Critical Design Review Report

Group 14

Madison Chubb, Grant Thomas, Jack Britton, Henry Kanfer

Table of Contents

Table of Figures

Table of Tables

Nomenclature

a = length of 1 wing – tip to root [length]

a-wall = length between servo and wall in actuator testing [length]

a-1,2 = respective lengths in Figure 2.7 [length]

b = span [meters]

c = Chord [meters]

C_L = Coefficient of lift

C_m = Coefficient of Moment

C_g = Center of gravity (m)

$\frac{C_L}{C_D}$ = Coefficient of Lift over Coefficient of drag, lift to drag ratio

D = Drag force [Newtons]

E.I. = expected improvement

EI = bending stiffness [force-length^2]

h = stringer cross section height [length]

I = area moment of inertia [length^4]

$I_{x,y,z}$ = principal moments of inertia [mass-length^2]

J(x) = Cost function

L = lift force [Newtons]

m = mass [grams]

P_R= Power Required

q = distributed load [force/length]

S = Wing Area [meters^2]

s_w = sweep [degrees]

T_R= Thrust Required [Newtons]

V_{stall}= Stall Velocity [Meters/second]

W = Weight [Newtons]

w = stringer cross section width [length]

w_d= Damping frequency [rad]

w_n= Natural frequency [rad]

$\overline{x}$ = centroid/equivalent force location [length]

δ = deflection [length]

ς = Damping coefficient

θ-*1,2* = respective angles in Figure 2.7 [angle]

λ= taper ratio

α = Angle of attack [degrees]

1. Introduction

1.1. Company Profile

Figure 1.1. Logo

We are Sweet Silence. Our mission: to protect the peace and quiet in our communities by silencing crying babies. Picture this: a father takes their child to the park but just as they arrive, the child spits their pacifier onto the dirty park ground. Obviously, he can't continue to use this dirty pacifier. The father is in dismay because he forgot to bring a spare and his child has begun crying… just then, he remembers that he can simply order another and have it within 5 minutes! As the Sweet Silence unmanned-plane soars above the park, delivering a fresh pacifier to the crying child, bystanders are filled with awe and relief as the cries fade and the sound of birds chirping returns.

Our company's headquarters are in New York, a large population center where our innovative product can flourish. We have multiple unmanned aircraft hangers located on rooftops across the city. Each is capable of operating within a 5 km radius of its storage hangar for up to 13 minutes of flight! The high population density allows for efficient distribution to various screeching sites. Our business model consists of the service we provide. Sweet Silence owns and maintains multiple delivery aircraft, the service being paid for by the city government. Parents in need within the cities will have no direct costs when ordering a delivery. The overall cost to the city is $199,999.99 per year for 200 km^2 of coverage.

Our product is designed for any scenario where a baby is disturbing the peace. Typically, our product will be utilized by parents or other individuals in outdoor public places like parks, resorts, theme parks, and sporting events. All the user needs to do is place a delivery request within the app, and a plane will take off to come deliver a fresh pacifier. Our current areas of investment

and research involve expanding the necessities available for delivery: blankets, stuffed animals, or even ear plugs (for the parents). Currently we have no competitors as our company, Sweet Silence is at the forefront of what we believe to be a multi-million-dollar market. We have already secured a contract with the city of New York and are preparing to release our first wave of aircraft on the market. The Pacifier Deployment System (PDS) weighs approximately 500g fully loaded.

We estimate an annual expense of approximately $25,000 per year for equipment upkeep and purchasing more supply for the aircraft to deliver. On top of this, there is expected to be around $60,000 per year to pay for the rent to store and operate these airplanes from the industrial district. All in all, we will charge each city a low, low $199,999.99 per year for our services. Our services are sold directly to the city. Every time a parent utilizes our app the money will go to the City and Swet Silence will get a portion of the profits. The city pays yearly for our service with options to renew or cancel each year. Sweet Silence owns and operates all their individual airplanes, under city management. All you have to do as a customer is call us through our app and Sweet Silence will be on its way in minutes! They say you cannot put a price on peace and quiet, but guess what? We did! And this is it!

Our marketing strategy is to build a strong online presence through social media platforms, working with parenting influencers, and collaborating with pediatricians to highlight the benefits of Sweet Silence products. We will also partner with children's stores and e-commerce platforms like Amazon to increase accessibility to our products. This will drive enormous demand and these constituents will pressure their elected city leaders to sign contracts with Sweet Silence. Our current product line is designed to drive interest among parents:

- Classic Pacifier: Soft, ergonomic design for comfort, with an emphasis on reducing noise when the child sucks or chews.
- Travel Pacifier: Compact, portable version that fits easily in bags for on-the-go parents.
- Customized Pacifiers: Personalized pacifiers with different colors, textures, and materials for various needs (e.g., for teething or sensitive gums).
- Limited Edition Pacifiers: Special themed designs for holidays or unique occasions.

1.2. Vehicle Description

The Sweet Silence aircraft has a maneuverability and efficiency at the forefront of its design. This unmanned aircraft was engineered to deliver top-of-the-line products in a way that never fails to impress customers. Sweet Silence's revolutionary aircraft design is featured in Figure 1.2.

Figure 1.2. Airplane

Summary: Our vehicle is an unmanned aircraft operating off of an advanced autopilot that navigates to the coordinates where an order is made within the app. Sweet Silence's plane has a mass of 3252.88 grams. The parametrically designed wing has a NACA0012 airfoil with taper of 0.4, root chord of 0.255m, tip chord of 0.153m, wingspan of 1.884 m, and an aileron with a length of .526m and chord of .0381m (see page 63 and 66 for dimension drawings). This plane is able to obtain a range of 46.6km with a flight time of 34.2 minutes overall. The plane and its parametric design and optimization process are analyzed in further detail throughout the report.

Table 1.1 Wing Parameters

Airfoil	NACA0012
Mass	3.252kg
Altitude of flight	100m
Endurance	34.2min
Range	46.6km
Wingspan	1.884m
Taper	0.4
Root Chord	0.255m
Tip Chord	0.102m

Aileron	0.526m

Challenges

- Ensuring customers maintain within an open area to review pacifier safely
- Make sure nobody walks through the payload drop off zone
- Ensuring that new possible cities have safe areas for take off and landing due to high population density
- Avoiding the use of prank calling as we like to serve every customer who calls

Unique Features

- Top of the line payload firing system for Pacifier delivery
- Custom wing designs for your city to perfectly adjust to climate conditions
- Personal aircraft maintenance by own our Sweet Silence Staff.
- Live tracking for delivery updates
- Can deliver even on holidays!
- Operate 24 hours a day
- Our staff truly love our company and what we stand for, fostering a great work environment

Despite these challenges our Sweet Silence Aircraft are the top of the line, ready to serve your city within minutes of receiving your call!

1.3. Software Used

AVL

Athena Vortex Lattice (AVL) was the software that aerodynamic specialists were constrained to model their aircraft. AVL is a computational tool used by engineers to analyze the aerodynamic performance of aircraft, to model airflow over the aircraft surfaces using vortex lattices. AVL is well suited for preliminary aircraft design modelling as well as iterative testing. It allows for the complete analysis of forces including but not limited to lift, drag, moments under different flight conditions like take off, landing, and trim analysis. Additionally, it provides insight for the aircraft's stability and control characteristics throughout various flight scenarios.

SolidWorks

SolidWorks was the CAD software used by the structures specialist to model the aircraft and design the wing. It was used in predicting center of gravity and principal moments of inertia based on geometry and material properties. SolidWorks was also the tool used for finite element analysis in predicting deflections and resonant frequencies. The avionics specialist also used SolidWorks for the design of the payload mechanism.

MATLAB

MATLAB is a programming software that utilizes computational programming in order to calculate outputs based on written code. MATLAB was specifically utilized by both Aerodynamic and Structural Specialists in order to complete the optimization process and robustness analysis.

Mission Planner

Mission Planner was used by the avionics specialist to program the Pixhawk. The Pixhawk flight computer needed to be flashed with the latest firmware within Mission Planner to function properly with ArduPilot. This system was used for managing radio control inputs and servo actuation, as well as managing multiple onboard sensors for tracking flight data. This is also the

system that would be used for implementing the Controls' waypoint navigation software if it were to be placed in control of the aircraft flight.

2. Aerodynamics

2.1 Design

2.1.1 Problem Statement

As an aerodynamic specialist, the goal was to change the geometry of the wing through various iterations both parametrically and using optimal design. The overall goal was to design a wing which can maintain mission requirements[Table 1.1], while being the most efficient at an altitude of 100m. The center of gravity, which was fixed in place, at 3.34 cm above the centerline of the wing was found based on Stock Airplane with Structures Model. To determine what the 'best' design, a cost function was utilized to numerically measure the performance of the aircraft. To optimize the wing configuration, a normalized and weighted cost function was formulated to guide the optimization process. The primary objective was to maximize the lift-to-drag ratio ($\frac{C_L}{C_D}$) within the mission constraints outlined in Table 1.1. However, because the chosen optimization approach employed a function minimization technique, the objective was reframed to minimize the cost function. By incorporating aerodynamic performance along with geometric penalties, the cost function enabled balanced consideration of lift generation, induced drag, and structural efficiency within the context of practical design limits. A minimization approach was taken with the goal of achieving a minimum $\frac{C_L}{C_D}$ ratio signifying the most efficient design through changes in geometry. The cost function [2.1] was made with four different parameters, airfoil, sweep(s_w), taper ratio (λ), and span (b). These parameters were normalized with respect to the Stock Airplane values to calculate the relative improvement from the starting iteration. The airfoil was analyzed through the $\frac{C_L}{C_D}$ ratio, the goal was to minimize the $\frac{C_D}{C_L}$ so one minus this normalized quantity was used. The drag ratio measured by AVL simplified the fuselage to a spiral, which did not account for the nose cone drag. Therefore, for every iteration from AVL, a factor 0.02 was added to the Coefficient of drag. The taper ratio was analyzed with respect to the stock value of 0.475 and squared for weighting purposes. The span was normalized to the original 1.578m and squared for weighting purposes. The sweep, s_w, was analyzed as a factor out of 100. The original stock aircraft had no sweep and thus was not normalized to any scale, just squared for weighing purposes.

$$J(x) = \left(1 - \frac{C_L/C_D}{6.85}\right) + \left(\frac{\lambda - 0.475}{0.475}\right)^2 + \left(\frac{b - 1.578}{1.578}\right)^2 + \left(\frac{s_w}{100}\right)^2 \qquad [2.1]$$

Athena Vortex Lattice (AVL) was the software that Aerodynamic specialists were constrained to model their aircraft. AVL is a computational tool used by engineers to analyze the aerodynamic performance of aircraft, to model airflow over the aircraft surfaces using vortex lattices. It allows for the analysis of forces including but not limited to lift, drag, moments under different flight conditions like take off, landing, and trim analysis. Additionally, it provides insight for the aircraft's stability and control characteristics throughout various flight scenarios. Using AVL allows for multiple iterations to be run, testing various configurations and parameters. The original Stock Airplane was modeled in its entirety, including the wings, fuselage, horizontal stabilizer, and vertical tail. Then the wing geometry only was changed for the remainder of

iterations. By using this software and the cost function parameters the best wing design was determined.

2.1.2 Airfoil

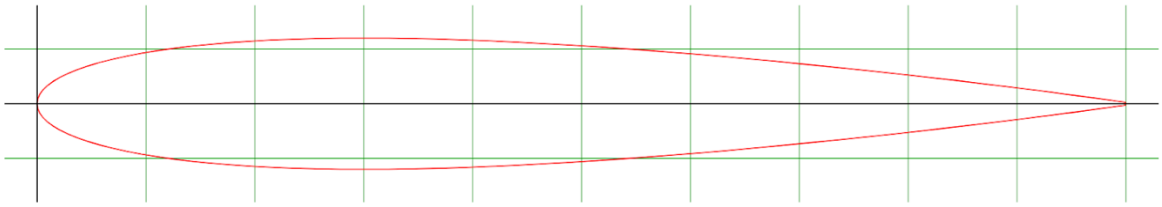

Figure 2.1 NACA0012 from Airfoil Tools [1]

The airfoil that was chosen for our company was the NACA0012. Despite the symmetric design of this airfoil type, after trying multiple different airfoils with the same wing designs, the NACA0012 outperformed others with a larger $\frac{C_L}{C_D}$ ratio when inputting our specific mission requirements. Specific testing for various airfoils was completed to establish which would best fit the team mission and constraints as seen in 2.1.3 Parametric Design.

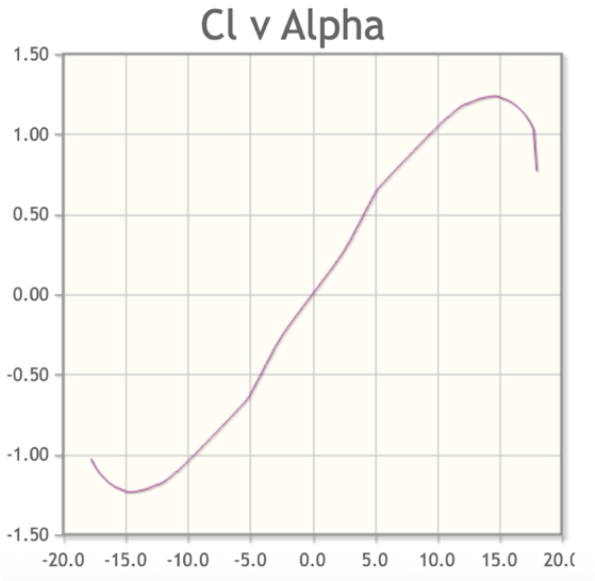

Figure 2.2 Coefficient of lift versus Alpha

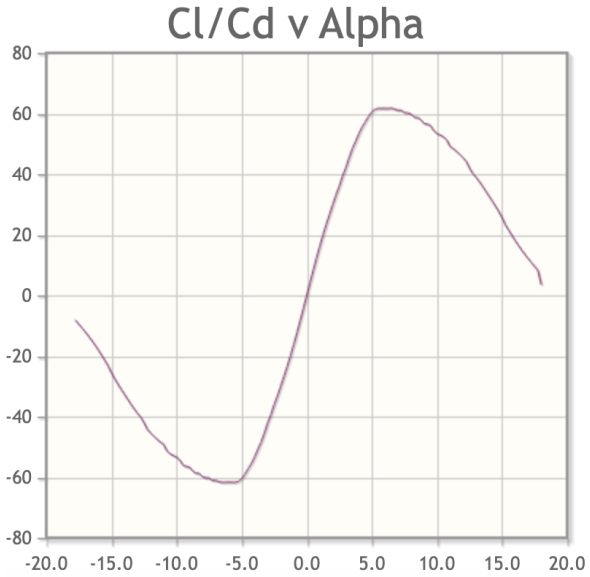

Figure 2.3 CL/CD versus Alpha

The theoretical values for the coefficient of lift versus angle of attack (Fig. 2.2 This ranges from -20 to + 20 degrees with Coefficient of lift values ranging from -1.5 to +1.5. This was tabulated from Airfoils.com (1) at a Reynolds number of 500,000, to best match mission requirements (Table 1.1). The peak value occurs at around 1.25 with a corresponding angle of attack around 14 degrees. Utilizing these expected values will further allow the comparison of Sweet Silence wing iterations to expected outcomes. Figure 2.3 displays the theoretical lift to drag ratio ($\frac{C_L}{C_D}$) over various angles of attack (α) ranging from -20 to positive 20 degrees for the NACA0012 airfoil (1). This graph correlates to a Reynolds number of 500,000 as this correlates to mission requirements (Table 1.1). The highest theoretical ratio occurs at a peak of around 8 degrees with a corresponding value of about 60. The peak values represent the optimal operating conditions for the aircraft to achieve maximum efficiency. Beyond this angle of attack begins the onset of flow separation begins over the wing surface. Analyzing this theoretical performance to Sweet Silence's wing design will allow for a complete analysis of performance based on expected measures.

The NACA0012 additionally aligns with the stock airplane model used in our flight tests, allowing for a probable increase in correlation between simulation and actual flight performance. The scale to which the model would be affected by a slight camber was not significant according to the iterations trials done with varying airfoils in AVL. NACA0012 has low profile drag which contributes to the overall higher lift to drag ratio during cruise, which is important for the mission. Stability is more predictable and leads to an easier analysis with the symmetry, making other factors like changing the wingspan and chord length easier to analyze. Having good performance over a variety of angles of attack is important as there are not always exactly consistent flight conditions for the missions and flight tests. The cons of a symmetrical design included no camber in the airfoil which can lead to a decrease in maximum lift conditions at low speeds. However despite this theory, AVL tests resulted in minimal difference in lift outputs with overall higher induced drag on a NACA2412. Having a slight lower inherent drag at lower speeds may result in a higher stall speed of the aircraft. However, based on AVL testing results and the mission criteria, the NACA0012 should perform well for the airfoil choice.

2.1.3 Parametric Design

Parametric design altered the airfoil type, wing area, sweep, and taper ratio. This design section outlines the iterative approach taken to evaluate the impact of these parameters on overall performance. Collaboration between team members was essential to create this design and ensure a cohesive output. The AVL software required the plane geometry, center of gravity location, weight, and moment of inertias for each axis. Initial simulations were based on the weight of the stock aircraft, as determined by the Avionics member. This initial weight, 4kg, was used to determine baseline values of lift drag ratio during the initial design interactions. The moments of inertia were determined from the Structures specialist in SolidWorks. Once these values were found and inputted, ten wings were iterated based on these four variables, and the coefficient of lift and drag were analyzed at each iteration for the cruise speed of the mission 29m/s as well as the altitude of 100m. The cost function values for each iteration were analyzed with the goal of minimization. Once each of these designs were iterated, the modes of each aircraft were determined utilizing AVL to analyze the stability of each aircraft. The modes analyzed included both the real and imaginary components of the spiral, roll, short period, phugoid, and Dutch roll pole values. These represent the aircraft's dynamic behavior in response to various disturbances. Planes were considered stable if the real part was less than zero, meaning that the disturbance will be minimized. Some iterations resulted in unstable poles, most commonly the spiral mode caused a divergence, in which the plane would not be able to maintain the flight mission. After comparing the $\frac{C_L}{C_D}$ ratios of each design, the mission requirements were analyzed on the most stable iterations to ensure it could achieve the requirements beyond just being a stable aircraft. The overall goal of the parametric design was to design a wing that fulfilled mission requirements by minimizing thrust and power, by maximizing the Coefficient of lift over drag ratio. In doing this, the cost function was minimized. Each design faced benefits and constraints and therefore the overall best parametric design was chosen, even with some tradeoffs as a perfect wing is not possible.

Summary of iterations

A summary of some of the 21 total iterations run through AVL allowed for a complete parametric analysis of the wing. Only some iterations were shown to display the logic taken for each of the 21 total iterations, while only highlighting some of the most relevant. Each iteration has the listed parameters that were changed in the iteration along with their cost value function. The modes of each design are also listed to analyze the stability, which help determined if the design was feasible for Sweet Silence. The first ten iterations display the parametric testing with the Stock Weight of the plane 3.8kg. The remaining 11 were the additional trials run with the updated weight and parameters. The final design has the most optimized wing with updated weight measurements based on SolidWorks, with a final weight of 3.26209kg.

Variable 1- Airfoils

Iteration 1: Rectangular wing - NACA0012

Table 2.1 Iteration 1 Parameters

Wing Area (S)	**Span (b)**	**Chord (c)**	$\frac{C_L}{C_D}$	**J(x)**

0.4576 m^2	1.7897 m	0.255 m	10.51	0.70529

Modes

Table 2.2.2 Iteration 1 Modes

Type	**Real**	**Imaginary**
Roll	-15.253862	0.0000000
Dutch Roll	-1.3431867	4.4191049
	-1.3431867	-4.4191049
Spiral	-0.66193817E-01	0.0000000
Short Period	-3.7463778	3.3643525
	-3.7463778	-3.3643525
Phugoid	0.61680756E-02	0.61098384
	0.61680756E-02	-0.61098384

This iteration had a decently high $\frac{C_L}{C_D}$ ratio, however the Phugoid mode was unstable as the real part of the eigenvalue was positive. This design could be optimized further however unstable phugoid modes generally originate with a center of gravity being moved forward to restate stability. The center of gravity in this design is fixed and cannot be altered. Overall, the wing produced a great $\frac{C_L}{C_D}$ ratio and the design can be altered with other factors to make it stable.

Iteration 2: Rectangular wing - NACA2412

Table 2.3 Iteration 2 Parameters

Wing Area (S)	Span (b)	Chord (c)	$\frac{C_L}{C_D}$	J(x)
0.4576 m^2	1.7897m	0.255m	9.9486	0.78724

Modes

Table 2.4 Iteration 2 Modes

Type	**Real**	**Imaginary**
Roll	-19.7666	0.0000000
Dutch Roll	-2.200744	3.633504
	-2.2000744	-3.633504
Spiral	-0.69193817E-01	0.0000000
Short Period	-5.52758	2.404301
	-5.52758	-2.404301
Phugoid	-0.4011	0.0
	0.2745	0.0

This iteration had a lower CL/CD ratio when only the airfoil was changed from the NACA0012 to the NACA2412, an asymmetric airfoil with some chamber. This design also led to once again, a set of unstable phugoid modes which did not formulate properly. At this point, the iteration was repeated with varying airfoil types. It was decided to continue testing the other variables while choosing the NACA0012 as the chosen airfoil. It produced the highest $\frac{C_L}{C_D}$ ratio although still requires further tuning to obtain full stability with the phugoid mode.

Variable 2 - Span

The stock airplane had a wingspan of 1.578m therefore iterations with a smaller and larger wingspan were tested to develop a range, showing the effect of span on the aircraft performance and stability derivatives.

Iteration 5: Rectangular wing - NACA0012

Table 2.5 Iteration 5 Parameters

Wing Area (S)	Span (b)	Chord (c)	$\frac{C_L}{C_D}$	J(x)
0.3825 m^2	1.5m	0.255m	10.1933	0.73597

Modes

Table 2.6 Iteration 5 Modes

Type	**Real**	**Imaginary**
Roll	-12.3594	0.0000000
Dutch Roll	-1.87518	4.4047101
	-1.87518	4.407101
Spiral	-0.1804102	0.0000000
Short Period	-4.7243	3.785201
	-4.7243	-3.785201
Phugoid	-0.65796E-01	0.041258384
	-0.65796E-01	-0.041258384

This iteration had the third largest $\frac{C_L}{C_D}$ ratio of all the iterations completed so far, as well as the first set of all stable poles as all of the real parts were negative. This design showed as a possible design, however further testing was done to have more options to compare and analyze.

Iteration 6: Rectangular wing - NACA0012

Table 2.7 Iteration 6 Parameters

Wing Area (S)	Span (b)	Chord (c)	$\frac{C_L}{C_D}$	J(x)
0.4095 m^2	1.82m	0.255m	10.52	0.709359

Modes

Table 2.8 Iteration 6 Modes

Type	**Real**	**Imaginary**
Roll	-16.01872	0.0000000
Dutch Roll	-1.363902	3.633594
	-1.363902	3.633504
Spiral	-0.621757E-01	0.0000000
Short Period	-3.30284	3.324501
	-3.30284	-3.324501
Phugoid	0.695296E-01	0.0606852
	0.695296E-01	-0.0606852

This iteration had the best $\frac{C_L}{C_D}$ out of all the testing iterations so far, showing a benefit to having an increase in wingspan for the overall performance of the airfoil. The modes were also all stable, further making it a good design option. Further iterations with other variables were done to compare with.

Variable 3 - Sweep

Both 5 and 10-degree sweeps were tested utilizing AVL metrics. The 10-degree sweep outperformed the two designs and the metrics for only 10 degrees (Table 2.9).

Iteration 7: 10-degree sweep - NACA0012

Table 2.9 Iteration 7 Parameters

Wing Area (S)	Span (b)	Chord (c)	$\frac{C_L}{C_D}$	J(x)
0.4095 m^2	1.7897m	0.255m	10.10667	0.76417

Modes

Table 2.10 Iteration 7 Modes

Type	**Real**	**Imaginary**
Roll	-15.766	0.0000000
Dutch Roll	-1.354744	5.10526
	-1.354744	5.10526
Spiral	-0.72463817E-01	0.0000000
Short Period	-3.9754	6.663241
	-3.9754	-6.663241
Phugoid	0.175296E-01	0.785652
	0.175296E-01	-0.785652

This iteration had decently high $\frac{C_L}{C_D}$ ratio when sweep was added to the aircraft. However, other designs had a better overall ratio, additionally when designing a wing with the structures team member a sweep makes internal components a lot more difficult. Considering there were better wing designs, this one was not considered. Additionally in coordination with the Structures member, having such a large sweep made it more difficult to create the internal structures with strong supporting ribs and spars.

Variable 4 - Taper

A taper ratio of 0.6 and 0.8 were both tested with the NACA0012, overall, the taper of 0.6 generated the best result between the two designs.

Iteration 9: 0.6 Taper wing - NACA0012

Table 2.11 Iteration 9 Parameters

Wing Area (S)	Span (b)	Chord (c)	$\frac{C_L}{C_D}$	J(x)
$0.4641m^2$	1.82m	0.255m	10.72	-0.47219

Modes

Table 2.12 Iteration 9 Modes

Type	**Real**	**Imaginary**
Roll	-14.497622	0.0000000
Dutch Roll	-1.4537696	4.06727
	-1.4537696	4.06727
Spiral	-0.3024585E-01	0.0000000
Short Period	-3.4957535	3.1035012
	-3.4957535	-3.1035012
Phugoid	0.175296E-01	0.59523559
	0.175296E-01	-0.59523559

The initial parametric wing was chosen to have a taper of 0.6, S= 0.4641 m^2, b= 1.82 m, a root chord of c=0.255m with a $\frac{C_L}{C_D}$ = 10.72. This wing geometry was sent to the Structure's member, to create it in SolidWorks. They created the outside structure as designed by Aerodynamicists, as well as the internal structure with ribs and spares. Once the SolidWorks model was made, the weight was found to be 3.26209 kg and updated accordingly. AVL was then run again 10 times with the trials from before changing the span, airfoil, sweep, and taper. The results with the new weight factor and the modes were tabulated and then analyzed. Table 2.13 shows the wings iterative cost values functions, and Table 2.14 shows with the highest output in detail with the modes, and a $\frac{C_L}{C_D}$ at a value of 12.49. This is a higher value than was reached before, most likely due to the decreased weight from previous testing making the aircraft more lightweight a durable during flight conditions. This new wing was concluded to be the best parametric design possible given the constraints of this project.

Table 2.13 Cost Function Values for Iteration 11 - 20

Iteration number	Airfoil	Span (m)	Taper	Sweep	$\frac{C_L}{C_D}$	J(x)
11	NACA0012	1.7897	1	0	11.26	0.6502
12	NACA2412	1.7897	1	0	10.23	0.7128
13	NACA0012	1.5	1	0	10.95	0.812
14	NACA0012	1.6	1	0	11.023	0.756
15	NACA0012	1.7	1	0	11.1933	0.6325
16	NACA0012	1.82	1	0	11.435	0.51353
17	NACA0012	1.7897	1	5	11.03	0.61217
18	NACA0012	1.7897	1	10	10.56	0.7213
19	NACA0012	1.82	0.6	0	12.49	-0.7305867
20	NACA0012	1.82	0.8	0	11.93	-0.56731

Iteration 19: Rectangular wing - NACA0012

Table 2.14 Iteration 19 Parameters

Wing Area (S)	Span (b)	Taper	Chord (c)	$\frac{C_L}{C_D}$	J(x)
0.4641 m^2	1.82m	0.6	0.255m	12.49	-0.7305867

Modes

Table 2.15 Iteration 19 Modes

Type	**Real**	**Imaginary**
Roll	-24.791502	0.0000000
Dutch Roll	-2.1412517	5.2519812
	-2.1412517	-5.5665775

Spiral	-0.1141E-01	0.0000000
Short Period	-6.330884	11.873947
	-6.330884	-11.873947
Phugoid	-0.48157E-02	0. 44429986
	-0. 48157E-02	-0.44429986

The pole values were found to be all real poles based on their negative real values. Overall, the stability increased as the magnitude increased with respect to previous iterations. This aligns with the decrease in weight as well as the higher coefficient of lift to drag ratio found for this iteration.

Conclusion

The best parametric wing was chosen to have a taper of 0.6, S= 0.4641 m^2 , b= 1.82m, a root chord of c=0.255m with a $\frac{C_L}{C_D}$ = 12.49 and a cost function value of J(x) = -0.7305867 This new wing was concluded to be the best parametric design possible given the constraints of this project. The cost value function was minimalized showing the effectiveness of iterative design by testing various parameters in the cost function.

Computational results of aerodynamics and loads for entire aircraft

Table 2.16 Computational Properties of Parametric Design

	Takeoff	**Cruise**
Weight	31.968N	31.968N
Speed	17m/s	29m/s
CL	0.5799	0.2927656
CD	0.03653	0.02344
$\frac{C_L}{C_D}$	15.876	12.49

Lift force (L)	39.012N	39.012N
Drag force (D)	2.458N	54.987N
Alpha	7.854 degrees	2.6859 degrees
Thrust Required (TR)	2.0136N	2.5595N
Power Required (PR)	27.652	68.6532
Stall Velocity	10.028m/s	10.028m/s

Equations utilized:

$$T_R = W\frac{1}{C_L/C_D}$$

$$P_R = \sqrt{\frac{W^3}{\frac{1}{2}\rho}\frac{1}{C_L^{3/2}/C_D}}$$

Figure 2.4 Equation for Tr and Pr for Aircraft Properties

$$V_{stall} = \sqrt{\frac{1}{\frac{1}{2}\rho}\frac{W}{S}\frac{1}{C_{L_{max}}}}$$

Figure 2.5 Equation for stall velocity

2.1.4 Optimal Design

To optimize the wing configuration, a normalized and weighted cost function was formulated to guide the optimization process. The primary objective was to maximize the lift-to-drag ratio ($\frac{C_L}{C_D}$) within the mission constraints outlined in Table 1.1. However, because the chosen optimization approach employed a function minimization technique, the objective was reframed to minimize the cost function. By incorporating aerodynamic performance along with geometric penalties, the cost function enabled a balanced consideration of lift generation, induced drag, and structural efficiency within the context of practical design limits. From the original cost function, the sweep eliminated as a design parameter for simplification. This decision was due to limited practicality when considering mission requirements. The structures specialist was responsible for designing internal wing structure including ribs and spars. During the initial parametric design period, it was noted that high sweep angles added unnecessary complexity, without offering significant performance benefits. Increased sweep reduced the ability to maintain a structurally stable and manufacturable wing design. Due to these factors the cost function was simplified [2.2], only changing the span and taper ratio of the wing were considered for optimization methodology.

$$J = (1 - \frac{C_L/C_D}{6.85}) + \left(\frac{\lambda - 0.475}{0.475}\right)^2 + \left(\frac{b - 1.578}{1.578}\right)^2 \quad [2.2]$$

The optimization function utilized five different MATLAB files to generate the most optimal design. The optimization process works by running multiple iterations of the surrogate model and the algorithm explores design possibilities by adjusting a set of parameters. These parameters for the chosen cost function include the taper and span which can only be altered within predetermined minimum and maximum range. The five MATLAB files generated a total of 20 design iterations with the aim of minimizing the cost function. Although continuation of running points would ultimately converge to the 'best' design, for the scope of this report, after twenty points the design was considered optimal.

The first file used a Latin Hypercube Sampling (LHS) method to determine an initial set of design points (taper and span) for the optimization process. LHS is a statistical technique that generates representative starting points for the surrogate model. By starting initially with a set of five data points that represent the design space, further iterations can lead to efficiently finding the minimal value of the cost function. This file required an input for the minimum and maximum values for each parameter, which were determined based off parametric design iterations. The taper ratio was set to [0.4 - 1] and the span was set to [1.2 - 2.5] meters. These values were chosen based on structural limitations of the wingspan and the theoretical taper ratios. Based on these inputs, MATLAB returned five starting parameter value sets (Table 2.17), which were used as the first 5 case runs for design iterations. Each of these new parameter values were used to calculate the five new wing geometric shapes. These metrics were inputted into AVL and simulated at trim conditions with the cruise speed to generate the new coefficient of lift and drag values. Once all the data was found for each of the wing designs, the cost function was calculated utilizing Excel. The cost function values were then taken and inputted into the second MATLAB file, eas4710_sm_avl02.m.

Table 2.17 Iterative Properties for 5 Design points

Design case	Span	Taper	C_L	C_D	$\frac{C_L}{C_D}$	$\frac{C_D}{C_L}$	J(x)Cost function value
Case 1	1.525	0.4	0.26587	0.0223	11.9115	0.08395	-0.71285
Case 2	1.85	0.95	0.15749	0.0211	7.4772	0.13373	0.93815
Case 3	1.2	0.675	0.28236	0.0238	11.8453	0.08442	-0.49457
Case 4	2.5	0.8125	0.12527	0.0205	6.1161	0.16350	0.95338
Case 5	2.175	0.5375	0.16968	0.0208	8.1535	0.12264	-0.02985

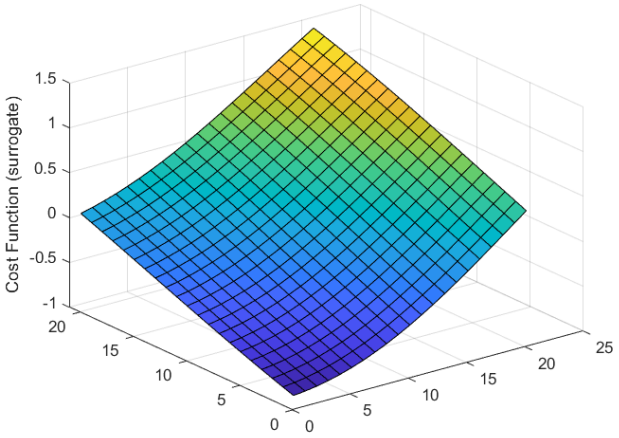

Figure 2.6 Cost Function after 5 points

Figure 2.6 shows the Cost function values with respect to the surrogate model after the first 5 design points were generated. The cost function displays how well the design iterations performed. The colored gradient indicates the magnitude of the cost function, higher values are indicated with the warmer tones. These represent larger values, thus those needing more improvement to reach minimalization. The x axes represented the two design parameters which were altered in the design space, with the cost function on the vertical axis representing the value of the cost function iterated through the design space for the five data points. The minimum value that was found in the first iteration correlated to a span of 1.525m and a taper ratio of 0.4, which yielded a cost value minimum of J(x)=-0.7128499197. This provided a good starting point for future design iterations.

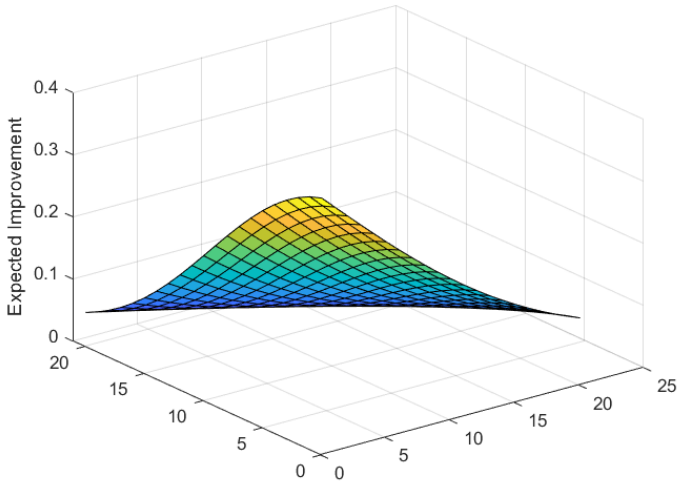

Figure 2.7 Expected Improvement for 5 points

The horizontal plane in Fig 2.7 represents the two design variables, span and taper ratio. The vertical axis represents the expected improvement of the function. This was a metric used to determine how the design space can be improved to further minimize the cost function. Expected

improvement estimates how much the cost function could decrease in subsequent iterations, serving as a guide for the MATLAB algorithm to strategically select the next five sampling points. The color gradient reinforces this interpretation, warmer colors highlight regions where greater improvement is anticipated, indicating areas that should be prioritized by the code in the next iteration to further minimize the cost function.

The next MATLAB iteration which was run utilizing the eas4710_sm_avl02.m file. This file returned the next five run cases (Table 2.18) These new span and taper ratios were each tabulated to generate the new wing geometries and then run through AVL to generate their respective coefficient of lift and drag values. These values were utilized to calculate their respective cost function values. The goal of optimization was to minimize the cost function value. It can be seen when comparing these values with the previous iteration (Table 2.17) that these values successfully got smaller. This proved during the iterative process that the function was successfully becoming further minimized.

Table 2.18 Iterative Properties for 10 design points

	Span	Taper	C_L	C_D	$\frac{C_L}{C_D}$	$\frac{C_D}{C_L}$	J(x) Cost function value
Case 6	1.2	0.42	0.33786	0.0244	13.8683	0.07211	-0.94018
Case 7	1.265	0.4	0.3205	0.0237	13.4702	0.07424	-0.90212
Case 8	1.33	0.4	0.30484	0.0233	13.0712	0.07650	-0.8586
Case 9	1.2	0.4275	0.33136	0.0243	13.6298	0.07337	-0.9224
Case 10	1.265	0.4275	0.31424	0.0237	13.2329	0.07557	-0.8825

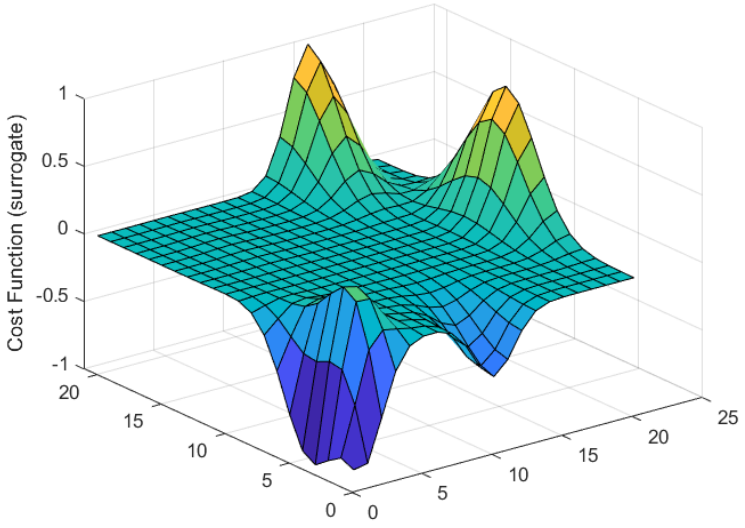

Figure 2.8 Cost function after 10 points

The Figure 2.8 represents the cost function generated after the 10 points were evaluated in the design space. Each point corresponds to the varying combination of taper and span with their resulting surrogate model values. Regions with a minimized value are once again indicated by the darker blue regions whereas other peaks still require some optimization. The minimal value for this run case was found at a span of 1.265m and 0.4 taper ratio, with a cost function of -0.94018. The nonlinear shape can be seen with the multiple local minima and maximum values. This is suggesting a design space is still in need to undergo more iterations before reaching the true minimum. The overall graph showed sign of improvement within the design space as compared to previous iterations (Fig 2.6) validating the effectiveness of the optimization approach.

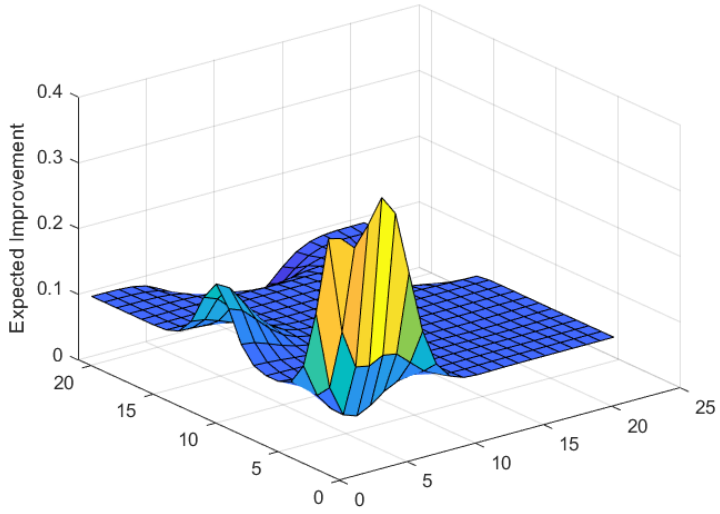

Figure 2.9 Expected Improvement after 10 points

Figure 2.9 displays the expected improvement across the design space. This graph predicts the regions in which the most improvements were expected to be in future iterations. The general flat region of this graph represents a limited amount of improvement, suggesting an already near optimal point where as the region with the large yellow tones peak show a need for greater minimalization through further iterations.

The next five run values were run through AVL and their new cost value functions were tabulated (Table 2.19). It can be seen based on the cost function values that the optimization process was improving over each iteration as the values continue to decrease each time MATLAB was run.

Table 2.19 Iterative Properties after 15 design points

	Span	Taper	C_L	C_D	$\frac{C_L}{C_D}$	$\frac{C_D}{C_L}$	J(x) Cost function value
Case 11	1.2	0.675	0.2823	0.02383	11.84530	0.08442	-0.4945745462
Case 12	1.2	0.4825	0.3191	0.02417	13.20419	0.07573	-0.8699895932
Case 13	1.2	0.51	0.3133	0.02412	12.98745	0.07699	-0.8331713392
Case 14	1.2	0.455	0.3251	0.02423	13.41373	0.07455	-0.8990552188
Case 15	1.2	0.4	0.3379	0.02436	13.86831	0.07211	-0.9422602471

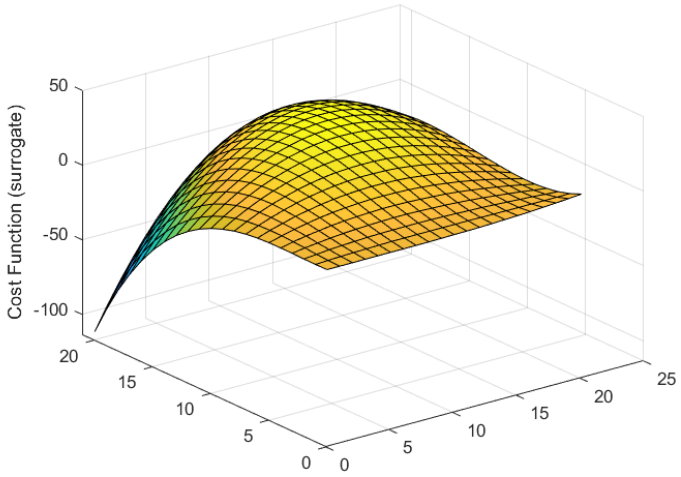

Figure 2.10 Cost function after 15 points

The cost function for this run case (Fig. 2.10) shows a more stable and smooth outputted graph. This was noted as a significant improvement as the cost function seems to be closer to reaching the most optimal pattern. The graph being more uniform signifies a reduced uncertainty in the design space, and therefore a more likely stable solution after the final iteration. The minimal cost function was found to be J=-0.9422602471 which corresponded to a span of 1.2m and a taper of 0.4.

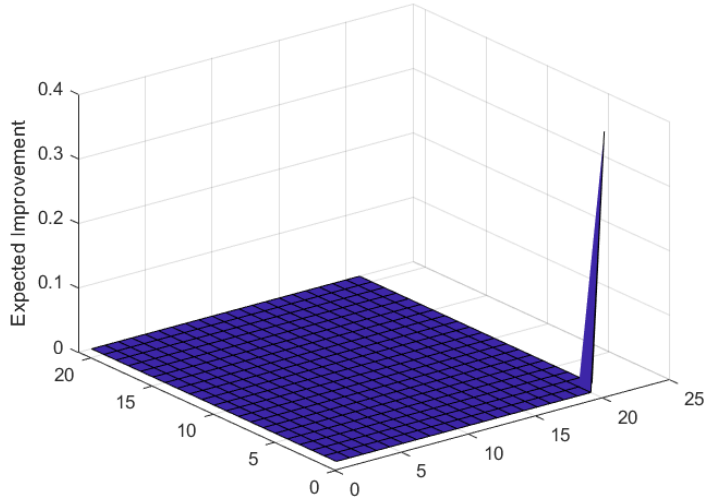

Figure 2.11 Expected Improvement after 15 points

Figure 2.11 displays the future improvement possible for the next iteration. The graph can be seen to mostly lie at a value of zero, with one major spike. This was interpreted as the function within the range had little room for improvement. The design space has a very small area left to improve, with most of the function reaching a minimum.

The final 5 points were run through MATLAB to generate the most optimal wing design. The results are summarized (Table 2.20). After 20 points were generated the design was considered optimal and the lowest cost function from all the trials were analyzed.

Table 2.20 Iterative Properties after 20 design points

	Span	Taper	C_L	C_D	$\frac{C_L}{C_D}$	$\frac{C_D}{C_L}$	J(x) Cost function value
Case 16	1.2	0.95	0.24252	0.023472	10.33231084	0.09678377041	0.549014651
Case 17	1.265	0.95	0.23108	0.0230135	10.04106285	0.09959105072	0.5734950608
Case 18	1.2	0.9225	0.24963	0.023142	10.786881	0.0927052037	0.370216371
Case 19	1.33	0.95	0.22451	0.02304	9.744357639	0.1026234912	0.6021656065
Case 20	1.265	0.9225	0.22891	0.023312	9.819406314	0.1018391508	0.4934160066

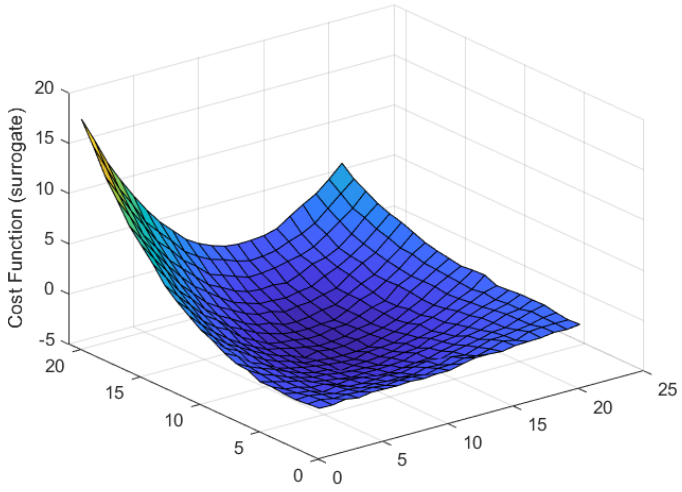

Figure 2.12 Cost Function after 20 points

The cost function for this run case (Fig. 2.12) shows a stable and smooth outputted graph. The shape of the graph is concave up, showing the optimal minimum in the middle region. The color of the graph is almost entirely dark blue, further supporting the cost function is minimized. The graph is more uniform which signified a reduced uncertainty in the design space. A strong final iteration was met after utilizing 20 points. A small region of yellow is shown in the top left corner, meaning the function could have been even further minimized with future testing. For the scope of this report, this result was considered the fully optimized, although more iterations would refine this result.

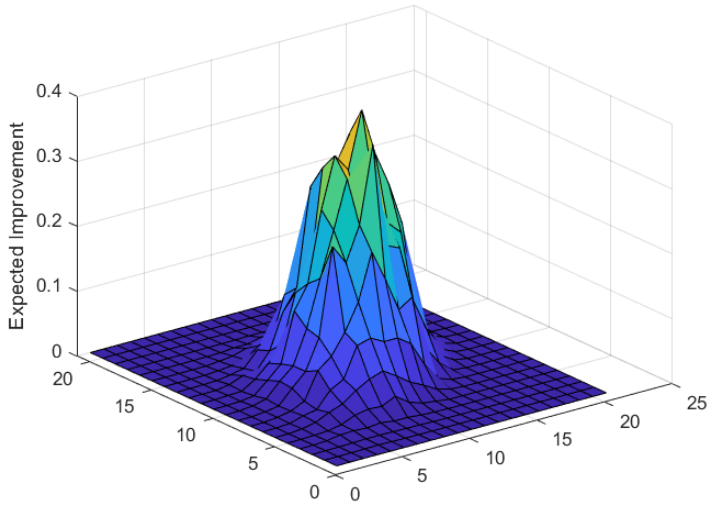

Figure 2.13 Expected Improvement after 20 points

Fig 2.13 represents the final iteration output of the MATLAB file with twenty design points. The majority of the function is optimized as can be seen in with the expected improvement, near zero for most design space values. The MATLAB file still believes there is more room for improvement, future testing to generate more points would establish an even further optimal design, however twenty was considered optimal for the scope of this report.

2.2 Wing

The wing design that resulted in the "best" outcome was defined as that of which had the smallest cost function value. The goal of parametric and optimal design, although different methods, was to minimize the value of the cost function through changing a variety of parameters including the span, taper ratio, sweep, and airfoil type. By analyzing each design through an iterative process and finding the cost function value at each point the best design was found to have a cost function value of J(x) = -0.9422602471, this corresponded to Case 15 in the 2.4.1 Optimization Design. This was the minimal value found throughout all iterations and therefore correlated to the best wing design. The specific wing geometry was a NACA0012 airfoil with a span of 1.2 meters and a taper ratio of 0.4 and the $\frac{C_L}{C_D}$was found to be 13.86.

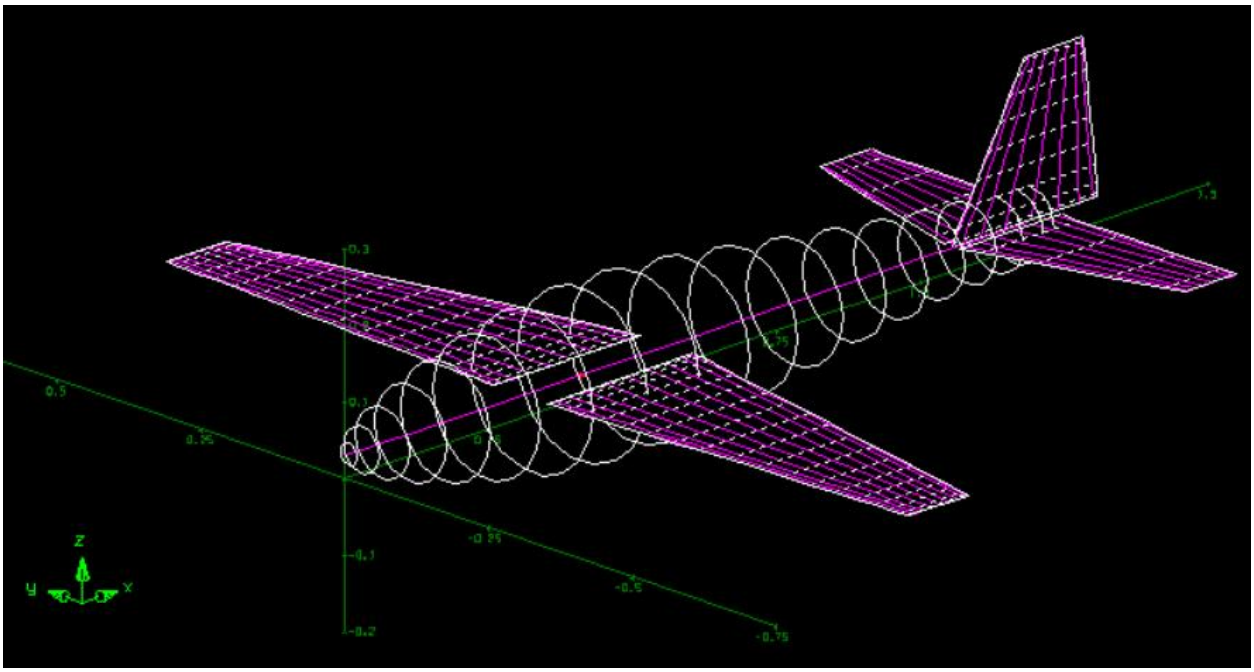

Figure 2.14 Optimized Plane from AVL

Figure 2.14 displays the optimized plane geometry in AVL based on Case 15 which returned the lowest cost value function. The fuselage was modeled as a spiral based on the original stock airplane. The horizontal tail and vertical stabilizer were also not altered from Stock Measurements. This design represented the best wing based on mission requirements and aerodynamic constraints.

Theoretical plot for lift and drag from AVL

Coefficient of Lift versus Alpha

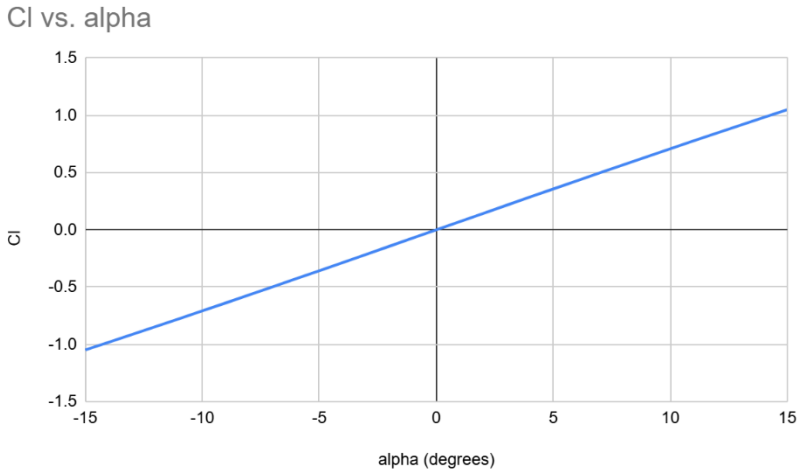

Figure 2.15 Coefficient of lift versus Alpha

The C_l vs α graph in Figure 2.15 is for the AVL model output. AVL assumes frictionless inviscid flow, and therefore the graph above is linear without a clear C_{lmax} value. Based on information from online sources, on the NACA0012, the maximum value of C_l is around 1.4 - 1.5 and occurs around 15 degrees.

Coefficient of Drag versus Alpha

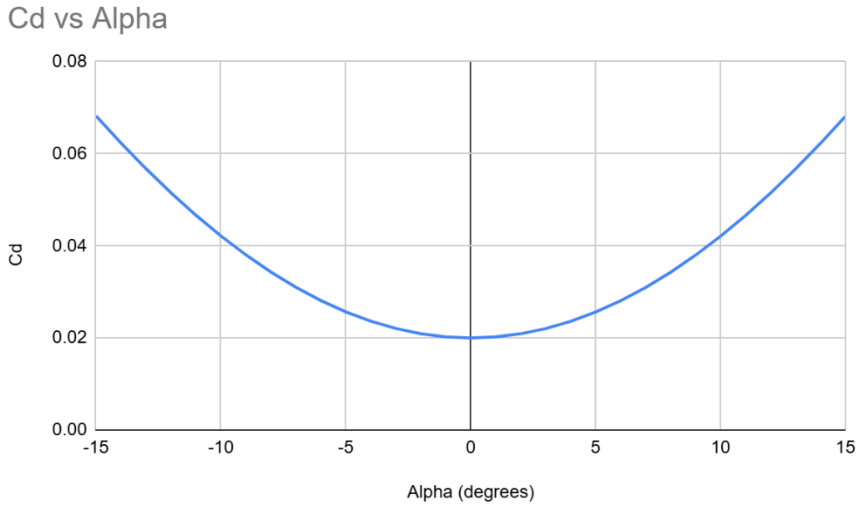

Figure 2.16 Coefficient of Drag versus Alpha

Figure 2.16 shows the value for C_d vs α and is a parabolic shape. The lowest value of the coefficient of drag was found at the alpha of zero degrees which corresponds to a C_d of 0.02. Therefore the most efficient flight conditions in terms of drag are found to be at low angles of attack. AVL only models the induced drag of the aircraft model, therefore a factor of 0.02 drag was added to each result to account for other drag factors from the nose cone that the aircraft

experiences. Analyzing the pattern of C_d and obtaining the lowest value while maintaining the highest C_l ratio is important to have the most efficient performance.

Coefficient of Lift/ Coefficient of Drag versus Alpha

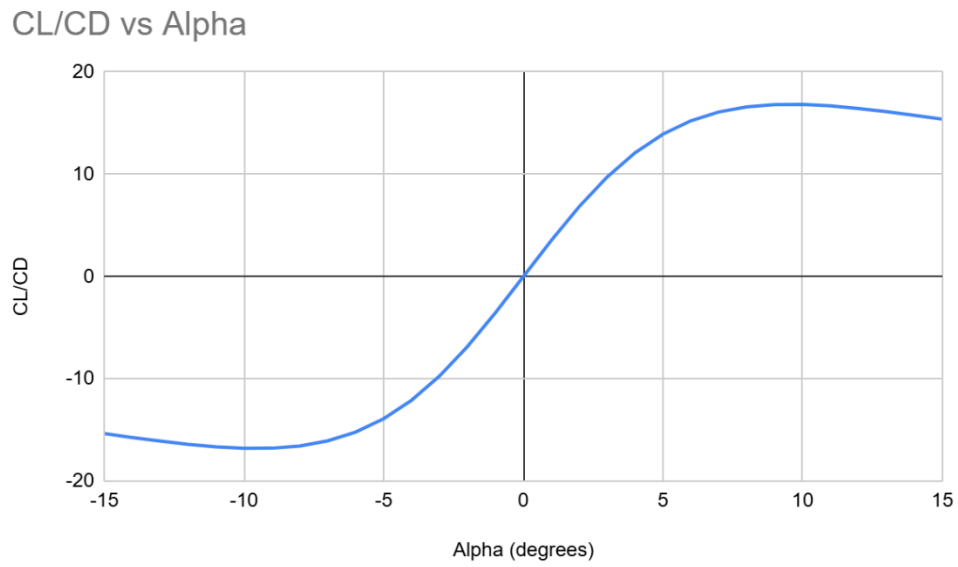

Figure 2.17 CL/CD versus Alpha

Figure 2.17 represents the aerodynamic efficiency of the aircraft across varying angles of attack. A high maximum value of CL is desired with the lowest possible CD. The maximum value from the graph was found to be 16.82635513 at 10 degrees. At low values of alpha the ratio is small and negative, above alpha of zero the ratio begins to increase and eventually reaches a maximum. Through optimization of the wing area, chord, taper, and airfoil this ratio was altered through many interactions until the most efficient was found to meet the mission criteria.

Table 2.21 Optimal Wing Properties

	Takeoff	**Cruise**
Weight	32.01N	32.01N
Speed	17m/s	29m/s
CL	0.5934	0.3379
CD	0.02154	0.023312
$\frac{C_L}{C_D}$	16.83	13.86
J(x)	-1.57988039	-0.9422602471
Lift force (L)	40.254N	40.254**N**
Drag force (D)	1.902N	2.39N
Alpha	7.99 degrees	4.039 degrees
TR	1.902 N	2.39N
PR	63.458N	79.747N
Stall Velocity	11.13m/s	11.13m/s

Equations utilized:

$$T_R = W\frac{1}{C_L/C_D}$$

$$P_R = \sqrt{\frac{W^3}{\frac{1}{2}\rho}}\frac{1}{C_L^{3/2}/C_D}$$

Figure 2.18 Equations for Thrust required and Power required

$$V_{stall} = \sqrt{\frac{1}{\frac{1}{2}\rho}\frac{W}{S}\frac{1}{C_{L_{max}}}}$$

Figure 2.19 Equation for the stall velocity

2.3 Aircraft Analysis

2.3.1 Trim

The trim analysis constrained the speed of 29m/s which was established based on Avionics data obtained during flight tests. This constraint represents the optimal operating condition for the aircraft during flight, while maintaining mission requirements. To simulate trim conditions, AVL was utilized with the wing design of case 15 with span of 1.2m and a taper ratio of 0.4. The roll, pitch, and yaw moments were constrained to zero to represent true trim conditions where the aircraft is in steady flight without any additional rotational moments. Additionally, the assumption of balanced aerodynamic forces acting on the wing was assumed, meaning lift equaled the weight. Once AVL tabulated the conditions, the angle of attack (α) was determined to be 4.0039 degrees, and the elevator deflection was found to be -1.595 degrees. The values confirm the aircraft is properly trimmed for our altitude of flight, further showing a stable wing. A small positive angle of attack aligns consistently with aircraft performance expectations with a small nose up altitude to generate the necessary lift to counteract the weight. The small negative elevator deflection provides the force to overall contribute to overall stability in the pitch axis. It applies a downward force on the tailplane, ensuring the forces are balanced based on the center of gravity location. These conditions ensure flight path stability, minimizing oscillations in flight patterns and improving the pilot's ability to control the aircraft during flight.

2.3.2 Static Stability

Static Stability was proven using three different graphs, $C_{m\alpha}$vs α,C_l vs β,and $C_{n\beta}$ vs β . These graphs represent the aircraft performance over varying degrees from -15 to +15 for both alpha and beta representing the three different elements of static stability.

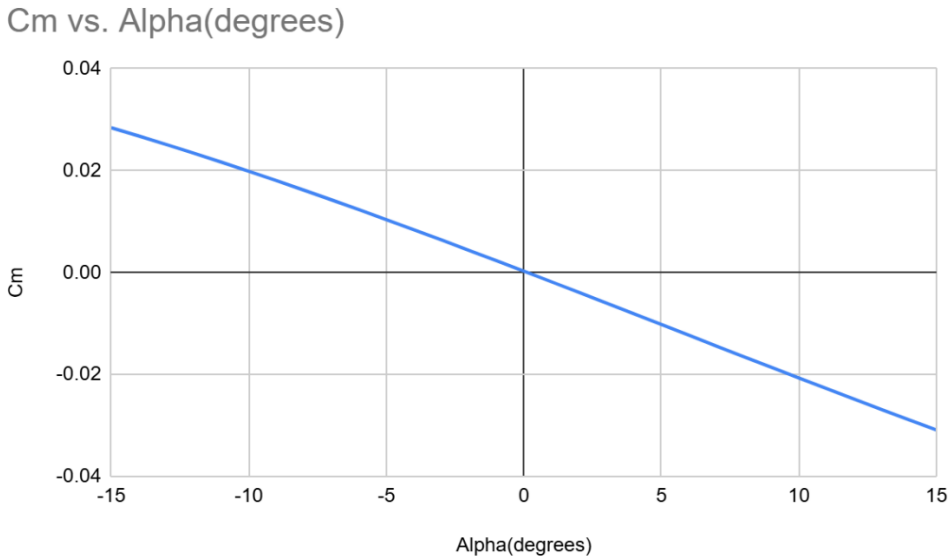

Figure 2.20 Pitching Moment versus Angle of Attack

Figure 2.20 illustrates the longitudinal static stability of the aircraft, which characterizes its pitching behavior. Longitudinal stability is confirmed when the slope of the moment coefficient versus the angle of attack is negative. A negative slope indicates that, as the aircraft experiences a pitch-up disturbance, the resulting nose-down moment acts to restore the aircraft to its trim equilibrium, thereby stabilizing the flight path. This behavior ensures that the aircraft does not diverge uncontrollably from its desired attitude but instead returns to a stable condition following a perturbation. From the data provided by AVL, the wing design was found to exhibit a negative slope, confirming that the aircraft possesses positive longitudinal static stability. This means that the aircraft's aerodynamic configuration is inherently stable in the pitch axis, with disturbances being self-correcting. The negative slope further indicates that the aircraft's design ensures the appropriate balance between lift and moment forces, promoting stability throughout the flight envelope.

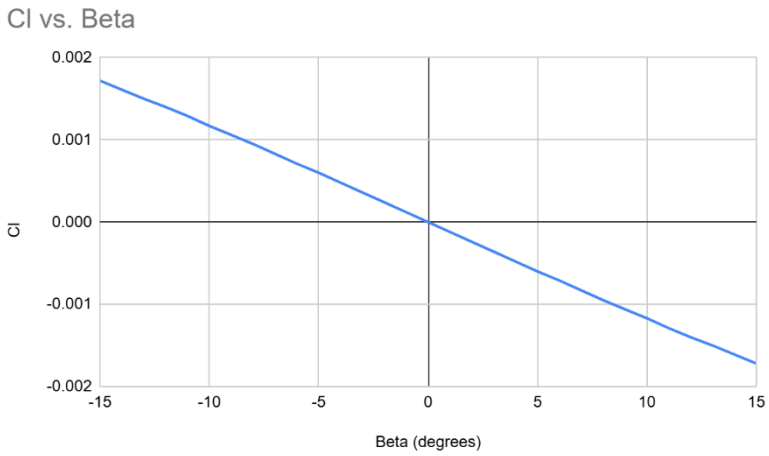

Figure 2.21 Roll Moment versus Beta

The graph above represents the Roll moment versus slide slip angle (Beta). It has a negative slope showing stability in the aircraft with the parametric design. A negative slope was found for the optimal design (Fig. 2.21), meaning stability conditions were met.

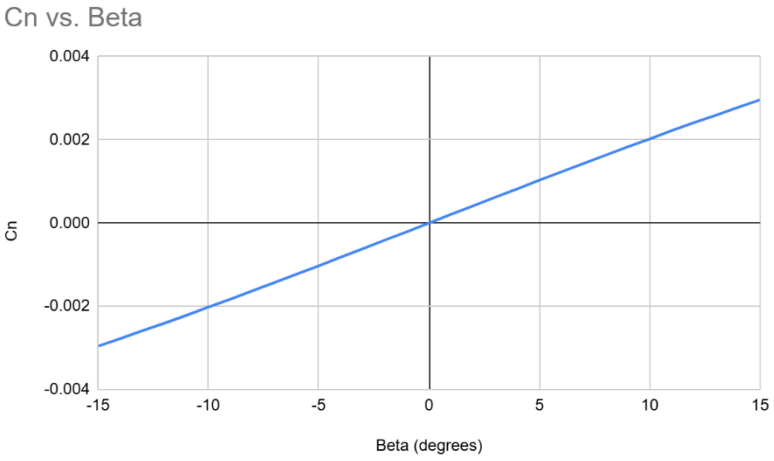

Figure 2.22 Yaw Moment versus Beta

Figure 2.22 shows the static directional stability which is how the aircraft responds to the yaw disturbances. A positive slope indicates a yaw in the nose to the left, with a resulting restoring force which yaws back to the right, to maintain stability. Based on AVL inputs the aircraft was found to have a positive slope for the stability, meaning it is stable for this parameter.

2.3.3 Stability and Control Derivatives

The Modes of the most optimized wing were analyzed (Table 2.22) to ensure that even if the cost function was the lowest, that these parameters were strong enough to produce a stable and level flight path.

Table 2.22 Optimal Wing Modes

Type	**Real**	**Imaginary**
Roll	-6.8245410	0.0000000
Dutch Roll	-1.8829395	5.4859092
	-1.8829395	-5.4859092
Spiral	-0.84870237E-01	0.0000000
Short Period	-4.3338683	5.9821362
	-4.3338683	-5.9821362
Phugoid	-0.47816455E-02	0.39693001
	-0.47816455E-02	-0.39693001

The modes found (Table 2.22) displays the modes of the optimal wing. These modes were successfully found to be stable, as the real parts of the modes are less than zero. These values specifically are analyzed in detail within 2.3.5 Flight Dynamics, they display a viable plane option with stable parameters.

```
Stability-axis derivatives...

                            alpha                beta
                     ----------------    ----------------
z' force CL |    CLa =   5.135155    CLb =   0.000000
y  force CY |    CYa =   0.000000    CYb =  -0.401381
x' mom.  Cl'|    Cla =  -0.000000    Clb =  -0.038736
y  mom.  Cm |    Cma =  -1.225086    Cmb =   0.000000
z' mom.  Cn'|    Cna =  -0.000000    Cnb =   0.043339

                       roll rate  p'      pitch rate  q'        yaw rate  r'
                     ----------------    ----------------    ----------------
z' force CL |    CLp =   0.000000    CLq =  10.296403    CLr =  -0.000000
y  force CY |    CYp =   0.048726    CYq =  -0.000000    CYr =   0.136925
x' mom.  Cl'|    Clp =  -0.594092    Clq =   0.000000    Clr =   0.103395
y  mom.  Cm |    Cmp =  -0.000000    Cmq = -35.288375    Cmr =   0.000000
z' mom.  Cn'|    Cnp =  -0.049100    Cnq =   0.000000    Cnr =  -0.254853

                    Aileron      d01     elevator     d02     rudder       d03
                     ----------------    ----------------    ----------------
z' force CL |   CLd01 =   0.000000   CLd02 =   0.013639   CLd03 =  -0.000000
y  force CY |   CYd01 =   0.000212   CYd02 =   0.000000   CYd03 =  -0.004623
x' mom.  Cl'|   Cld01 =  -0.007463   Cld02 =  -0.000000   Cld03 =  -0.000310
y  mom.  Cm |   Cmd01 =   0.000000   Cmd02 =  -0.052879   Cmd03 =   0.000000
z' mom.  Cn'|   Cnd01 =  -0.000417   Cnd02 =  -0.000000   Cnd03 =   0.003054
Trefftz drag| CDffd01 =   0.000000 CDffd02 =  -0.000913 CDffd03 =  -0.000000
span eff.   |    ed01 =   0.000000    ed02 =   0.026133    ed03 =   0.000000



Neutral point  Xnp =   0.455233

Clb Cnr / Clr Cnb  =   2.203049    (  > 1 if spirally stable )
```

Figure 2.23 Stability Derivatives derived from AVL

Stability Derivatives were derived from AVL (Fig. 2.23) to describe the flight parameters at straight and level trim with a speed of 29m/s. Various characteristics show the defining parameters of the flight. This can be seen with the coefficient of pitch damping $C_{Mq=}$ -35.288, a negative value is required for stable flight path. The plane is additionally spirally stable with a ratio of 2.203, which is greater than one, signifying spiral stability. $C_{L\beta=}$ -0.03876 and $C_{n\beta=}$ 0.04339 further signifying the stability of the aircraft. The combination of each of these parameters signify a stable flight

2.3.4 Loads

The aerodynamic loads acting on the aircraft included lift, drag, weight, and thrust. These forces had to be balanced and accounted for in order to maintain a steady and level flight (Table 2.21). These conditions were modeled utilizing AVL and the cruise speed of 29 m/s. The weight was calculated in ordinance with the Structures specialist and calculated to be 3.26209 kg. To analyze these forces the Trefftz plane represents the cross section of the aircraft with spanwise lift distribution across the wing.

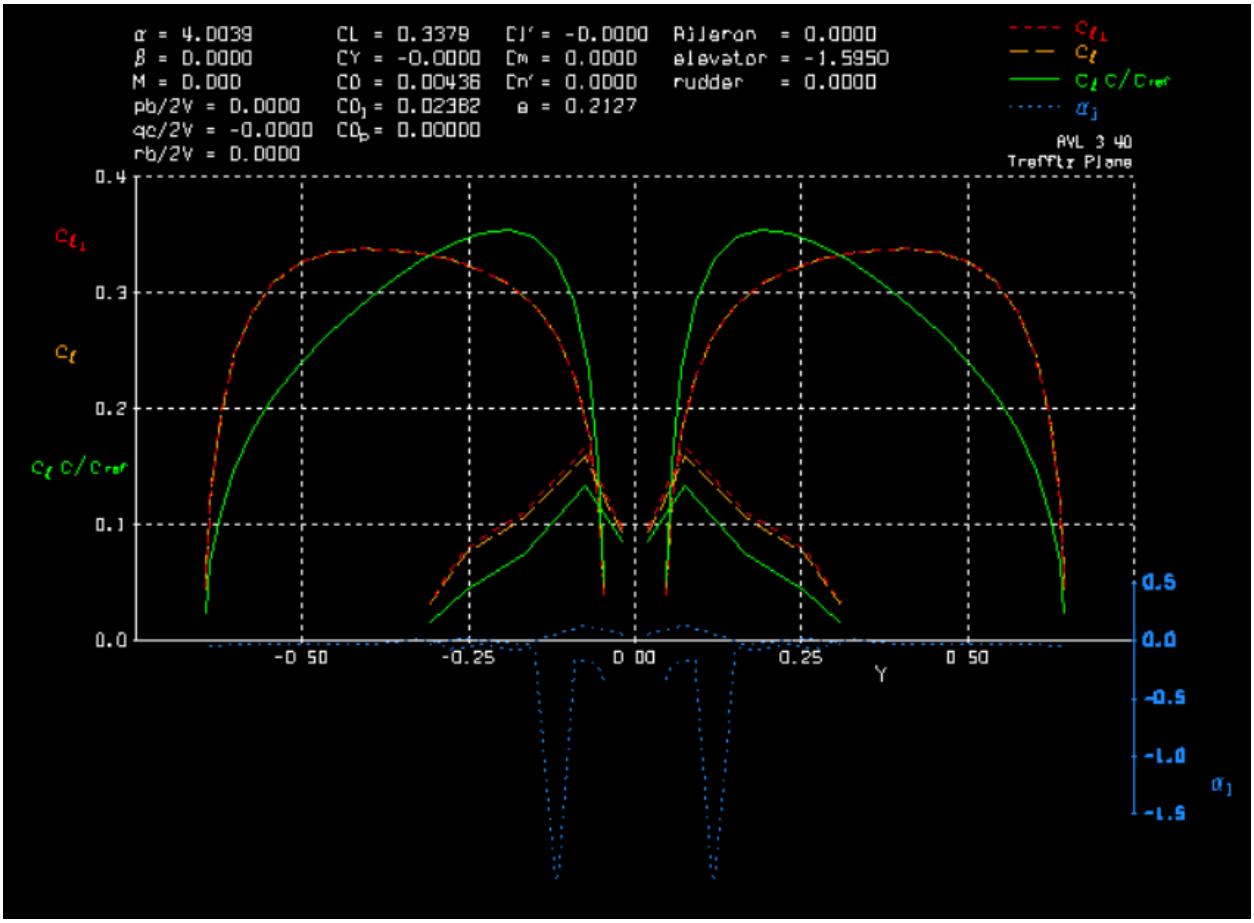

Figure 2.24 Trefftz Plane

The Trefftz Plane plot (Fig 2.24) represents the aerodynamic coefficients of the loads across the aircrafts control surfaces across the spanwise direction (Y). This graph displays the aerodynamic coefficients for the aircraft control surfaces. This is done as a function of spanwise location along the wing. The X axis represents the span distance across the plane while the Y axis represents the various aerodynamic coefficients that are calculated based on loads faced by the aircraft including but not limited to the coefficient of lift, moment, side force, and lift to drag ratio. These forces were calculated at trim conditions so they are equal to zero with respect to the lift, side force, and moment coefficients. This correctly represents the forces for straight and level flight. It can be seen by the graphed lines that the lift coefficient curve shows a typical distribution with higher values near the wing root which decrease towards the wing tip. The moment coefficient indicated the control surfaces contribution to the longitudinal stability. The ratio of coefficient to lift to drag displays the effect across the wing of the induced drag forces that the wing experiences.

2.3.5 Flight Dynamics

For the plane to be stable, the real parts of the eigenvalue poles must be negative. This was obtained successfully with the optimal design case. The poles are represented in the form of $-\zeta\omega_n \pm \omega_d t$ where $-\zeta\omega_n = \sigma$ is the real part and ω_d is the imaginary part of the system. To find the natural frequency $\omega_n = \sqrt{(\sigma^2 + \omega_d^2)}$ and to find zeta $\zeta = \sigma / \omega_n$. These values were calculated for each mode (Table 2.23).

Table 2.23 Mode Analysis

Mode Type	**Eigenvalue Real Part ($-\zeta\omega_n$)**	**Eigenvalue Imaginary Part (ω_d)**	**Natural Frequency (ω_n)**	**Zeta (ζ)**
Roll	-6.8245410	0.0000000	6.824541	1
Dutch Roll	-1.8829395	5.4859092	5.77459	0.3261
	-1.8829395	-5.4859092	5.77459	0.3261
Short Period	-4.3338683	5.9821362	7.3846	0.58676
	-4.3338683	5.9821362	37.3846	0.58676
Spiral	-0.84870237E-01	0.0000000	0.291324	1
Phugoid	-0.47816455E-02	0.39693001	0.39693	0.012
	-0.47816455E-02	-0.39693001	0.39693	0.012

Overall, the aircraft was found to be stable as all of the real parts of the eigne values were negative. The short period mode has a damping ratio of 0.58676, which satisfies the minimum threshold of 0.3, indicating stability in pitch. Its natural frequency is relatively high, ensuring a quick response to control inputs, which enhances maneuverability during flight. The spiral mode controls long term directional stability and spiral convergence or divergence. With a damping ratio of 1.0 the mode is critically damped and will be stable without any divergence. The natural frequency of 0.291324 shows that any spiral tendency will take a long time to develop and can be easily corrected by the pilot control. The Dutch roll mode, which governs yaw and roll stability, has a damping ratio of 0.3261 which is above the minimum of 0.3 but only slightly, meaning the aircraft is stable but could benefit from additional yaw damping. Its natural frequency of 5.77459 suggests a relatively fast response time to control inputs. The phugoid mode, represents the longer period altitude and speed oscillations and had a very weak and low damping ratio of 0.012. Although this is still stable, it has little to none damping which proves that these types of oscillations will take an extended amount of time to settle and may need pilot correction during flight testing. The roll mode shows how the airplane recovers from the roll disturbances and is critically damped with a damping ratio of 1.0, with a large natural frequency of 6.82 it recovers quickly from disturbances, ensuring high stability. The optimally designed wing had all five poles

stable with sufficient damping ratios and natural frequencies. The wing is optimized as well as dynamically stable.

The aircraft had additional parameters that needed to be met beyond static and dynamic stability, including a turn rate of at least 6 degrees per second as well as 3g loading forces. To meet these, an analysis of aircraft performance under loads to be analyzed.

Turn Rate and Loading factor

The aircraft was required to achieve a turn rate of at least 6 degrees per second. The bank angle for the mission required a 70 degree angle, making the load factor, n, equal to 3. This required that the lift force be three times the weight of the airplane to meet mission requirements. To ensure the parametric wing met this design, the coefficient of lift with a cruise speed of 29m/s and 70 degree bank angle was found to be 0.3379. Utilizing this to calculate the force of lift, L, it was found to be 99.51N of lifting force. The weight is 32.01 N, meaning that the ratio of lifting forces is 3.11 which passes the 3g loading factor and therefore can successfully achieve a turn rate of at least 6 degrees per second.

Range and Endurance

$$* \; E = \frac{C\mathcal{V}\eta f}{W}\Pi\eta\frac{C_L^{3/2}}{C_D}\sqrt{\frac{\frac{1}{2}\rho}{W/S}}$$

$$* \; R = \frac{C\mathcal{V}\eta f}{W}\Pi\eta\frac{C_L}{C_D}$$

Figure 2.25 Equation for Endurance and Range

The endurance was calculated based on the speed of 29m/s and the corresponding coefficient of lift and drag was found utilizing AVL (Table 2.21), the battery efficiency n was 95%, the voltage was 22.2 V, the allowable battery discharge *f* was 0.80, and C was 5.2 Amp*s. Utilizing these variables the total endurance was found to be 34.2 minutes. The same constants were utilized for the range, and this was found to be 46.6km. This range and endurance are close in the order of magnitude required for our mission to travel across New York City and therefore is sufficient for flight testing and overall requirements.

2.3.6 Robustness with Respect to Uncertainty in Derivatives

Robustness analysis was studied in order to understand the propagating uncertainties throughout the design process. Such examples include disturbances from wind or unexpected weather conditions throughout the flight. Additionally, there were various assumptions in the modeling through AVL that did not account for aeroelasticity. These assumptions from outside uncontrollable factors as well as assumptions from AVL modeling create propagating uncertainties. This report utilized a Monte Carlo MATLAB iteration to analyze the effects of random variables, which correspond to the uncertainty. It indicated the sensitivity to various uncertainty measurements. The file was able to run 1000 iterations for each independent perturbation and alters the delta change for each variable. These variables which were considered were for the Phugoid, Short Period, and Dutch Roll as well as their respective damping values.

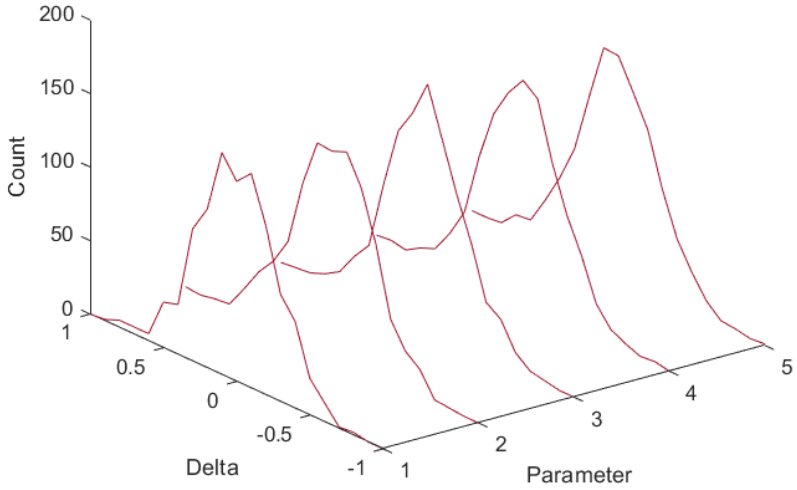

Figure 2.26 Gaussian Assumption for Monte Carlo

Figure 2.26 displays a 3D line plot that visualizes the distribution of various parameters in response to the "Count." The red lines trace how the variable changes as both variables fluctuate, with their shape higher and lower frequencies for specific values. The plot reveals a periodic pattern, with the count rising and falling in cycles, suggesting a Gaussian distribution.

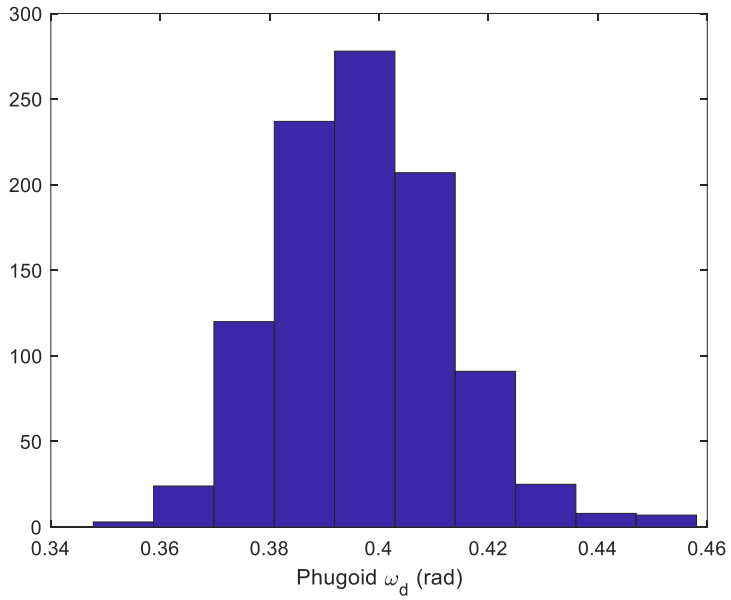

Figure 2.27 Phugoid Damping frequency

Figure 2.27 shows a histogram representing the distribution of Phugoid ω_d (rad). The x-axis represents the values of the phugoid frequency, ranging from approximately 0.34 to 0.46

radians. The y-axis indicates the count of occurrences, with values ranging from 0 to around 300. The histogram is plotted using blue bars, which show the number of observations in each range of the ω_d values. The plot suggests a normal or Gaussian distribution with a peak around 0.4 radians, indicating that most of the data points are centered around this value. This aligned with expected results. The true frequency corresponded to 0.39 radians and is therefore within this optimal range. The phugoid frequency is crucial for understanding the aircrafts pitch stability and represents the oscillations between altitude gain and loss. The frequency value directly influences how the aircraft responds to the disturbances in pitch. The gaussian distribution shows the stable and controlled oscillations which allow for smooth flight operations. This factor is important to maintaining overall flight stability and responses to flight disturbances

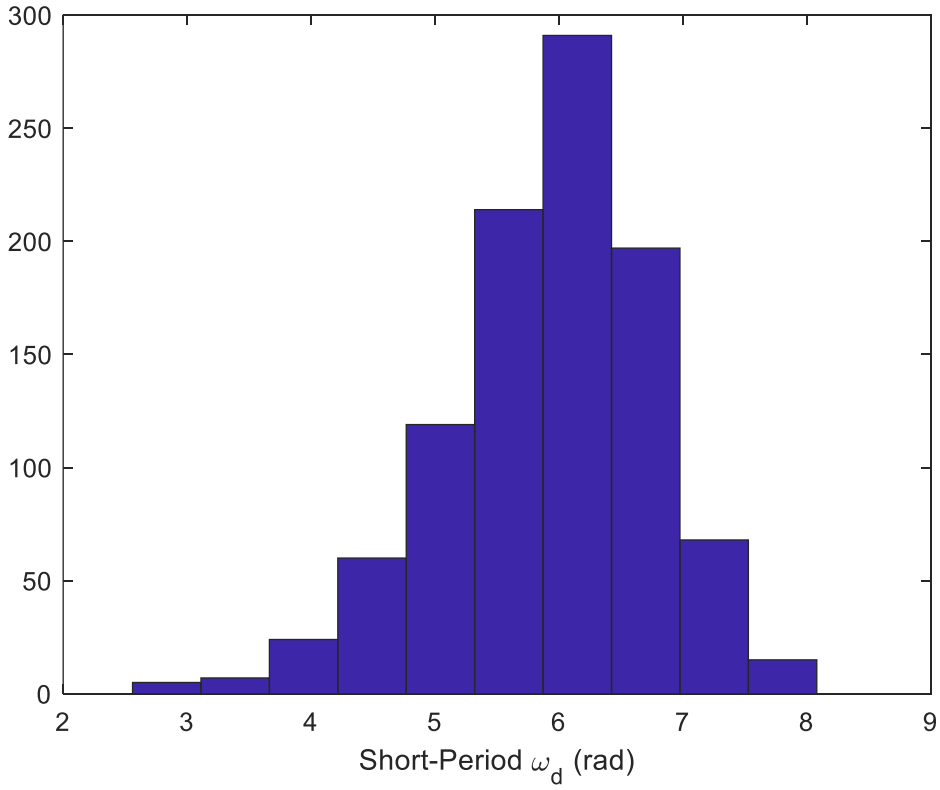

Figure 2.28 Short Period damping frequency

Figure 2.28 displays a histogram representing the distribution of the Short-Period ω_d (rad) frequency. The x-axis shows the range of values for ω_d which is the frequency of the short-period oscillation in radians ranging from about 2.5 to 8 radians. The y-axis shows the count of occurrences for each parameter. The histogram reveals that the ω_d values are most concentrated and peak around 6 radians. The true short period damping frequency was found to be 5.98 rads, well within the range. The distribution follows a Gaussian pattern with a slight right skew, which follows the expected behavior. For importance in flight dynamics, the short period mode represents the aircrafts response to a rapid change in pitching oscillations. It is important to ensure this value remains within the expected range so that the aircraft performance can be controlled under disturbances.

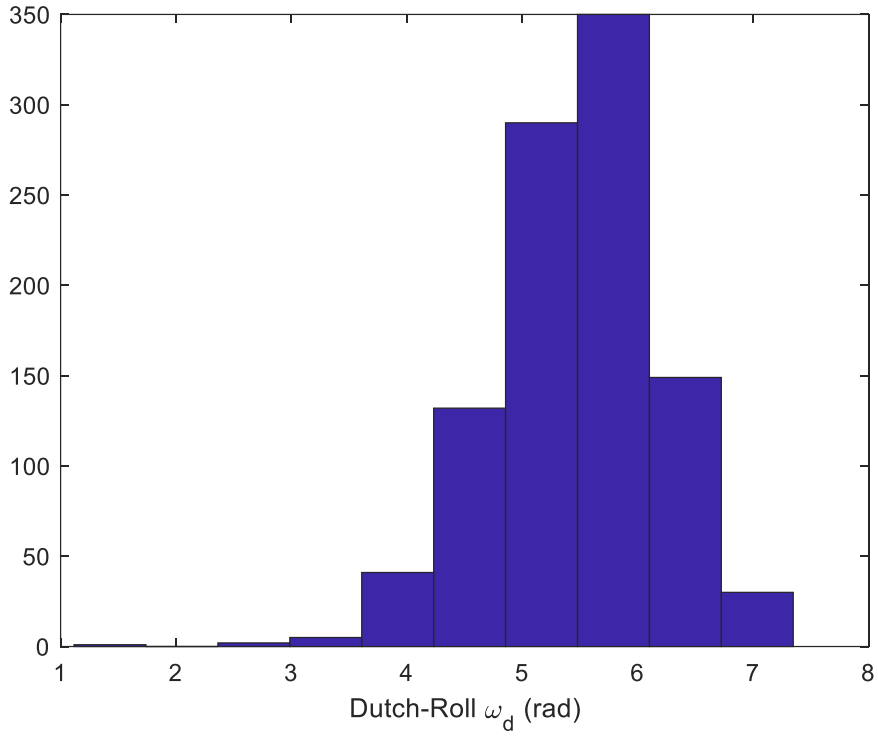

Figure 2.29 Dutch Roll damping frequency

Figure 2.29 presents a histogram that shows the distribution of the Dutch-Roll ω_d (rad) frequency. The x-axis represents the values of ω_d, which correspond to the frequency of the Dutch-roll oscillation in radians, ranging from about 1 to 7.5 radians. The y-axis shows the count of occurrences for each parameter, with values up to approximately 350. The histogram indicates that the majority of the data points are concentrated around the 5-6 rad range, with a peak near 5.5 radians. This suggests that most of the observed Dutch-roll frequencies lie within this range, with fewer occurrences at the extreme ends of the spectrum. The true dutch roll damping frequency was found to be 5.48 radians which aligned well within optimal range. This pattern is a Gaussian distribution as expected for this parameter. The Dutch Roll mode is associated with oscillations and disturbances in the lateral-directional stability. A well damped system corresponds to effective recovery from small perturbations in the system. Maintaining a Dutch Roll frequency within optimum range is important for ensuring that the aircraft remains stable during lateral and directional movements throughout flight, responding predictably to roll and yaw.

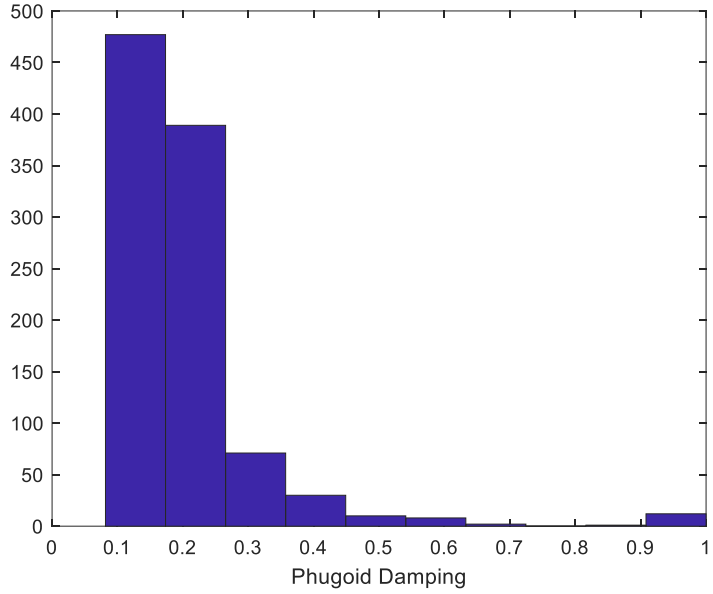

Figure 2.30 Phugoid Damping Monte Carlo

Figure 2.30 shows a histogram representing the distribution of Phugoid Damping, which corresponds to the rate at which the oscillations in the phugoid mode decay over time. The x-axis represents the damping values, ranging from 0 to 1, where 0 indicates no damping and 1 which is critically damped oscillations. The y-axis shows the count of occurrences for each damping value. It can be seen that most of the data points are concentrated around lower damping values, with a peak around 0.1, however the distribution is not Gaussian and is more skewed to the left. The true value was 0.012, which is very low and less than the peak performance values. Low damping values are more common with aircrafts which have little to no damping. This makes aircraft recovery from disturbances more difficult. For flight performance, the phugoid damping is important as it displays how quickly the aircraft recovers from disturbances in altitude. Considering our flight mission remains mainly at constant 100m altitude for all flight, this variable is not as critical.

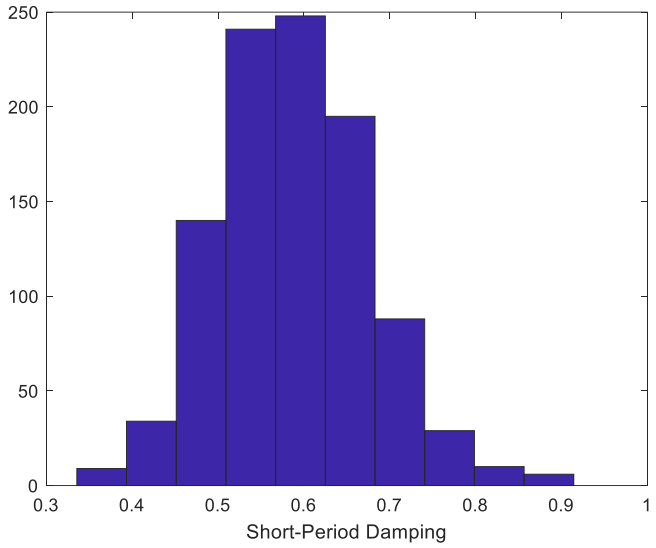

Figure 2.31 Short Period Damping for Monte Carlo

Figure 2.31 shows the histogram for the Short Period Damping with ranging values between 0.35 to 1. The x axis corresponds to the damping values in which zero indicates no damping and 1 represents the critically damped state. The Y axis represent the count of the occurrences for each damping value after 1000 runs propagating uncertainty. The true short period damping value is 0.5867 which lies well within the optimal range. This graph does mimic Gaussian behavior and is slightly skewed to the left. The Short Period damping is related to maintaining pitch stability and ensuring that the aircraft can recover quickly from disturbances without extreme oscillations in the aircrafts pitch. Maintaining the short period damping within this stable range around 0.6 is important in ensuring that the pitch oscillations remain stable without extreme oscillations which cannot be corrected with pilot control.

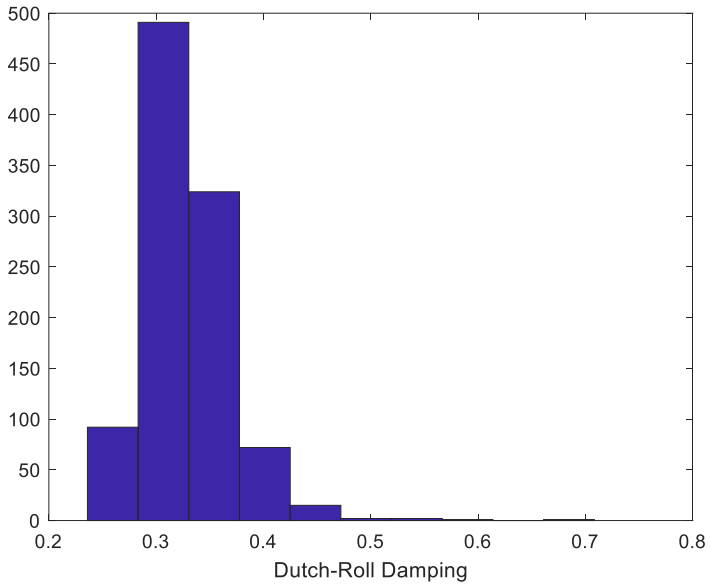

Figure 2.32 Dutch Roll Damping

Figure 2.32 represents the distribution of Dutch-Roll Damping, with values ranging from around 0.2 to 0.8. The x-axis shows the damping values, where 0 indicates no damping and 1 indicates critical damping, leading to the cessation of oscillations. The y-axis represents the count for each damping value. The histogram reveals that the majority of the data points fall within the 0.2 to 0.4 damping range, with the highest frequency occurring around 0.3 damping. The true value was found to be 0.326 which was well within optimal range. This suggests that most of the systems in the dataset have relatively low damping for the Dutch-roll mode, which results in moderate oscillations in yaw and roll. Optimization within this range is important for controlling oscillations in aircraft's lateral and directional stability.

These behaviors display the properties of Robustness and how they affect the aircraft's performance, with propagating uncertainties. Various factors in flight testing are not considered and therefore have various assumptions. These assumptions propagate uncertainties throughout aircraft testing. It is important to analyze the behavior of each variable and how it affects the stability and control of the aircraft. Ensuring that the true values are within the optimal ranges for these parameters will allow for the best performance.

3. Structures

3.1 Design

This section details the structural design of a wing to meet both a stiffness and mass requirement. This ensures that the final product is structurally sound for flight over populated areas while maintaining enough mass budget to carry payloads for the customer. A cost function is defined, and both a parametric and optimal design are covered and evaluated with the cost function.

3.1.1 Problem Statement

The multi-dimensional objective of this design was to create the structure for a specified wing geometry that meets a required wingtip deflection based on its span while also minimizing its mass below a determined mass budget. Specifically, the deflection requirement was for the wingtip to deform 25.4 ± 1.27 millimeters for every 1.829 meters of span under three times the wing loading at trim for the aircraft. The geometry for each wing was found by the aerodynamics specialist and the total span, after considering fuselage mounting, was found to be 1.884 meters. This means the target deflection for this design was 26.164 ± 1.27 millimeters. The weight budget was determined by the avionics specialist, and it was required that the designed wing have a mass less than 301 grams, with the goal to have the mass as low as possible while maintaining enough stiffness to meet the target deflection.

The design space was constrained by the geometric values determined by the aerodynamics specialist. Geometric values such as the span, taper, and airfoil shape all acted as constraints as to how large the spar could be, where stringers could be located, and hard points for mounting servos and landing gear. Geometric constraints paired with the conflicting objectives of reducing mass while maintaining a required stiffness created a complex problem that required a cost function with which to evaluate different designs. A cost function was created to addresses two simultaneous costs with terms for both mass and deflection (3.1). In the first term, the calculated mass (m) is normalized by the maximum allowable mass ($m_{max} = 301$ g). In the second term, the measured deflection (δ) is subtracted from the target deflection (δ_{target} = 26.164 mm) to find the error in deflection which is normalized by the maximum allowable deflection error ($\delta_e = 1.27$ mm).

$$J(m, \delta) = \left(\frac{m}{m_{max}}\right) + 2\left(\frac{\delta_{target} - \delta}{\delta_e}\right)^2 \tag{3.1}$$

It is important to note that in (3.1), the deflection term is squared. Aside from assuring this term was positive regardless of if there was too much or too little deflection, the square heavily penalizes designs which don't fall in the required deflection range. For designs that approach the target deflection within the allowable error, the square makes this term much smaller giving more influence to the mass term. Additionally, a weighting coefficient of 2 was assigned to the deflection term to emphasize its greater importance relative to minimizing the mass, as most designs during parametric design already fell below the max allowable mass. However, this still allows the mass to be minimized further without compromising the deflection goal. The main parameters, or design variables, that were altered to affect both the deflection and mass of the wing were spar diameter, stringer dimensions, and spar/stringer material. The process behind selection of these parameters is discussed in Section 3.1.2.

3.1.2 Parametric Design

The variables used in the parametric design of this wing were stringer width/height, stringer material, spar diameter, and spar material. These parameters were incrementally varied while the mass and deflection were measured using SolidWorks. To select these design variables a singular wing was initially assumed to be a cantilever beam under a distributed load. Under this assumption, the deflection (δ) at the free end of the wing/beam (with length a, modulus of elasticity E, and moment of inertia I) under a distributed load (q) is given by (3.2).

$$\delta = \frac{qa^4}{8EI} \tag{3.2}$$

The length is defined by the span of the wing and is set by aerodynamic needs. The force and location of the force are also unalterable and the result of aerodynamics from the AVL determined geometry. This leaves the modulus of elasticity and the area moment of inertia as design variables. The area moment of inertia for the rectangular cross-section stringers are given by (3.3) where *w* is width and *h* is height. The area moment of inertia for the spar with a circular cross section is given by (3.4) in which *d* is diameter.

$$I_{stringer} = \frac{1}{12}wh^3 \tag{3.3}$$

$$I_{spar} = \frac{1}{64}\pi d^4 \tag{3.4}$$

From (3.3) and (3.4) we can see that the area moment of inertia is a function of the dimensions of the cross-section. So, by increasing or decreasing the width, height, or diameter of the stringers/spar, it effectively increases or decreases the stiffness of the wing while also affecting the mass of the wing. Additionally, modulus of elasticity is a material property so by changing the material of structural components like the spar and stringers, it will also affect both the stiffness and mass of the wing.

With design variables selected, it was then necessary to set up a SolidWorks simulation to test the predicted deflection for different design iterations and record the weight of the resulting design. To simulate the loading condition described in Section 3.1.1, statics principles were applied. At trim, the total lift generated by the wings is equal to the force of gravity acting on the aircraft. Additionally, this load is distributed over the wing in the shape of an ellipse [2]. This distributed load is equivalent to the total load applied at the centroid of the lift distribution. For one wing, this would be at the centroid of a quarter ellipse. The total load for one wing was found to be 55.917 Newtons and the spanwise location ($\overline{x}$) was found using (3.5) to be 0.386 meters from the fuselage. Aerodynamic forces act through the aerodynamic center of an airfoil. For a NACA 0012 airfoil this point is located at the quarter chord [4]. Thus, the complex distributed wing loading can be described by a 55.917 N point force acting at a spanwise location of 0.386 meters on the quarter chord of the wing.

$$\overline{x} = \frac{4a}{3\pi} \tag{3.5}$$

The SolidWorks simulation was set up under the assumption that connections to the fuselage were a fixed geometry and the simulations were run without the rest of the plane in the model to reduce the time required for meshing (Fig. 3.1). The loading conditions were applied and after each iteration, changes to the design variables were made using relationships derived from (3.2) through (3.4), to minimize the weight of the wing while achieving a deflection within tolerance (Fig. 3.2).

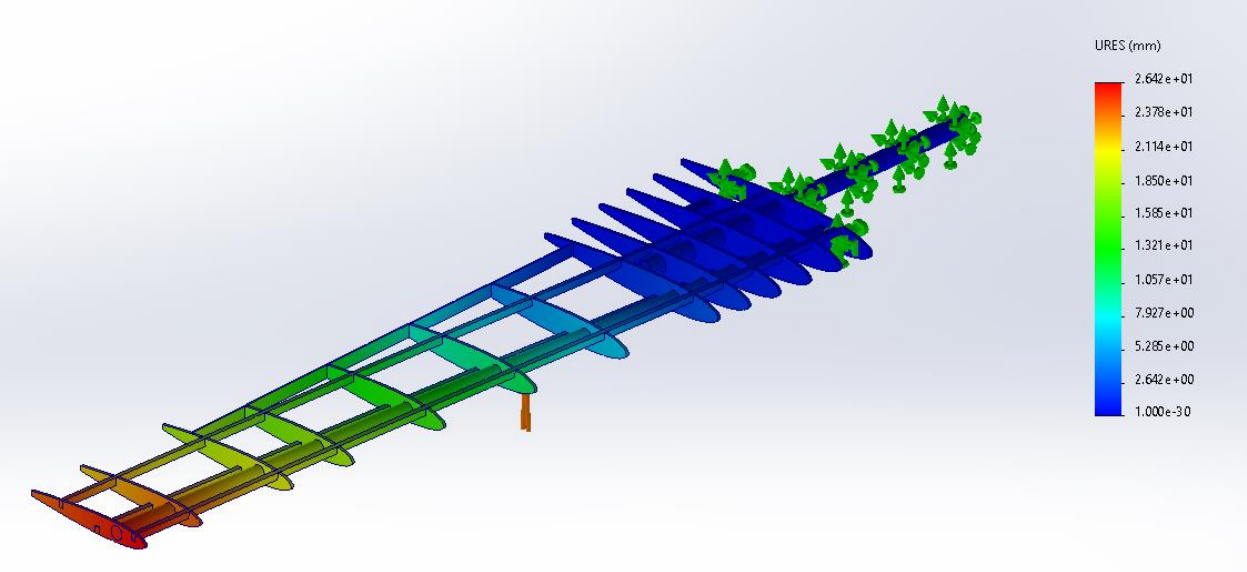

Figure 3.1. Deflection Testing Setup for Parametric Wing

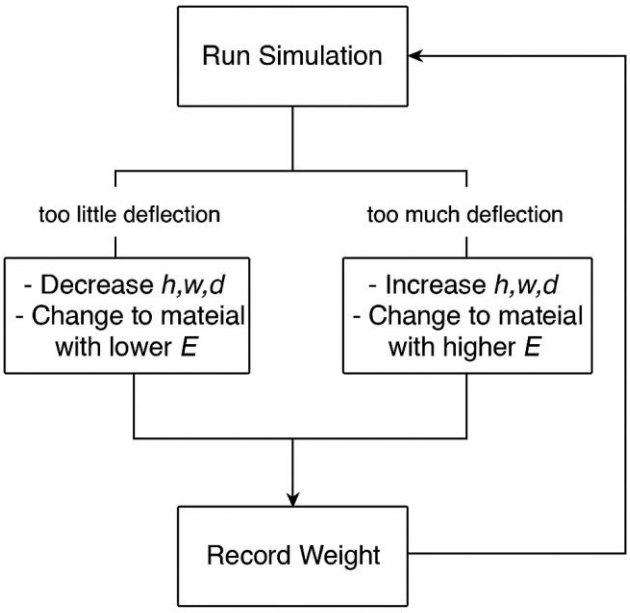

Figure 3.2. Flowchart Describing Parametric Design Variable Changes

SolidWorks simulations were run without large displacement calculations active due to limitations in computing power. Several iterations with varied design variables and the resulting weight and displacement are detailed in Table 3.1. The stringer height is given as *h,* the stringer width is given as *w*, and the spar diameter is given as *d*. Each dimension is followed by YP for American Yellow Poplar or RO for American Red Oak.

Iteration	Stringer (*w* x *h*) [mm]	Spar (*d*) [mm]	Deflection [mm]	Mass [g]	Cost
1	6.350 x 3.175 – YP	9.652 – RO	42.820	137.770	344.462
2	6.350 x 6.350 – YP	9.652 – RO	35.150	157.960	100.655
3	6.350 x 6.350 – YP	10.688 – RO	32.890	166.030	56.648
4	6.350 x 6.350 – RO	10.688 – RO	31.480	185.840	35.660
5	6.350 x 6.350 – YP	12.700 – RO	28.850	184.590	9.559
6	6.350 x 6.350 – YP	13.716 – RO	26.930	195.070	1.376
7	6.350 x 6.350 – YP	13.970 – YP	27.470	172.720	2.689
8	6.350 x 7.620 – YP	13.970 – YP	26.250	180.790	0.610
9	5.080 x 7.620 – YP	14.478 – YP	27.630	174.890	3.246
10	5.080 x 7.620 – YP	14.732 – YP	27.130	176.840	1.745
…	…	…	…	…	…
Final	5.080 x 7.620 – YP	14.783 – YP	26.420	157.040	0.603

Table 3.1. Iterations for Parametric Structures Design

During parametric design, over 20 iterations were tested. Only the first 10 iterations and final iteration are shown in Table 3.1 as the initial iterations offer the most insight into the parametric design process detailed in Fig. 3.2. Design iterations not listed in Table 3.1 include minor changes following the preliminary design report based on requirements from other specialists – these are covered in more detail in Section 6. The highlighted rows in Table 3.1 show designs that met both the weight and deflection criteria. The final design was selected because it had the lowest cost function value, according to (3.1). Design iteration 8 deflected closest to the target deflection of 26.164 millimeters, however, the final iteration had a lower cost function value due to having a lower mass. This helps to conceptualize (3.1) because both designs fall close to the target deflection value which reduces the deflection term to a very small value, giving more emphasis to the mass term. The final parametric design had a spar diameter of 14.783 millimeters and a stringer cross section of 5.080 x 7.620 millimeters – both with yellow poplar as a material (Fig. 3.3).

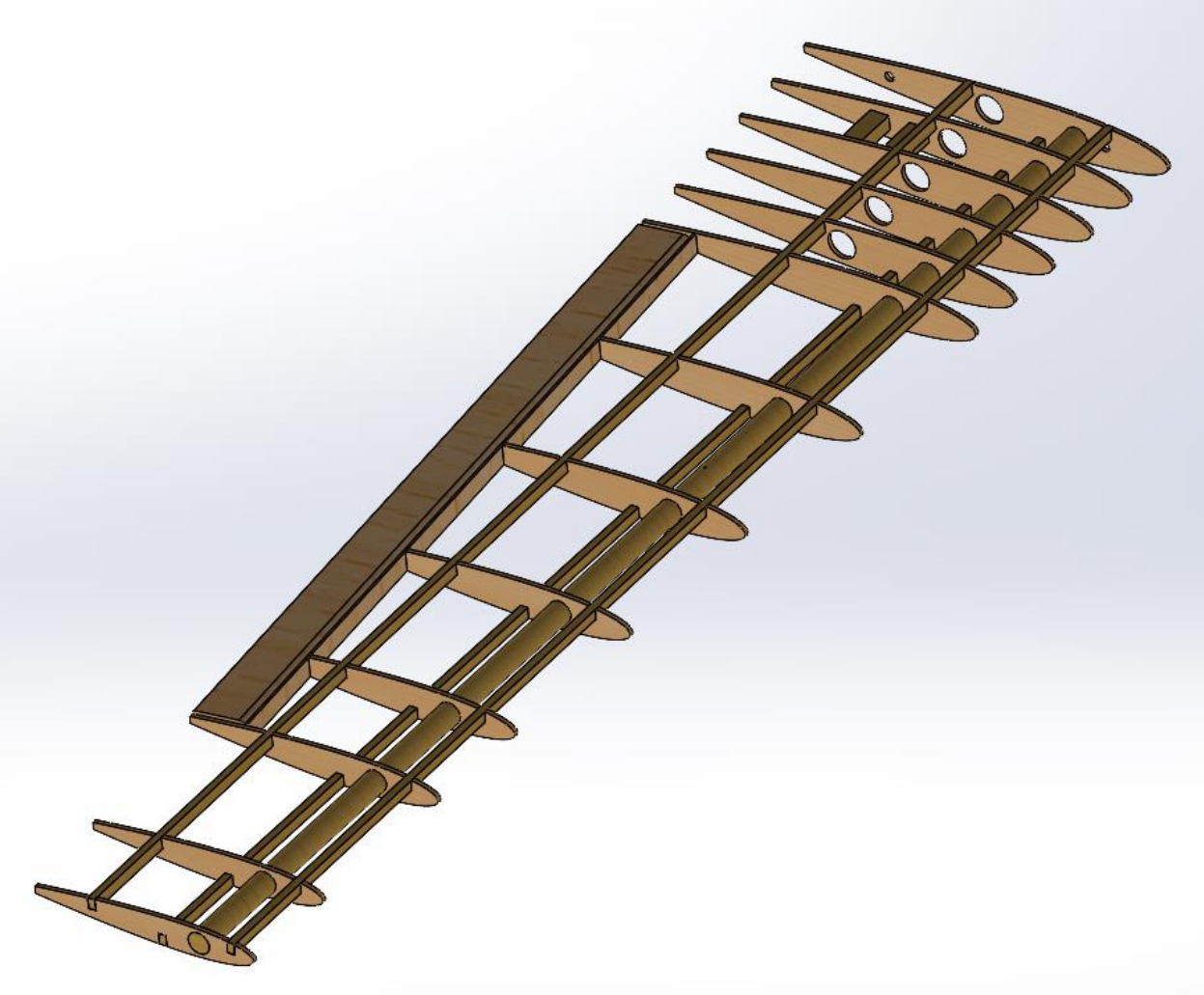

Figure 3.3. Final Parametric Design

3.1.3 Optimal Design

Although an acceptable design was found during the parametric design process, optimization techniques were used in an attempt to further minimize the cost function value for this design. A technique known as Kriging was used to create a surrogate model that uses radial basis functions to curve fit the relationship between design variable changes and the resulting cost function value [5]. Another important aspect of Kriging is that it includes a function that calculates expected improvement (E.I.). Expected improvement is based on advanced statistical analysis that considers curvatures and Gaussian distribution of variances which it uses to predict the next set of simulations to run to find the best curve fit [5]. This is extremely valuable in the context of this design because changing the model between iterations and running finite element analysis is time consuming. In concept, Kriging should produce a reliable curve fit with fewer data points (simulations).

Kriging builds a model that interpolates between design points, so it was necessary to choose continuous design variables. Of the design variables discussed in Section 3.1.2, all are continuous – that is they can take on any value within a range – *except* for spar/stringer material. As a result, the design variables chosen for the optimization process were spar diameter and stringer side length, while the material of each was held constant as yellow poplar. It is important to note that for this portion of the design process, the stringers are assumed to have a square cross section. This was done to simplify the simulation process and reduce the number of changes that had to be made to the model between iterations.

The optimization process began with the same basic design as the final iteration of the parametric design as shown in Fig. 3.3. The materials and spar/stringer/rib location remained constant from the final parametric design so only the cross section of the spar and stringer were varied. The maximum value of the spar diameter was determined based off the size of the smallest rib – to allow for at least 2.5 millimeters of rib material on all sides of the spar. The same criterion was used for determining the maximum stringer side length. This was done to ensure that each rib, although not highly load bearing, maintained structural integrity. The minimum values of the spar diameter and stringer side length were selected based off prior knowledge gained through parametric design. The ranges of each design variable are shown in Table 3.2.

Design Variable	Minimum [mm]	Maximum [mm]
Spar Diameter (*d*)	7.50	16.94
Stringer Side Length (*a*)	3.00	7.62

Table 3.2. Design Variable Ranges for Structures Optimization

These ranges were then input to a MATLAB code which utilized Latin Hypercube Sampling (LHS) to determine an initial set of design points. LHS splits each factor (spar diameter or stringer side length) into different levels (value of diameter or side length) and assigns them to runs (simulation iterations) such that every level of each factor is analyzed, and different levels of different factors are mixed [5]. LHS helps to avoid testing the minimum range of both factors within the same run, as this would clearly not provide much insight. The initial data points found from the LHS code along with the associated deflection, weight, and cost value for each run are shown in Table 3.3.

Run	Spar (*d*) [mm]	Stringer (*a*) [mm]	Deflection [mm]	Mass [g]	Cost
1	9.860	3.000	57.570	94.830	1223.375
2	12.220	7.620	25.620	158.700	0.894
3	7.500	5.310	44.190	103.460	403.266
4	16.940	6.465	21.310	178.840	29.810
5	14.580	4.155	31.880	134.010	40.959

Table 3.3. Structures Optimization Iterations 1-5

The cost function values calculated for the first 5 design points were then input into a MATLAB code which performed Kriging. An initial prediction of the curve fit was created based off the cost value of the five points and the associated design points from the previous script (Fig. 3.4). Additionally, a plot of the E.I. was created to show where design points were expected to improve the curve fit the most (Fig. 3.5).

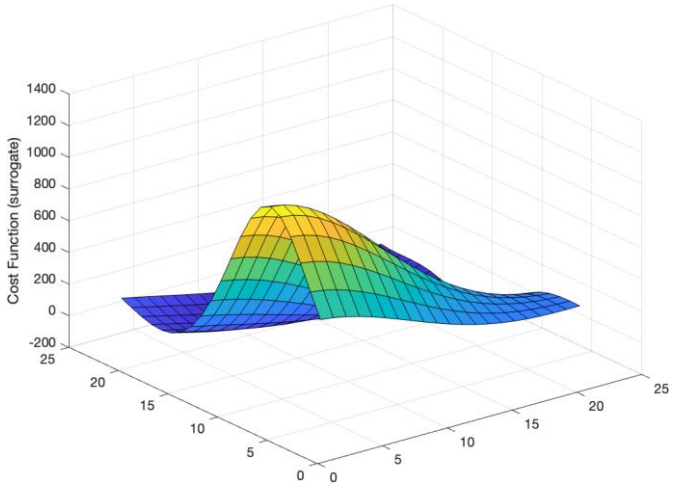

Figure 3.4. Surrogate model after 5 Design Points

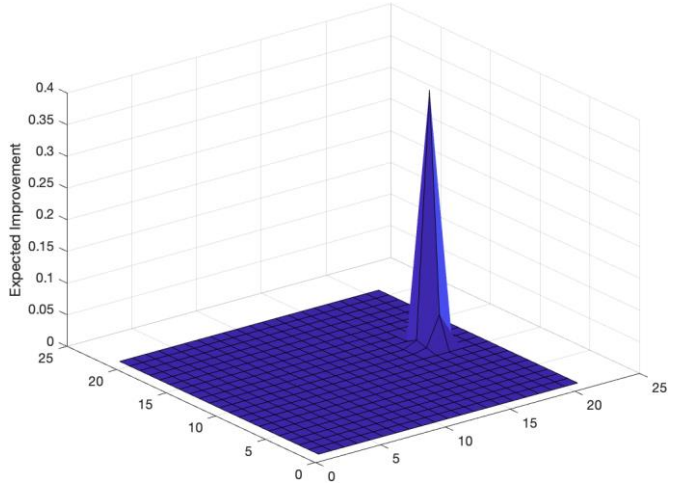

Figure 3.5. EI after 5 Design Points

It was predicted after 5 design points that the surrogate minimum was -14.617 at a spar diameter of 15.524 millimeters and a stringer side length of 5.541 millimeters (Fig. 3.4). The E.I. function predicted that the next best design points to test all fell between a spar diameter of 12-13 millimeters and a stringer side length of 6.5-7 millimeters (Fig. 3.5). The specific design points are displayed in Table 3.4 along with the simulation results and cost function values.

Run	Spar (*d*) [mm]	Stringer (*a*) [mm]	Deflection [mm]	Mass [g]	Cost

6	12.692	6.927	27.230	151.570	1.913
7	12.22	6.927	27.980	148.430	4.582
8	13.164	6.927	26.290	154.820	0.534
9	12.692	6.696	27.870	148.360	4.102
10	12.22	6.696	28.620	145.230	7.962

Table 3.4. Structures Optimization Iterations 6-10

From Table 3.4 and 3.3, designs which don't meet the required deflection range are heavily penalized in the cost function despite having relatively similar weights. This makes sense when recalling equation (3.1) due to the additional weighting put on the deflection term. The cost function values in Table 3.4 were entered into a MATLAB script along with the accumulation of data from the previous script. With data for 10 total design points, the plot of the surrogate model was updated (Fig. 3.6) along with the E.I. (Fig. 3.7).

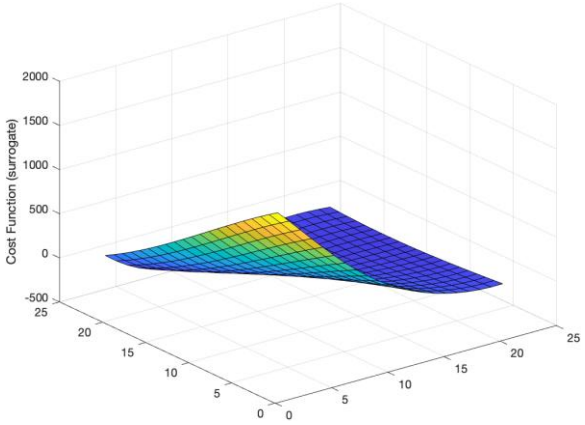

Figure 3.6. Surrogate Model after 10 Design Points

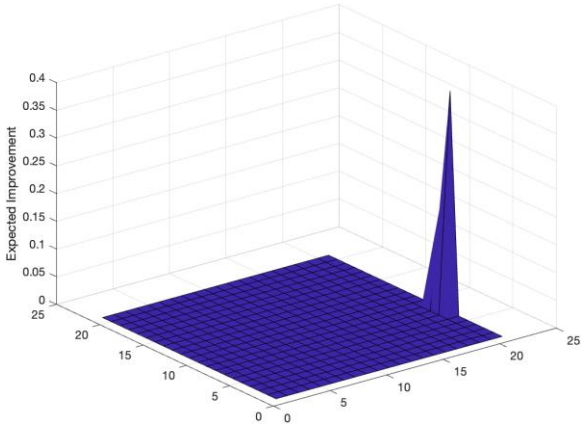

Figure 3.7. EI after 10 Design Points

It was predicted after 10 design points that the surrogate minimum was -166.019 at a spar diameter of 16.940 millimeters and a stringer side length of 4.386 millimeters (Fig. 3.6). The E.I. function predicted that the next best design points to test all fell between a spar diameter of 9.8-

11.3 millimeters and a stringer side length of 7.3-7.62 millimeters (Fig. 3.7). It is interesting to note that the E.I. function predicts the best curve fitting will occur with more points near the maximum stringer side length. This process was repeated 2 more times, and the iterations are summarized in Table 3.5. Additionally, the resulting surrogate model and EI plots are shown in Fig. 3.8 through 3.10.

Run	Spar (*d*) [mm]	Stringer (*a*) [mm]	Deflection [mm]	Mass [g]	Cost
11	10.332	7.620	28.350	147.350	6.415
12	10.804	7.620	27.860	150.010	4.065
13	11.276	7.620	27.370	152.790	2.311
14	9.860	7.620	28.860	144.810	9.494
15	10.804	7.389	28.480	146.480	7.138
16	10.332	7.620	28.350	147.350	6.415
17	9.860	7.620	28.860	144.810	9.494
18	10.804	7.620	27.860	150.010	4.065
19	9.388	7.620	29.390	142.380	13.378
20	11.276	7.620	27.370	152.790	2.311

Table 3.5. Structures Optimization Iterations 11-20

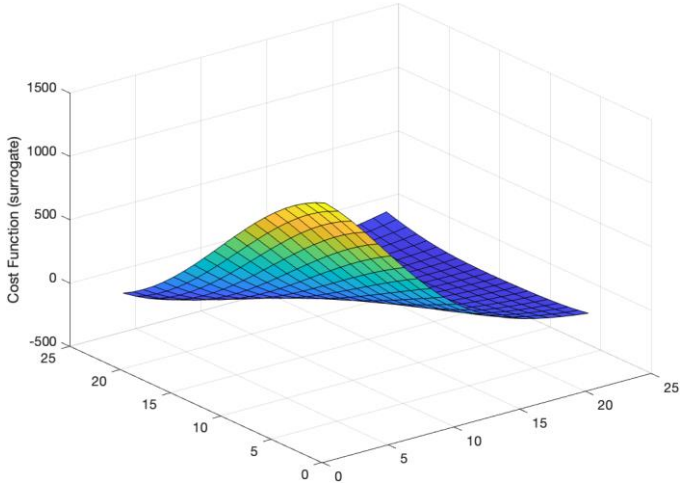

Figure 3.8. Surrogate Model after 15 Design Points

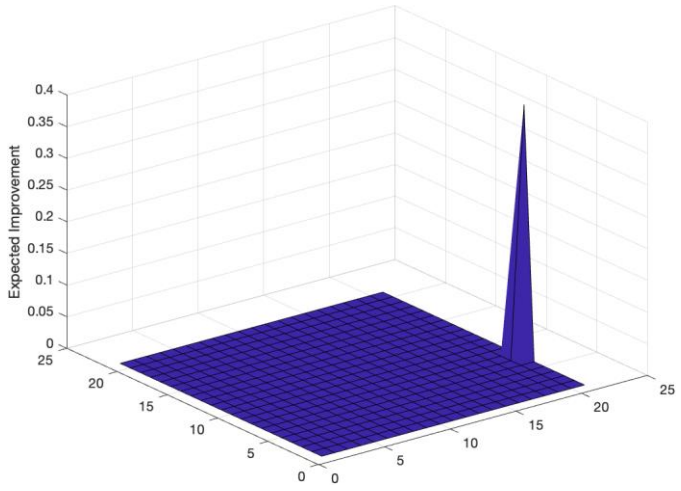

Figure 3.9. EI after 15 Design Points

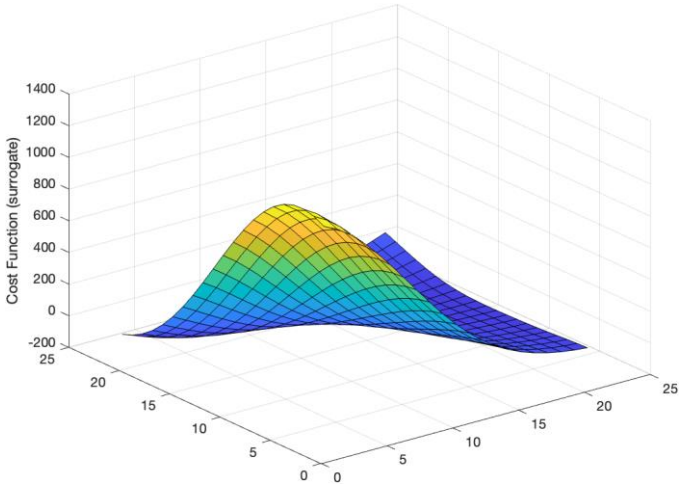

Figure 3.10. Surrogate Model after 20 Design Points

Looking at the results from Table 3.5, the algorithm appeared to converge because for iterations 16-20, E.I. predicted all of the same design points that were tested in previous iterations aside from one (run 19). The predicted surrogate minimum after 15 design points was -138.139 at a spar diameter of 16.940 millimeters and stringer side length of 4.152 millimeters (Fig. 3.8). After all 20 design points, the surrogate minimum was predicted to be -124.087 at a spar diameter of 16.940 millimeters and stringer side length of 3.985 millimeters (Fig. 10). This small change in prediction makes sense when considering only one truly new design point was tested between runs 16 and 20 (Table 3.5). The surrogate minimum prediction after 20 total runs was tested and the results are shown in Table 3.6. The model predicted that cost was minimized for a design that has the maximum spar diameter and an intermediate stringer side length (Fig. 3.11).

Spar (*d*) [mm]	Stringer (*a*) [mm]	Deflection [mm]	Mass [g]	Cost
16.940	3.985	26.300	152.440	0.529

Table 3.6. Final Optimization Design Results

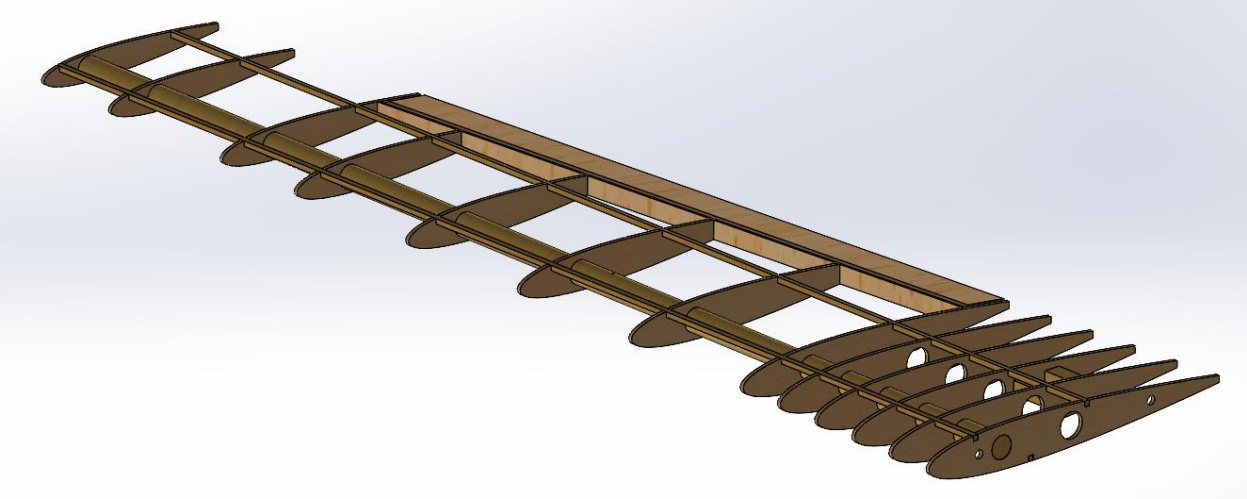

Figure 3.11. Optimal Design Wing

The design variable values in Table 3.6 represent the optimal design based off curve fitting of the cost function. The optimized design has the lowest cost function out of all 20 design points tested. It is interesting to note that the surrogate model was very far off in predicting the actual cost function value at this point. Looking at (3.1), it is not possible for the cost function to have a negative value, yet the surrogate model predicted a cost of -124.087. Nevertheless, the optimization was successful in identifying the design variable values that minimize cost. The optimization identified early on that maximizing the spar diameter resulted in the lowest cost function and further iterations just changed the stringer side length prediction.

3.2 Wing

Selection of the final design considered both the parametric (Section 3.1.2) and optimization (Section 3.1.3) studies. The final designs from each were compared using (3.1) and the design with the lowest cost function value was selected. This section covers only the better of the two designs.

3.2.1 Selected Design

The final designs from both the parametric analysis and optimization analysis are compared in Table 3.7. Both designs meet the deflection and mass requirements, however, the optimal design is closer to the target deflection of 26.164 millimeters and is slightly lighter than the parametric design. The cost function values reflect this as both designs have relatively low cost compared to past iterations, but the optimal design is slightly lower at 0.529 (Table 3.7).

Design	Spar (*d*) [mm]	Stringer [mm]	Deflection [mm]	Mass [g]	Cost
Parametric	14.783	5.080 x 7.620	26.420	157.040	0.603
Optimal	16.940	3.985 x 3.985	26.300	152.440	0.529

Table 3.7. Parametric and Optimal Design Comparison

The optimal design was selected which features a rib-spar construction with yellow poplar spar and stringers with cross section dimensions of 16.940 millimeters and 3.985 x 3.985 millimeters, respectively (Fig. 3.11). The ribs are made from 3-millimeter-thick balsa and vary in chord length according to the taper of the wing. The chord length at the root is 255 millimeters and the chord length at the wing tip is 153 millimeters (Fig. 3.12). The ribs are spaced 38.1 millimeters apart near the root of the wing to provide additional rigidity to the partial aluminum spar which connects the wing to the fuselage (see Section 3.3.4 for fuselage mounting). The remainder of the ribs are spaced 114.3 millimeters apart – with exceptions for aileron mounting and span requirements. The aileron material is balsa, and the dimensions were specified by the aerodynamics specialist (Fig. 3.12). Additional parts include the beam for aileron mounting, and the landing gear mounting blocks, both made from yellow poplar for increased rigidity.

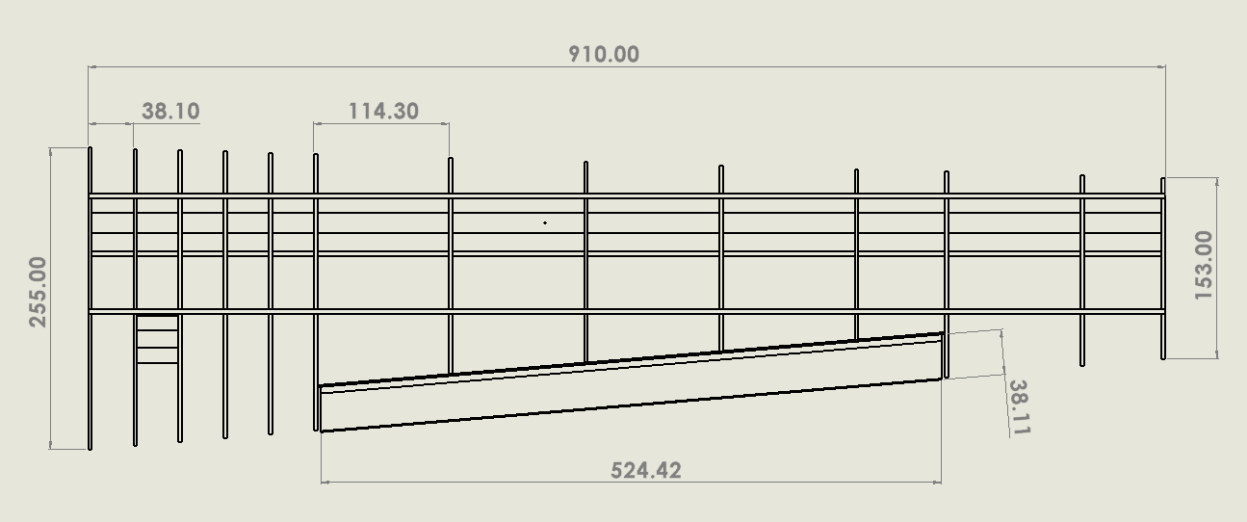

Figure 3.12. Top View of Final Wing Design Structure

The total weight of this design is 152.440 grams which demonstrates an improvement over both the stock wing, and parametrically designed wing. The selected design can be seen in Fig. 3.13 with a monokote covering to show how it would appear after full construction.

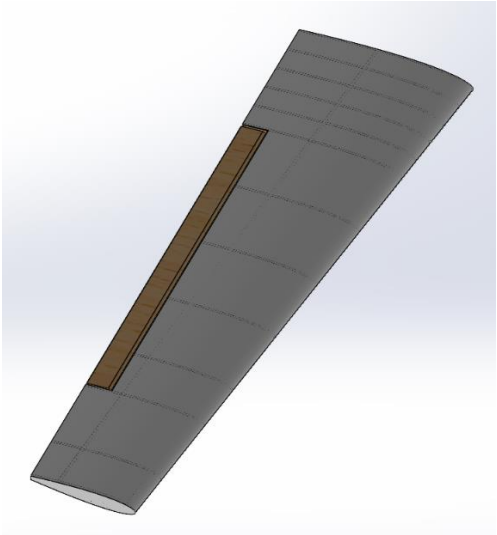

Figure 3.13. Selected Wing Design

3.2.2 Robustness Analysis

The mass and deflection of the final design discussed in Section 3.2.1 are not directly measured values, but rather estimations based off computer aided modeling and finite element analysis. There is an uncertainty associated with these software-calculated values based on different factors such as meshing quality. Furthermore, when the wing is manufactured, more uncertainties are introduced with build quality, measurement tolerances, and material defects. To determine the robustness of the design with respect to uncertainty, a Monte Carlo simulation can be used [5]. A Monte Carlo simulation introduces uncertainty to a model by randomizing variables. By running many iterations with certain variables randomized, it is possible to get an idea of how the design reacts to uncertainty in those variables [5]. Using MATLAB for this analysis, an uncertainty was introduced to the mass and bending stiffness (*EI*) at the root, midspan, and tip of the wing (Fig. 3.14). A Gaussian uncertainty was assumed for variations of these parameters (Fig. 3.15). Note that for this simulation, the input for *EI* at all three locations was approximated to be the same and was calculated using the deflection listed in Section 3.2.1 with a rearranged form of (3.2) for the point loading described in Section 3.1.2.

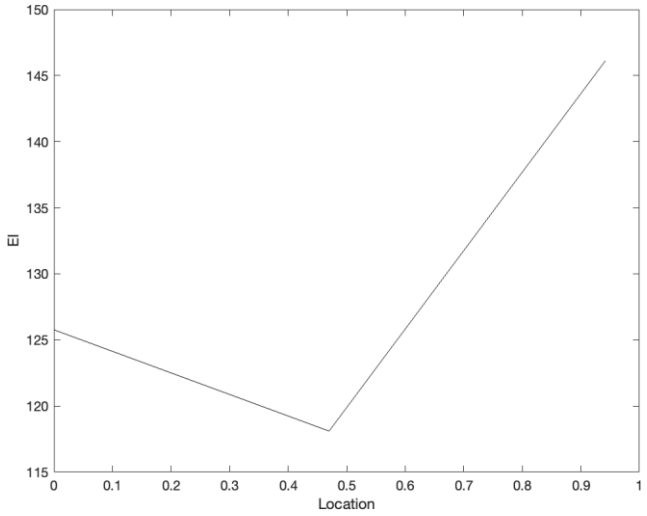

Figure 3.14. EI Variation with Spanwise Location

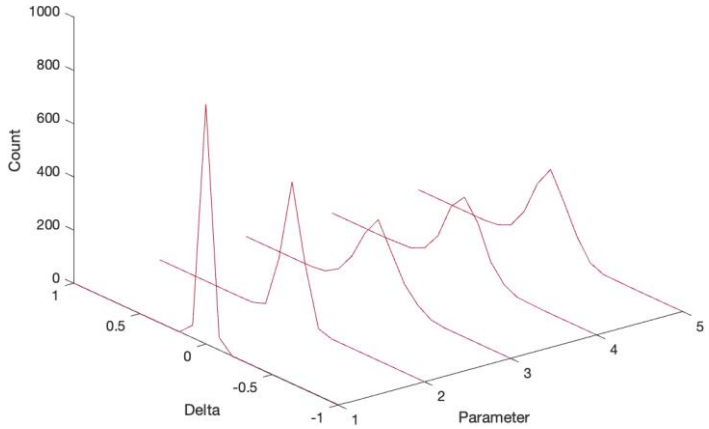

Figure 3.15. Gaussian Uncertainty Assumption in Parameters

With the mass and bending stiffness varied, the Monte Carlo simulation ran 1000 iterations to test how the design would react to uncertainty in these variables with respect to wingtip deflection (Fig. 3.16 and 3.17). Recall from Section 3.2.1, the expected deflection is 26.300 millimeters or 1.035 inches. The distribution of iterations in Fig. 3.16 shows a mostly Gaussian distribution, perhaps slightly right skewed, between deflection values ranging from 0.8 inches to 1.7 inches. Most of the iterations had a deflection between 1 and 1.2 inches (Fig. 3.16). The expected deflection falls within this range, although at the lower end. This suggests that the design may be sensitive to over deflecting with variations to the mass and bending stiffness. Additionally, from Fig. 3.17, uncertainty in mass and bending stiffness has an increasing effect on deflection with proximity to the wing tip. In other words, varying these variables has little effect on deflection near the root (lines are overlapping), but can have a larger effect when propagated to the wing tip (lines further apart).

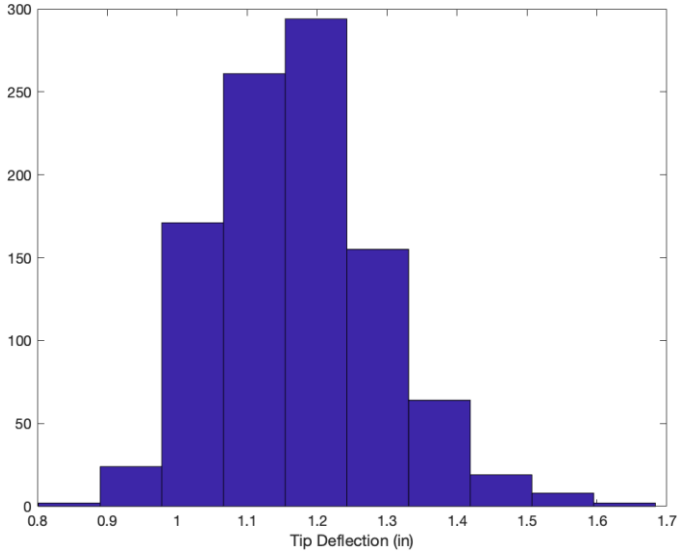

Figure 3.16. Monte Carlo Simulation Tip Deflection Histogram

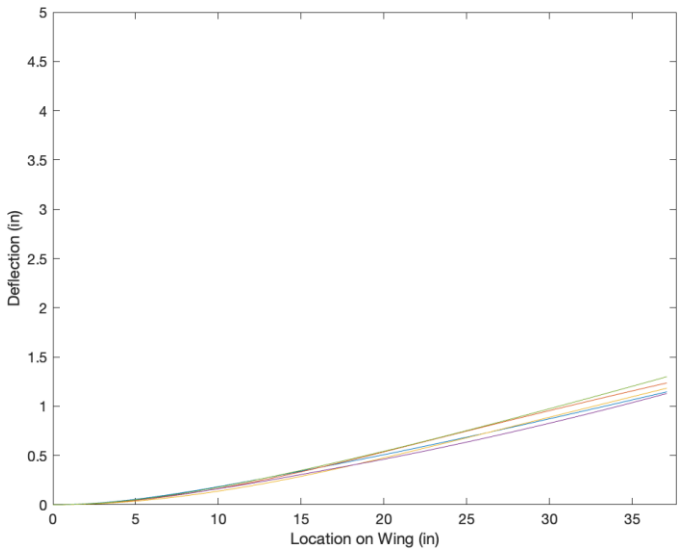

Figure 3.17. Monte Carlo Simulation Tip Deflection vs. Spanwise Location

3.3 Aircraft Analysis

This section covers how the mission-improved wing design was integrated with the existing plane components to form a complete aircraft. It details aspects of the system as a whole in respect to creating a working product.

3.3.1 Center of Gravity and Inertial Characteristics

The total weight of the aircraft with the optimally designed wings was 3252.88 grams. Design of the new wing was to be done in such a way that the center of gravity (CG) of the aircraft remained in the same relative location so as not to drastically change flight characteristics. The safe operating point for the center of gravity to be located is aligned with the quarter chord of the wing. With the new wings attached, the center of gravity is located at a vertical height of 23.61 millimeters below the center of the aircraft nose (Fig. 3.18). The center of gravity is located 407.68 millimeters aft of the nose of the aircraft, aligned with the quarter chord of the wing and centered within the fuselage (Fig. 3.19).

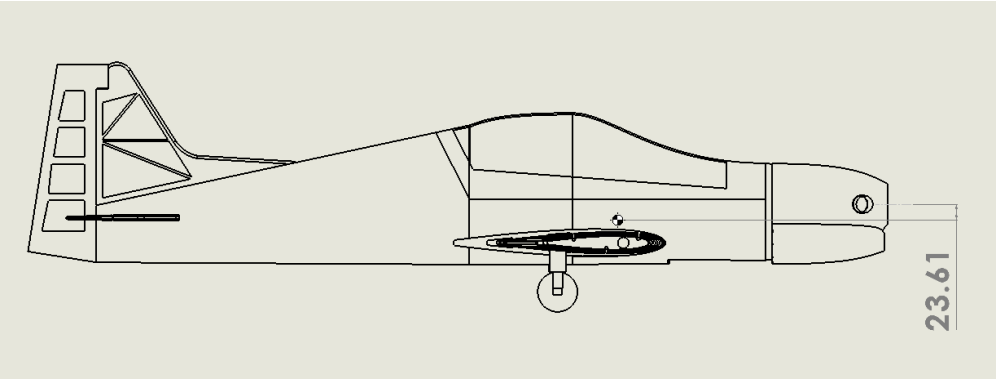

Figure 3.18. Side View with CG location

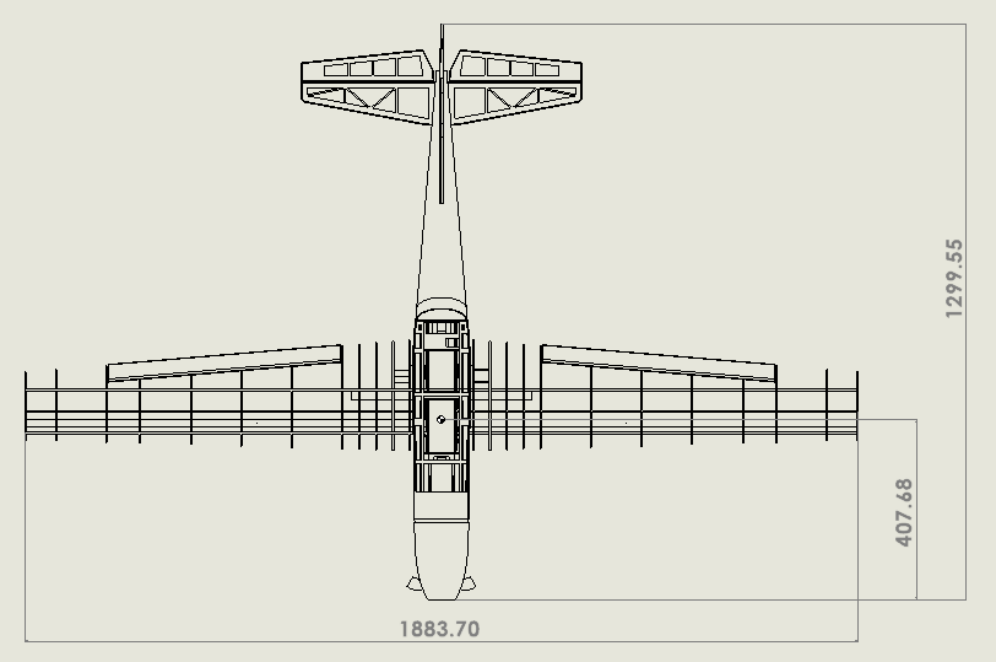

Figure 3.19. Top View Drawing with Major Dimensions [mm]

Another important characteristic of the aircraft is the moments of inertia. These values are important in describing how mass is distributed throughout the aircraft and how it will influence its stability during flight. The moments of inertia were calculated using SolidWorks and given to the aerodynamics specialist between different iterations of the design process. Let the x-axis be defined out of the nose of the plane, the y-axis out of the left wing, and the z-axis pointing up out of the top of the fuselage. Taken at the center of mass, the principal moments of inertia are listed in Table 3.8.

I_x [kg-m^2]	I_y [kg-m^2]	I_z [kg-m^2]
0.0989	0.2902	0.3716

Table 3.8. Principal Moments of Inertia Taken at Center of Mass

3.3.2 Loads and Deflections

Total wing loading at trim was calculated based on statics principals that the lift generated by the aircraft must be equal to the force of gravity on the aircraft. For simplicity, it was assumed that all lift was generated by the wings. This is an appropriate assumption due to the relatively small size of the horizontal tail in comparison to the wings. For SolidWorks simulation, the loading procedure detailed in Section 3.1.2 was followed to simplify the force for a single wing to the centroid of its lift distribution. The load was applied from the bottom of the wing and the deflection results were recorded (Fig. 3.20). Note that meshing for finite element analysis of the entire aircraft was not possible due to computing limitation. Instead, the central spar was added to the model to simulate the fuselage connection. The deflection of the wing, under 3 times the trim loading conditions, was found to be 26.30 millimeters.

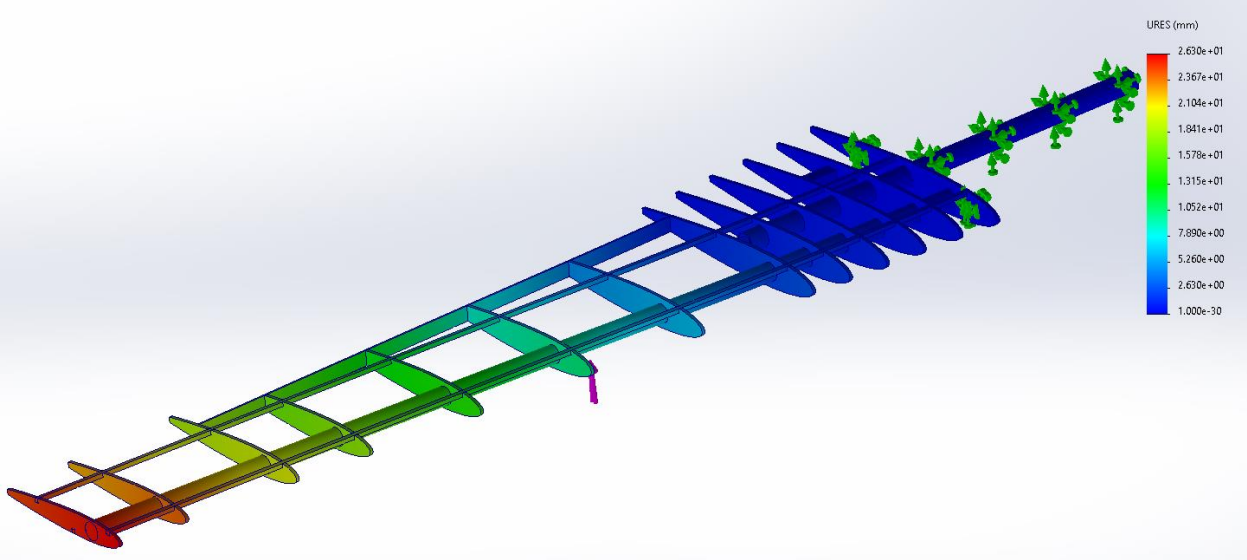

Figure 3.20. Deflection Test Results for Final Wing Design

3.3.3 Structural Dynamics

A dynamic analysis of the wing was performed to identify the resonant frequencies and node shapes associated with the geometry and mass of the design. This is a primary concern for aircraft because resonant frequencies can cause large oscillating displacements which could potentially lead to deformations, changes in flight characteristics, or catastrophic failure. A SolidWorks frequency analysis was performed for the final design and the first 4 resonant frequencies were recorded in Table 3.9. The accompanying node shapes for each frequency are shown in Fig. 3.21 through 3.24.

Mode No.	Frequency [Rad/sec]	Frequency [Hertz]	Period [sec]
1	120.56	19.188	0.052115
2	281.35	44.778	0.022333
3	624.57	99.403	0.01006
4	1065.4	169.57	0.0058974

Table 3.9. Resonant Frequencies

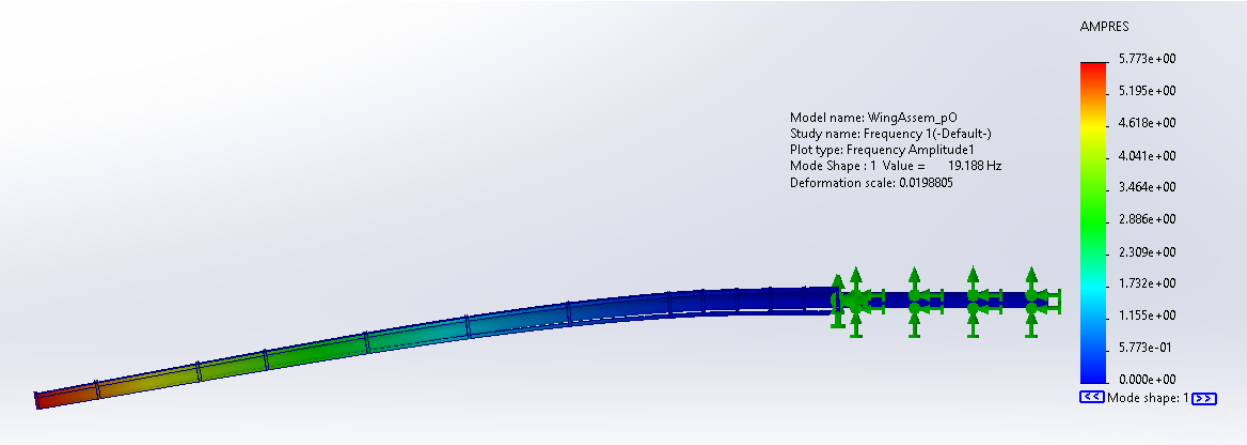

Figure 3.21. Mode Shape 1

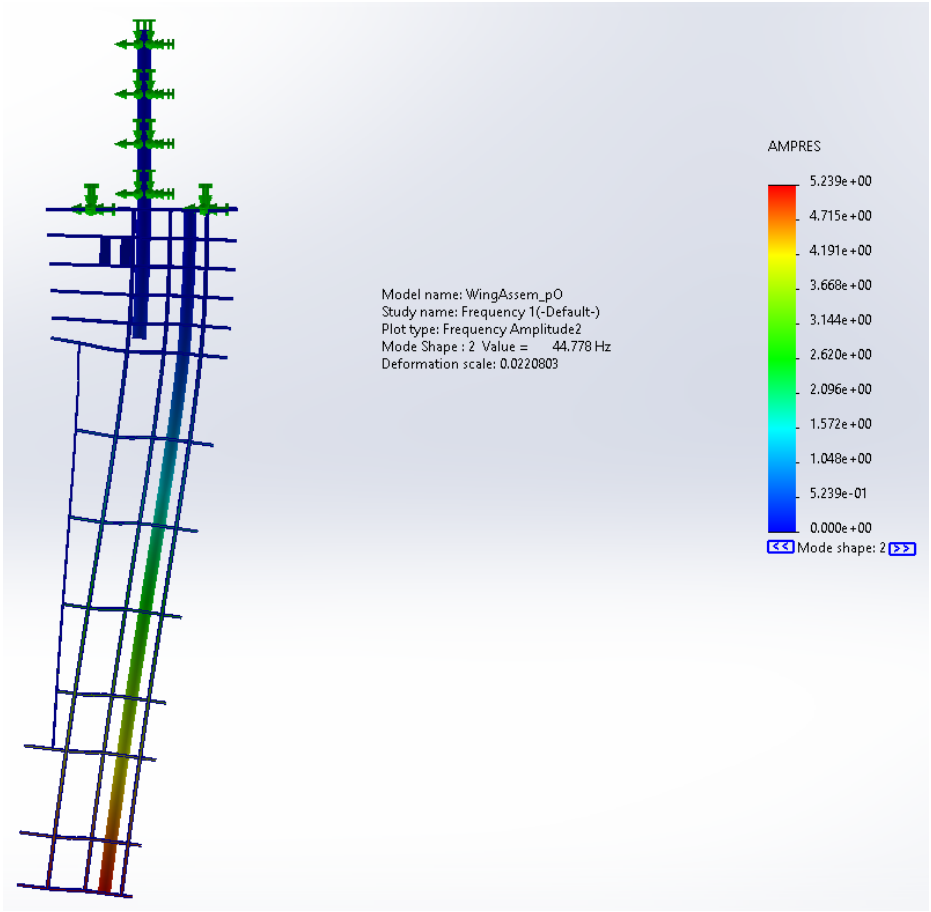

Figure 3.22. Mode Shape 2

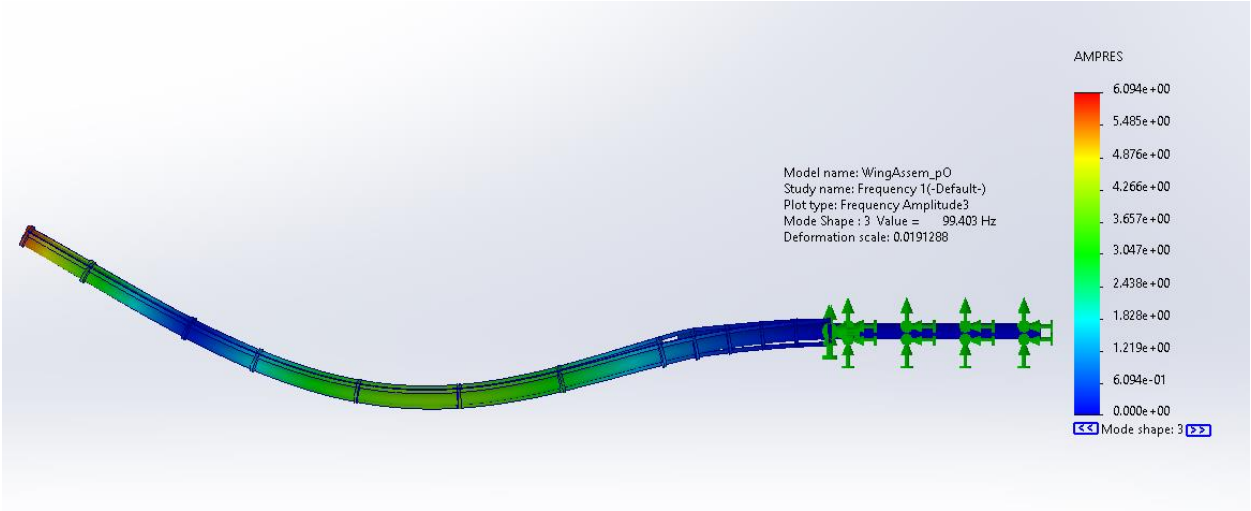

Figure 3.23. Mode Shape 3

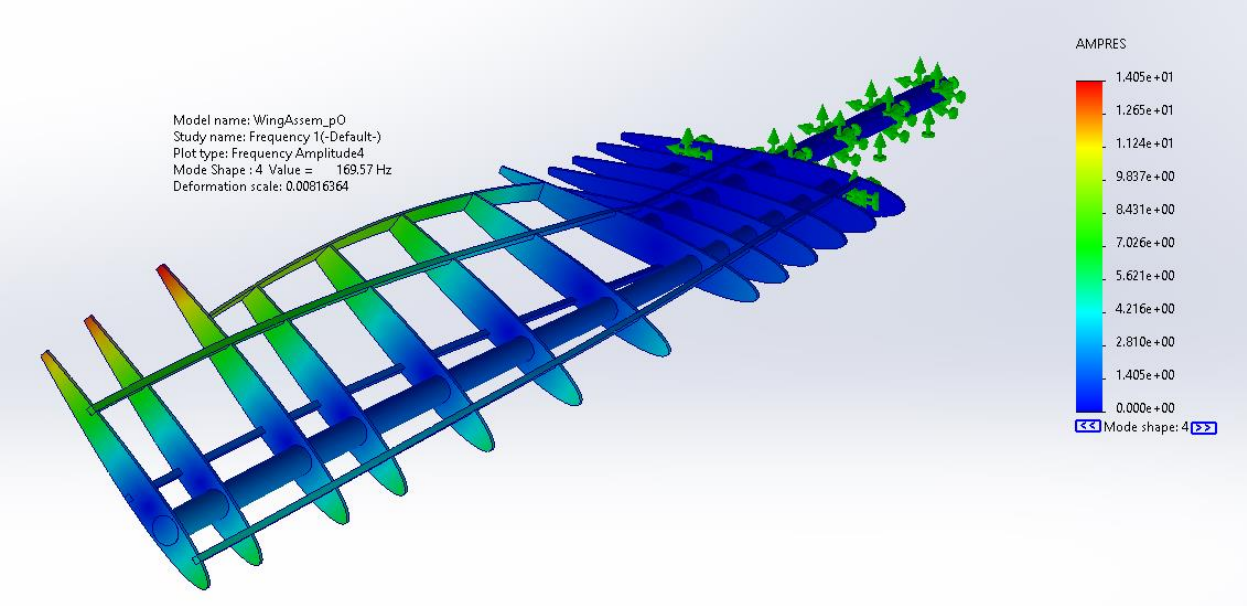

Figure 3.24. Mode Shape 4

The resulting frequencies detailed in Table 3.9 represent forcing frequencies that should be avoided as much as possible during operation of the aircraft. The most likely to occur is mode shape 1 because it has the lowest natural frequency (Fig. 3.21). However, this frequency is still relatively high, and it is unlikely that the aircraft would achieve an oscillating force to match this frequency and cause resonance during normal flight conditions.

3.3.4 Avionics

The final aspect to detail in relation to integrating the new wing design with the aircraft was providing hard points for mounting servos to control the aileron, the landing gear, and connection points for the wing to the fuselage. The design features a rib aligned near the center of the aileron with which a servo can be mounted for control (Fig. 3.25).

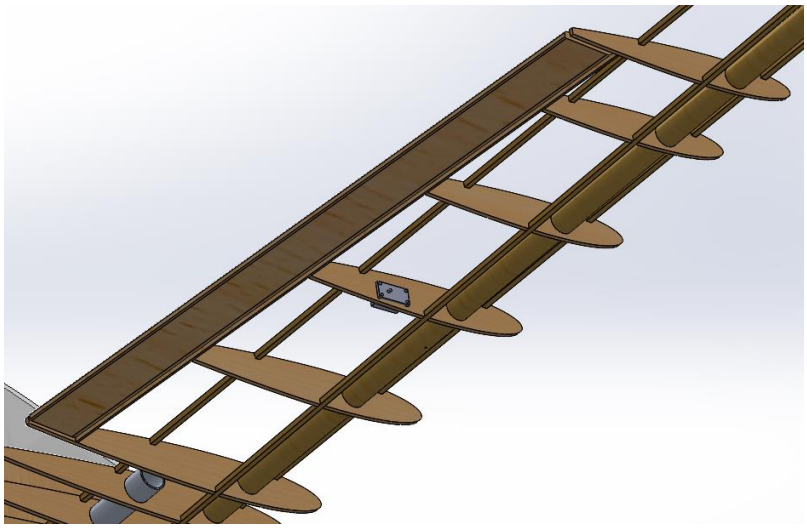

Figure 3.25. Servo Mounting Hard Point

The stock aircraft had a retractable landing gear mounted to the wing, so it was necessary to factor this into the design of optimized wings. It was determined that retraction of the landing gear during flight was unnecessary for the company mission and only added unnecessary complexity. The additional unnecessary footprint of the servo-controlled landing gear proved to be a design challenge because there were additional components that needed clearance between the mounting plate. To solve this, two yellow poplar beams were fixed between ribs with which the landing gear could be mounted, and the additional material could pass through for clearance (Fig. 3.26).

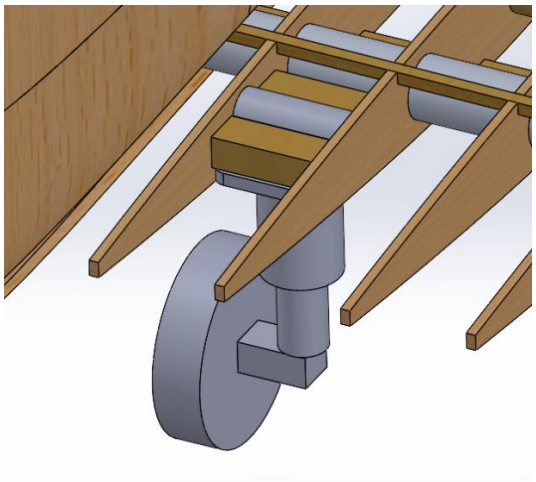

Figure 3.26. Landing Gear Mounting Hard Point

Finally, the connection to the fuselage required that the designed wing have a root-rib profile that was compatible with that of the stock wing. The hole pattern was carefully designed and located such that the wing fit seamlessly to the required hardware from the stock configuration with minimal gaps on the leading-edge side to minimize unnecessary drag (Fig. 3.27). The culmination of these design choices are shown in Fig. 3.28.

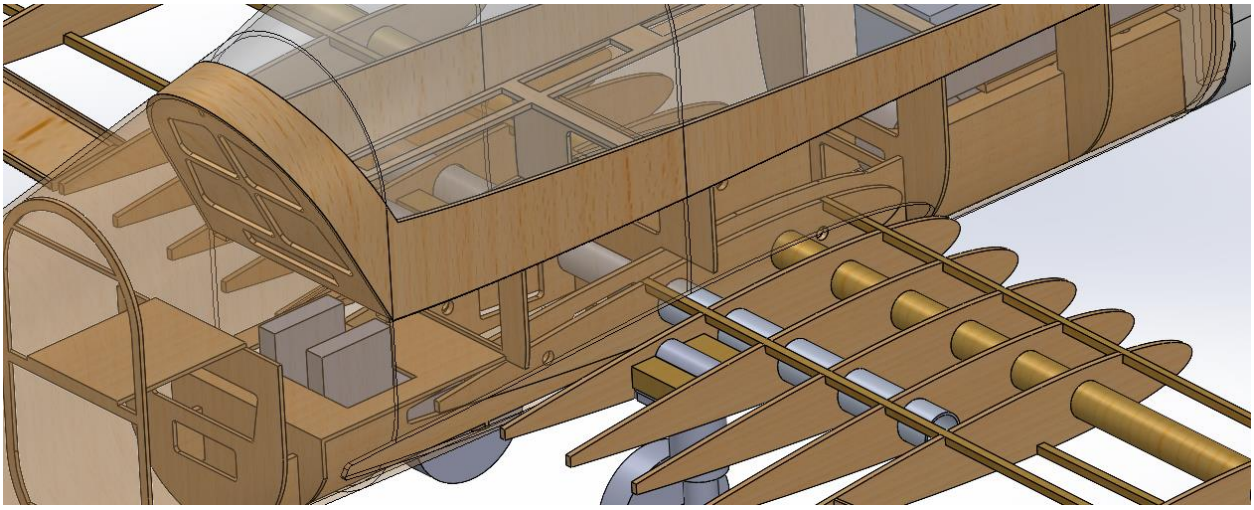

Figure 3.27. Wing Connection to Fuselage

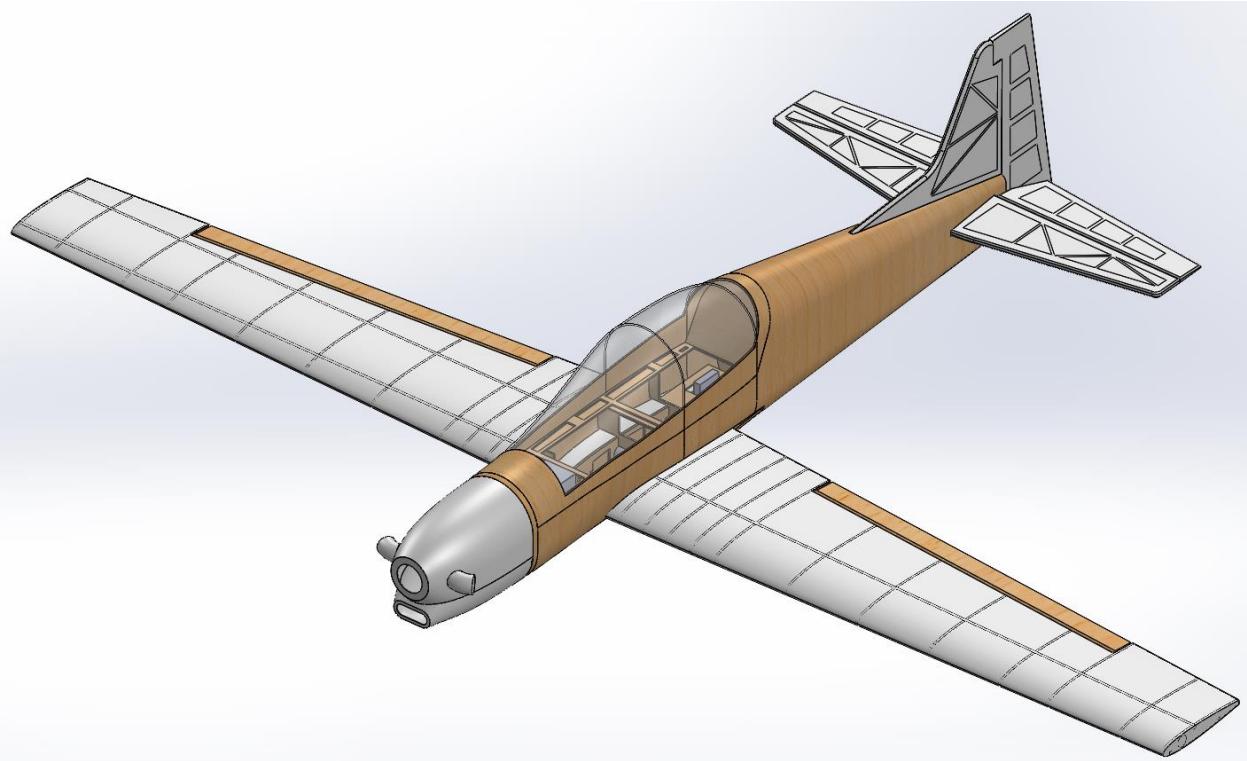

Figure 3.28. Full Plane Cad Model with Monokote Skin

4. Avionics

4.1. Mission Profile

The mission profile for Sweet Silence's delivery aircraft is presented below. Based on an early prototype of the aircraft, the plane is expected to have a range of approximately 13 km and an endurance of about 8 minutes. However, challenges have prevented this estimate from being updated with flight data for the updated wing design. It was assumed that the range and endurance will be comparable, though. Maintaining 30% of the aircraft's possible range as a safety factor yields an operational radius of 5 km about the hangar. Ongoing developments and future iterations of the aircraft aim to increase this radius to allow each plane to service a larger area.

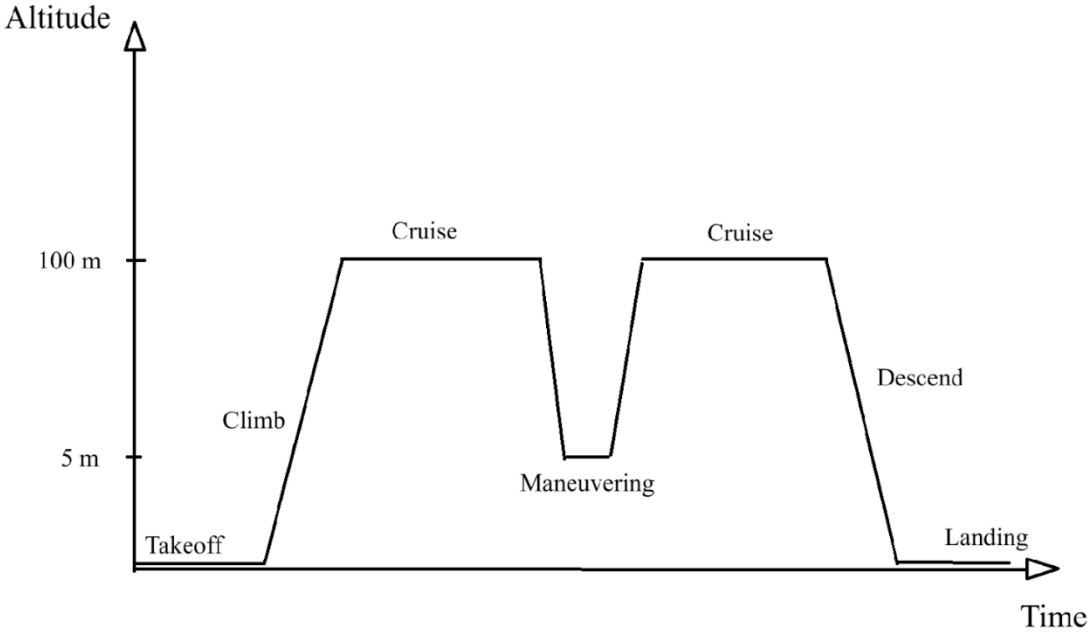

Figure 4.1. Flight profile for pacifier delivery

The mission plan and flight profile for pacifier delivery flights are presented in Figure 4.1. Overall, the airplane will fly directly from liftoff to the target, perform the delivery, and then return along the same path in reverse back to the hangar after. This plot summarizes the different phases of flight with respect to altitude and time. Due to the short takeoff distance required for this aircraft, the autopilot can take off directly from the storage site, with a small storage container and a 50 ft space for runway and initial climb out. The Climb phase is characterized by a 5.2 m/s rate of ascent to a cruise altitude of 100 m. The climb out will happen within the land area of the hangar initially, and the aircraft will then fly above streets in order to avoid potential collisions with buildings. Both cruise phases also take place avoiding streets and trees, taking place at 29 m/s to travel to and from the delivery site. The Descend phase has a 3.3 m/s rate of descent up until landing. The most complicated phase of the flight is the Maneuvering phase.

Maneuvering in Figure 4.1 consists of the approach to the drop site, where the plane descends from 100m to 5 m in altitude when it reaches the delivery site. The plane then decelerates to an airspeed of 14 m/s, moderately above stall speed, locates the delivery target, and actuates the payload mechanism to deploy the pacifier. Calling a pacifier delivery will happen through a phone

app, so the phone's GPS will be used to locate the customer and deliver the pacifier within 10 m of their location. The plane may need to turn or circle moderately to avoid trees or otherwise move to find and approach the known location of the customer's phone, but the intended mission behavior involves a low-speed and low-altitude straight line approach to deliver the pacifier, followed by another climb back up to cruising altitude.

4.2. Flight Test Cards

The flight test cards prepared for testing the final plane, involving flight performance characteristics and payload deployment testing, are all grouped together and presented in Figure 4.2.

Flight Test Cards

Jordan Hayden, Jack Britton

Test Flight 1

Card # 001	**Test Flight 1**	Date: 01 April 2025	AVIONICS SPECIALIST USE ONLY
	TAKEOFF		
A	30 sec. Stabilized Run		Time: _____
B	Choose any throttle setting for Roll-out (Ideally High)		Time: _____
C	Wheels up		Distance: _____
	REQUIRED REPEATS/NOTES		
	* Note takeoff starting position and wheels up		

Card # 002	**Test Flight 1**	Date: 01 April 2025	AVIONICS SPECIALIST USE ONLY
	CLIMB		
A	Choose any constant throttle setting (Ideally Medium-High)		Time: _____
B	Climb to cruise altitude		Time: _____
	REQUIRED REPEATS/NOTES		
	*Time right above wheels up is start of climb. Record time at end of throttle.		

CHECKOUT (Let Pilot get comfortable with aircraft)

Card # 003	**Test Flight 1**	Date: 01 April 2025	AVIONICS SPECIALIST USE ONLY
	ELEVATOR SINE SWEEP		
A	Maintain straight and level at any constant throttle setting.		Time: _____
B	Perform a medium magnitude sine sweep back and forth gradually Increasing Oscillations from 3, 2.5, 2, 1.5, 1, 0.5, 0.25 seconds. Repeat twice.		Time: _____ Time: _____ Time: _____
	REQUIRED REPEATS/NOTES		
	*Record start and stop time for each change in magnitude		

Card # 004	**Test Flight 1**	Date: 01 April 2025	AVIONICS SPECIALIST USE ONLY
	ELEVATOR 3-2-1-1		
A	Maintain straight and level at any constant throttle setting.		
B	Perform a Medium magnitude 3-2-1-1. Repeat twice.		Time: _____ Time: _____ Time: _____
	REQUIRED REPEATS/NOTES		
	* Record start and stop time for each change in magnitude		

Card # 005	**Test Flight 1**	Date: 01 April 2025	AVIONICS SPECIALIST USE ONLY
	RUDDER SINE SWEEP		
A	Maintain straight and level at any constant throttle setting.		
B	Perform a MEDIUM magnitude sine sweep back and forth gradually Increasing Oscillations from 3, 2.5, 2, 1.5, 1, 0.5, 0.25 seconds. Repeat twice.		Time: _____ Time: _____

		Time: _____
REQUIRED REPEATS/NOTES *Record start and stop time for each change in magnitude		

Card # 006	**Test Flight 1**	Date: 01 April 2025	AVIONICS SPECIALIST USE ONLY
RUDDER 3-2-1-1			
A	Maintain straight and level at any constant throttle setting.		
B	Perform a MEDIUM magnitude 3-2-1-1. Repeat twice.		Time: _____ Time: _____ Time: _____
REQUIRED REPEATS/NOTES * Record start and stop time for each change in magnitude			

Card # 007	**Test Flight 1**	Date: 01 April 2025	AVIONICS SPECIALIST USE ONLY
AILERON SINE SWEEP			
A	Maintain straight and level at any constant throttle setting.		
B	Perform a MEDIUM magnitude sine sweep back and forth gradually Increasing Oscillations from 3, 2.5, 2, 1.5, 1, 0.5, 0.25 seconds. Repeat twice.		Time: _____ Time: _____ Time: _____
REQUIRED REPEATS/NOTES *Record start and stop time for each change in magnitude			

Card # 008	**Test Flight 1**	Date: 01 April 2025	AVIONICS SPECIALIST USE ONLY
AILERON 3-2-1-1			
A	Maintain straight and level at any constant throttle setting.		
B	Perform a MEDIUM magnitude 3-2-1-1. Repeat twice.		Time: _____ Time: _____ Time: _____
REQUIRED REPEATS/NOTES * Record start and stop time for each change in magnitude			

Card # 009	Test Flight 1	Date: 01 April 2025	AVIONICS SPECIALIST USE ONLY
Additional Useful Maneuvers			
A	Elevator Singlet. Repeat twice. -useful to get spiral mode from it		Time: _____ Time: _____ Time: _____
B	Aileron Singlet. Repeat twice.		Time: _____ Time: _____ Time: _____
C	Rudder Singlet. Repeat twice.		Time: _____ Time: _____ Time: _____
D	Elevator Doublet. Repeat twice.		Time: _____ Time: _____ Time: _____

E	Aileron Doublet. Repeat twice.	Time: _____ Time: _____ Time: _____
F	Rudder Doublet. Repeat twice.	Time: _____ Time: _____ Time: _____
G	Phugoid. Repeat twice.	Time: _____ Time: _____ Time: _____
H	Spiral. Repeat twice.	Time: _____ Time: _____ Time: _____
I	Circle. Repeat twice.	Time: _____ Time: _____ Time: _____
REQUIRED REPEATS/NOTES *Record Location of wheel down at touch down and when aircraft stops.		

Card # 010	Test Flight 1	Date: 01 April 2025	AVIONICS SPECIALIST USE ONLY
DESCENT			
A	Maintain and level flight at medium throttle.		
B	Choose any throttle setting to descend at a reasonable rate		Time: _____
REQUIRED REPEATS/NOTES *Record time immediately at the start of descent. Record time at touchdown.			

Card # 011	Test Flight 1	Date: 01 April 2025	AVIONICS SPECIALIST USE ONLY
LANDING			
A	Wheels down.		
B	Choose any throttle setting for Roll-in.		Time: _____
C	Full Stop		
REQUIRED REPEATS/NOTES *Record Location of wheel down at touch down and when aircraft stops.			

Test Flight 2

Card # 001	**Test Flight 2**	Date: 01 April 2025	AVIONICS SPECIALIST USE ONLY
	TAKEOFF		
A	30 sec. Stabilized Run		Time: _____
B	Choose any throttle setting for Roll-out (Ideally High)		Time: _____
C	Wheels up		Distance: _____
	REQUIRED REPEATS/NOTES		
	* Note takeoff starting position and wheels up		

Card # 002	**Test Flight 2**	Date: 01 April 2025	AVIONICS SPECIALIST USE ONLY
	CLIMB		
A	Choose any constant throttle setting (Ideally Medium-High)		Time: _____
B	Climb to cruise altitude		Time: _____
	REQUIRED REPEATS/NOTES		
	*Time right above wheels up is start of climb. Record time at end of throttle.		

CHECKOUT (Let Pilot get comfortable with aircraft)

Card # 003	**Test Flight 2**	Date: 01 April 2025	AVIONICS SPECIALIST USE ONLY
	En-route to Payload Drop Zone		
A	Maintain Straight and Level flight for a pass		Time: _____
B	Slightly Reduce Altitude at Drop Zone		Time: _____
	REQUIRED REPEATS/NOTES		
	*Time right above wheels up is start of climb. Record time at end of throttle.		

Card # 004	**Test Flight 2**	Date: 01 April 2025	AVIONICS SPECIALIST USE ONLY
	Payload Deployment		
A	Activate payload motors		Time: _____
B	Cruise in bank turns of 15-20 degs to approach target.		Time: _____
C	Execute Payload deployment		Time: _____
D	Increase Altitude slightly		Time: _____
E	Conduct a wide gentle bank turn at low throttle setting and re-align with target		Time: _____
F	Execute Payload Deployment		Time: _____
G	Exit Drop Zone		
	REQUIRED REPEATS/NOTES		
	*Time right above wheels up is start of climb. Record time at end of throttle.		

Card # 005	Test Flight 2	Date: 01 April 2025	AVIONICS SPECIALIST USE ONLY
	DESCENT		
A	Maintain and level flight at medium throttle.		
B	Choose any throttle setting to descend at a reasonable rate		Time: _____
	REQUIRED REPEATS/NOTES		
	*Record time immediately at the start of descent. Record time at touchdown.		

Card # 006	Test Flight 2	Date: 01 April 2025	AVIONICS SPECIALIST USE ONLY
	LANDING		
A	Wheels down.		
B	Choose any throttle setting for Roll-in.		Time: _____
C	Full Stop		
	REQUIRED REPEATS/NOTES		
	*Record Location of wheel down at touch down and when aircraft stops.		

Figure 4.2. Flight Test Cards

4.3. Payload Design

4.3.1. Design Requirements

The design goal for the payload system was to modify the mechanism from a pre-existing blaster to mount onto the plane and be remotely operated. The pre-existing design used two flywheels within a NERF blaster to impart rotational energy into kinetic energy for the foam balls (representing pacifiers for the company mission). The NERF blaster used 6 C batteries (totaling 9 volts) to power the flywheel and required the user to trigger a mechanism to push the ball into the flywheels.

To prepare this mechanism for mounting onto the plane required significant reduction in volume and weight for practical packaging on the plane, as well as reducing inefficiency resulting from an excessively heavy payload. The design must also be able to be actuated remotely from the pilot or flight computer.

4.3.2. Design Approach

The initial efforts in designing the payload system were directed towards significant debulking of the mechanism. The 6 C batteries were replaced with a single 9V battery, providing equivalent voltage but significantly reduced weight, at the downside of reduced capacity. Also, all the plastic components not strictly necessary for storing the foam balls or accelerating them were removed. This leaves the flywheel and magazine, pictured in Figure 4.3, the basic components critical for the payload's functionality. They needed to be packaged and configured to provide intended functionality while in flight.

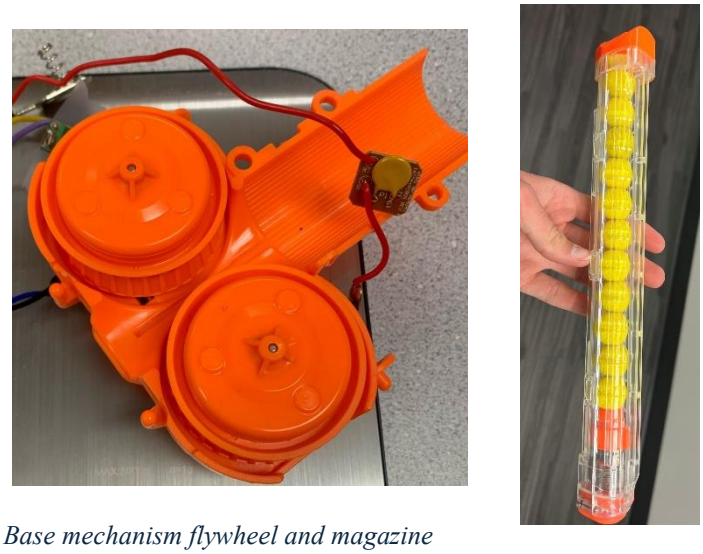

Figure 4.3. Base mechanism flywheel and magazine

4.3.3. Final Design

The final design secures the magazine horizontal to the plane and points the flywheels at a 45 degree angle downwards to allow the plane to fire at a downward angle while maintaining level trim, simultaneously avoiding hitting the landing gear with the projectiles. The use of the mechanism involves activating the motor to spin up the flywheels, then feeding each foam ball one at a time into the flywheels to fire them out of the aircraft. It has a mass of approximately 500g fully loaded.

This was accomplished by mounting both of these components onto a 3D printed base, designed in SolidWorks and presented in Figure 4.4. This mount features dimensional tolerancing to account for errors in 3D printing accuracy, maintaining the proper relative positions of the components. The full assembly is given in Figure 4.5, with magazine and flywheels attached. The magazine is removable, secured to the plane with Velcro, and the flywheel is bolted to the base, which is connected to the plane via double sided tape and superglue.

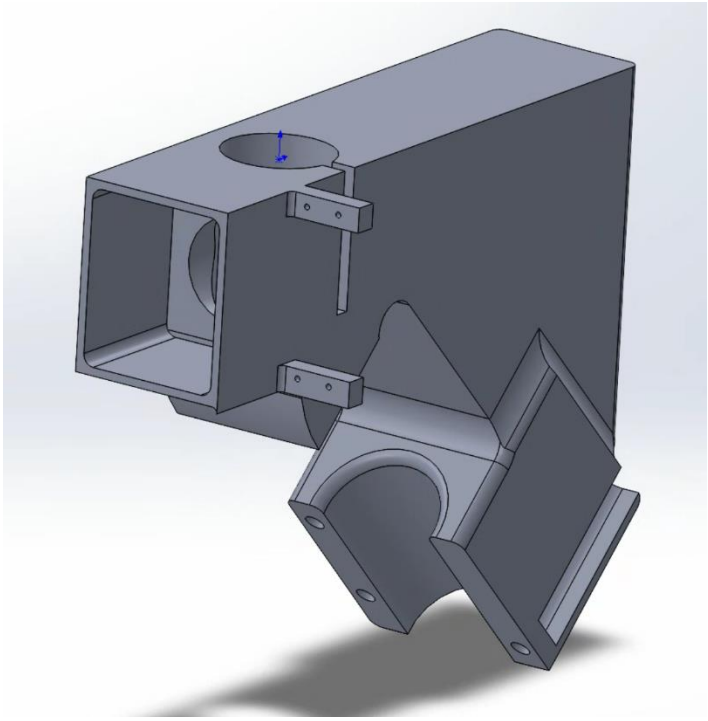

Figure 4.4. CAD model of payload mount

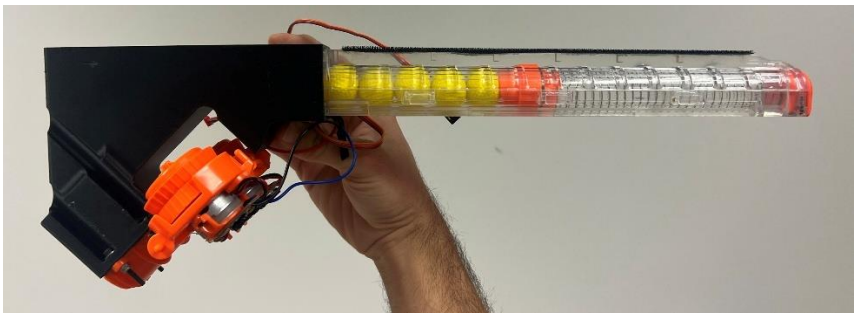

Figure 4.5. Payload with flywheel and magazine attached

The mechanism has a channel to feed the balls into the flywheel with gravitational assist. The next ball to be delivered is held in place using the compression of the spring within the magazine. The friction this force creates within the channel is sufficient to hold the ball in place, even with substantial shaking representative of extreme flight maneuvers. To deploy, a servo presses the ball out of this compression and allows it to drop into the flywheel firing mechanism. This servo and the channel where the ball is contained are displayed in Figure 4.6. This is representative of the state the base is in when the magazine is loaded and waiting for the flywheel to be turned on and the servo to be actuated.

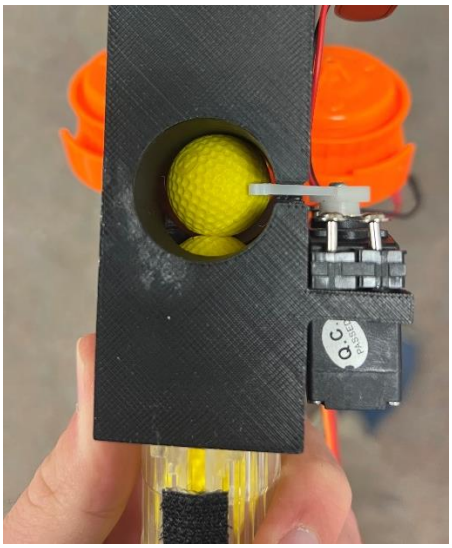

Figure 4.6. Loaded payload base with ball and servo

4.3.4. Future considerations

Preliminary testing of the payload was extremely promising, with the payload successfully firing via signals from a servo tester. Additionally, the mechanism was robust and held the next ball to be fired in place very reliably. However, sometimes it would take rotating the servo back and forth several times before the ball was deployed, so one future place for improvement would be extending the servo arm to ensure that a ball is deployed with each actuation of the servo. Another thing that could be improved is reducing the bulk of the base, reducing the weight of the plastic and potentially changing the angle of the flywheels to reduce the necessary packaging volume.

Due to rapid unscheduled disassembly of the prototype aircraft, in flight payload testing was not conducted. Thus, further testing of the mechanism in flight is recommended. However, another few improvements which could be made to this design include more robust mounting between the base and the plane, as well as adjusting the circuitry associated with the mechanism such that the separate 9V battery is no longer required and the mechanism may be entirely powered by the other batteries powering the plane.

4.4. Control Surfaces

The aircraft has a typical control system, with a rudder, elevator, and ailerons. The custom wing outfitted for the plane had traditional tailing edge ailerons that were each 30 cm long and 3.8 cm wide. They were located at the wingtips, with a lateral position of ± 80 cm from the central axis for each aileron. The actuator used to control these ailerons was a HS-77BB low profile aileron servo manufactured by HiTEC. More information on this servo is available in Section 4.5, outlining the experimental measurement of the actuator.

4.5. Experimental Measurement of Actuator

Experimental measurement of the HS-77BB low profile aileron servo actuators used to control the ailerons was conducted by attaching a laser to the servo (positioned at the bottom vertex of the triangle in Figure 4.7) and using trigonometry relating the laser's position with the actuator's performance. The experimental layout is presented in Figure 4.7. The distance between the servo

and the wall is *a-wall*, and *a-1* and *a-2* are the distances between the center point on the wall and the points of the laser at the full servo rotation limit for each direction. The angles θ-1 and θ-2 are calculated by trig to give the full rotation range.

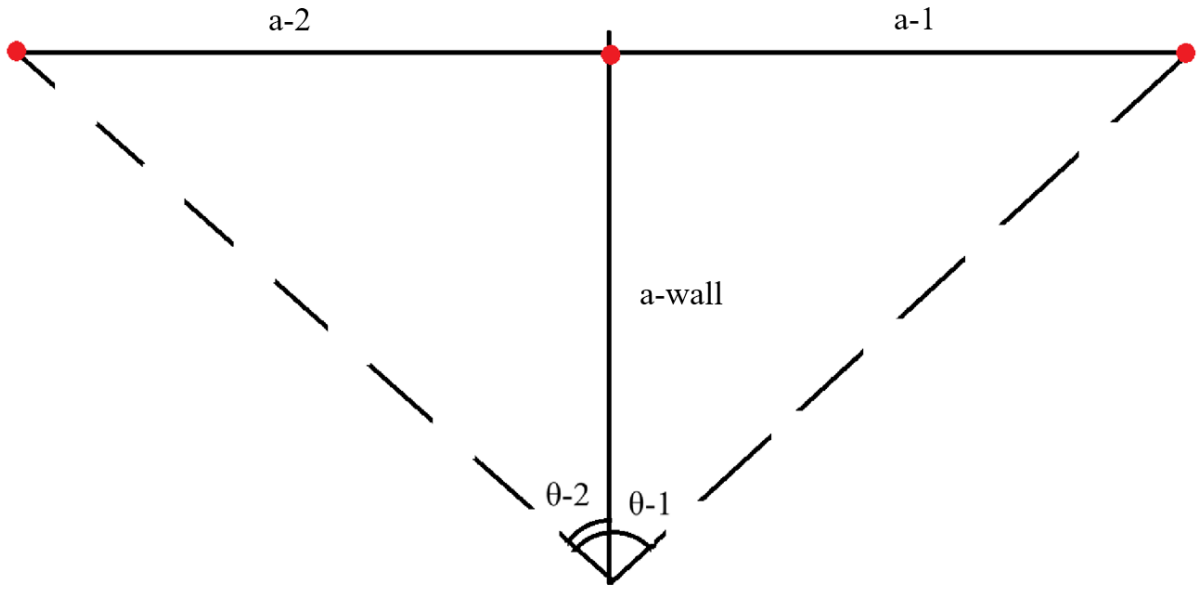

Figure 4.7. Actuator experimental configuration

The experiment measured these three lengths to determine the angular limits of the servo, and then the servo was put through a constant "sweep" so that it would continuously move between the leftmost limit and the rightmost limit as fast as possible. Timing these sweeps gave the servo's angular rate.

The distance *a-wall* was measured as 2.8 m, *a-1* was measured as 4.2 m, and *a-2* was measured as 3.3 m. Simple trigonometry yields *θ-1* as 56° and *θ-2* as 49°, giving a full angular range of 105°. During the sweep, 5 full "back and forth" sweeps were recorded to take 5.5 seconds, giving a total angular rate of 191 degrees per second. These performance parameters were implemented into the controls specialist's model to accurately reflect the plane's performance characteristics.

5. Controls

The controller for the aircraft used the dynamics of the PDR version due to time constraints. A PID (Proportional-Integral-Derivative) feedback controller was used to design architecture for the aircraft. Again, due to time constraints the controller was designed only using the P, and doing so the design process consisted of utilizing the root loci plots to select a gain, run the MALAB code and adjust the gain accordingly based on the closed loop responses.

5.1 Background

The controller consisted of two main sections Altitude Hold, and Yaw Damper.

5.1.1 Altitude Hold

The objectives of the controller were to maintain a low steady-state error, moderate time constant by limiting a rapid pitch that would cause stall, and to keep damping high for phugoid and short-period modes. The altitude hold architecture consisted of multi-loop architecture. The inner-loop (fig. 5.1) controlled the pitch angle and the outer-loop (fig. 5.2) controlled the altitude. The inner-loop utilizes two gains (Kt, for theta) and (Kq) to control pitch rate. The gain for the outer-loop (Kh) is used for the altitude control.

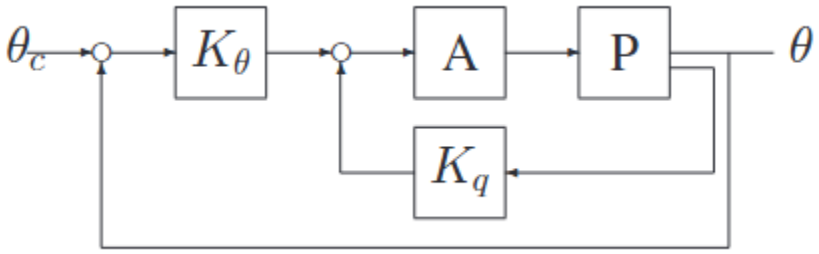

Figure 5.1 Altitude inner-loop

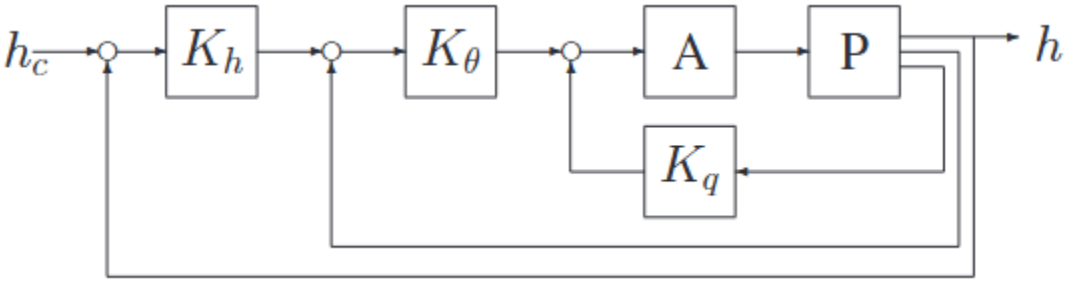

Figure 5.2 Altitude Outer-loop

5.1.2 Yaw Damper

The object was to maximize the damping in dutch-roll mode, and achieve fast tracking of roll-rate commands. The multi-loop architecture consisted of two parallel loops. The top loop (fig. 5.3) consisted of the actuator for the aileron, and the gain (Kp) used to achieve the pitch rate. The

bottom loop (fig. 5.3) consists of the actuator for the rudder, and the gain (Kr) that acts as a yaw damper and used to obtain the yaw rate.

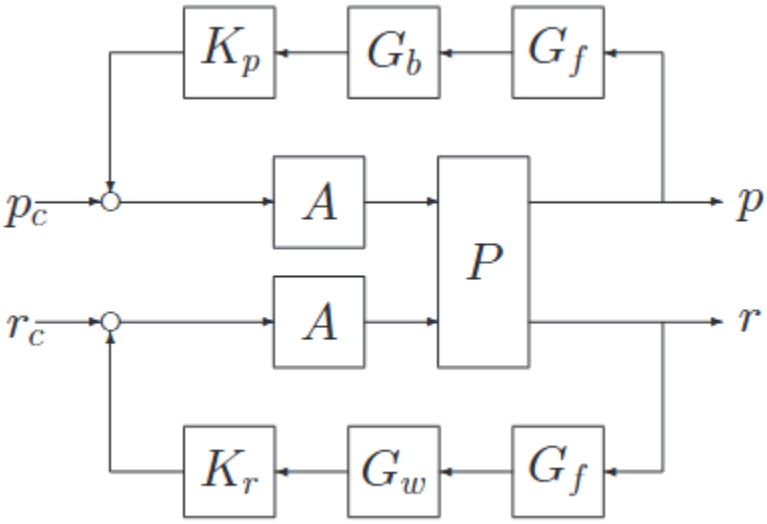

Figure 5.3 Yaw Damper Architecture

5.2 Controller Design Process

For each controller architecture the PID process was utilized of selecting a gain from the root-locus plot and then viewing the step responses. If the tracking was not adequate due to lack of damping, steady-state error, etc. The gain was adjusted accordingly.

5.2.1 Altitude Hold Controller Design

The inner-loop gains were selected first. The root locus for the two pitch rate gains, Kt and Kq were initially viewed when both gains were set to zero to understand how a change in gain affected each root loci. The Kq gain was selected first, due to the fact it is part of a feedback loop and in closed loop system the Kt gain is directly impacted by the Kq value.

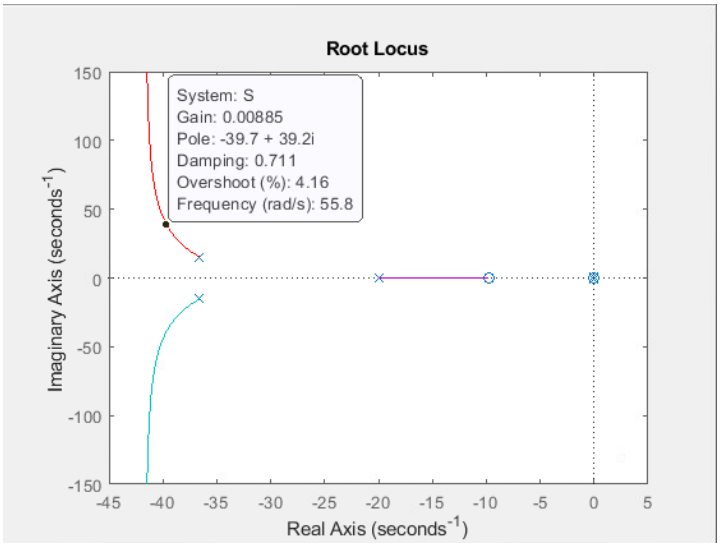

Figure 5.4 Kq Root Locus when Gain is Set to Zero

To start select a small gain to see how it affects the root locus, Kq = 0.00885 was plugged into the altitudehold.m file, figure 5.5 was the output. It was concluded that the larger gain causes faster response. Next a larger gain was selected (to obtain good tracking) but small enough that good short-period damping can exist too. Ideally the biggest gain that moves poles left and not too high is desired. Choose Kq = -0.113.

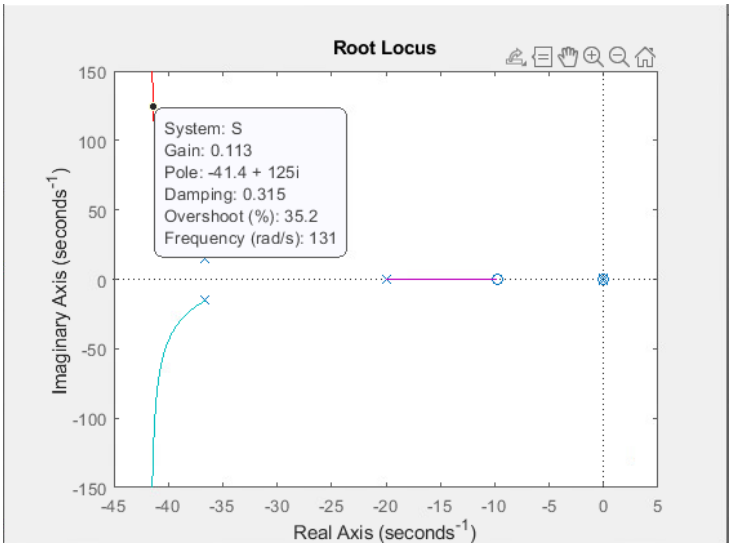

Figure 5.5 Kq Root Locus when Gain is Set to 0.00885

The result was pretty good raking. Due to reaching the desired result the Kq loop was closed and the Kt gain was selected. The block diagram and bode plot for this root locus are displayed in figures 5-6, and 5-7 respectively.

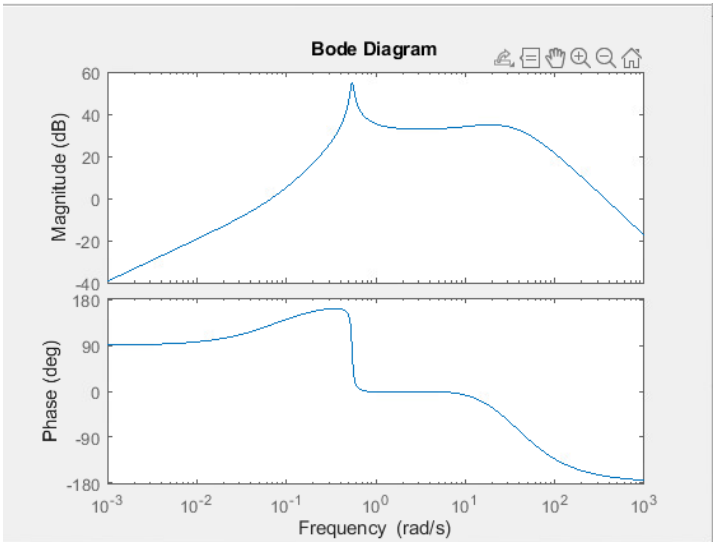

Figure 5.6 Bode Plot for Kq Root Locus

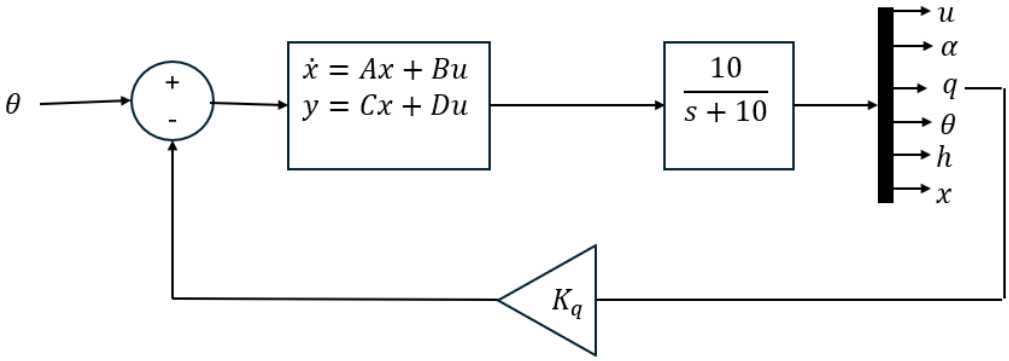

Figure 5.7 Block Diagram for Kq Root Locus

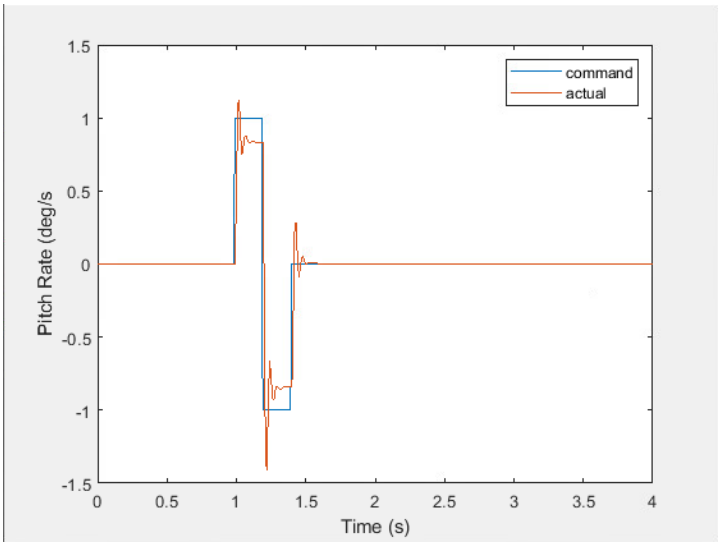

Figure 5.8 Pitch Rate Tracking for Kq

The pitch rate response associated with the selected Kq gain (Fig. 5–8) demonstrates overall good tracking performance. Although there is noticeable overshoot and a marginal steady-state error, this response is generally acceptable for a pitch rate loop. In particular, the steady-state error cannot be completely eliminated without significantly increasing the controller gain or introducing integral action. However, doing so would make the system more sensitive to high-frequency noise and may lead to oscillatory or unstable behavior.

Because pitch rate commands are typically short-duration transients rather than sustained inputs, eliminating the small steady-state error is not critical. Attempting to fully remove this error could result in an overly aggressive controller, causing excessive actuator activity and amplifying sensor noise. This would degrade the overall stability and robustness of the system. Therefore, the current level of tracking—despite the small error—is a balanced trade-off between responsiveness, noise sensitivity, and stability.

The pitch rate loop was finished by the Kt gain. Figure 5.9 shows the root locus for Kt when it was set to an initial value of zero. An initial gain was selected from the root locus to view how to root locus was affected by the gain.

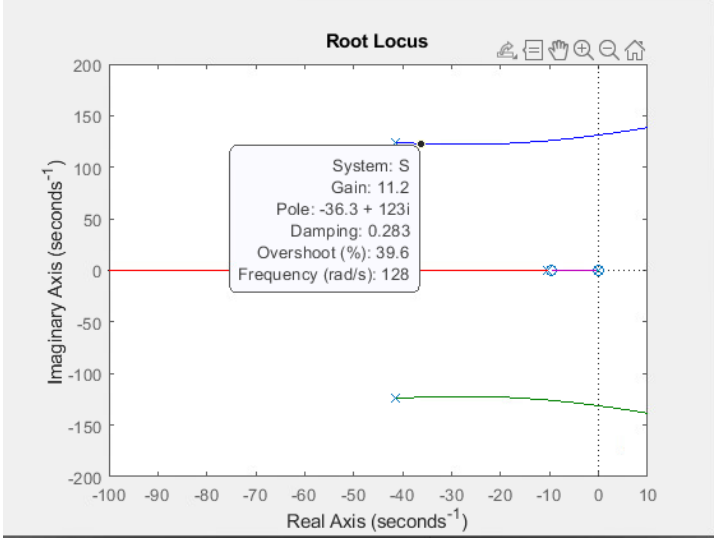

Figure 5.9 Kt Root Locus when Gain is Set to Zero

Two observations were made: 1) the poles go right (unstable) as gain is increased, 2) the poles are relatively flat as they move, which means the damping is steadily decreasing. Select a Choose large K for good damping and tracking: Kt = 11.2. Decent tracking, a larger gain was selected for even better tracking, and to diminish steady-state error.

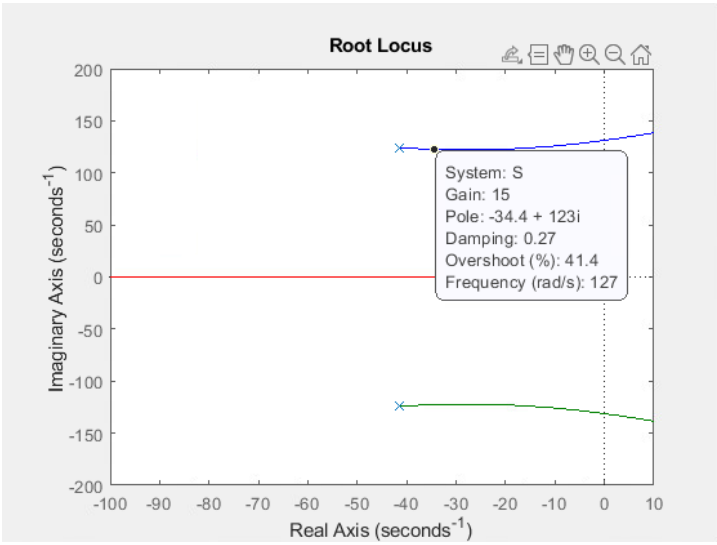

Figure 5.10 Kt Root Locus when Gain is Set to 11.2

When Kt was set to 15 the tracking was appropriately fast with good damping and little to no steady-state error and no overshoot. The bode plot (fig. 5.11) and block diagram (fig. 5.12) for the Kt root locus provide context for selected gain. The block diagram provides a visual representation while the bode plot displays the magnitude and phase.

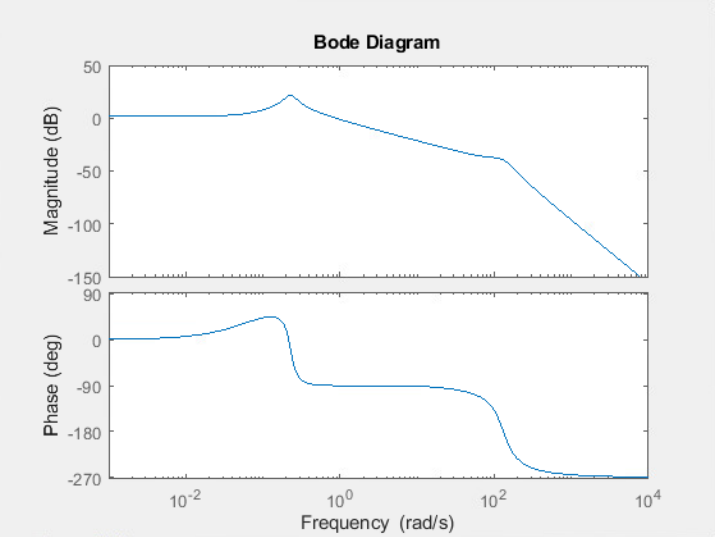

Figure 5.11 Bode Plot for Kt Root Locus

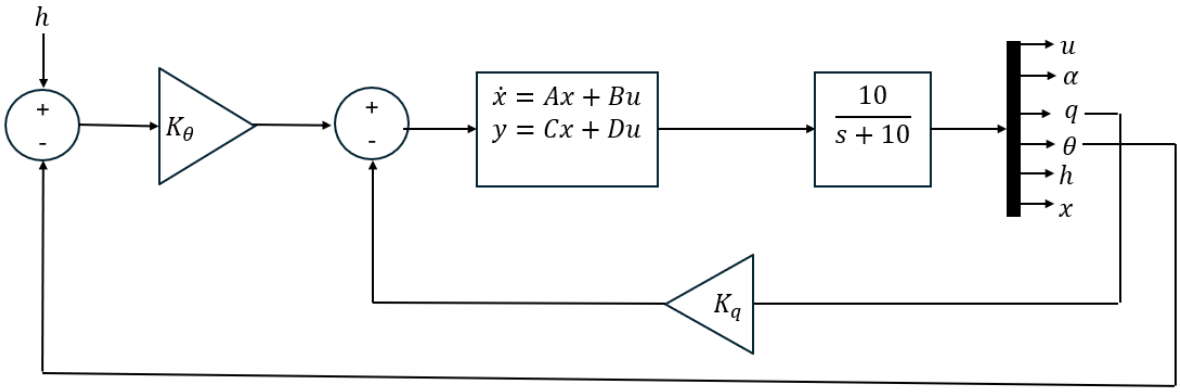

Figure 5.12 Block Diagram for Kt Root Locus

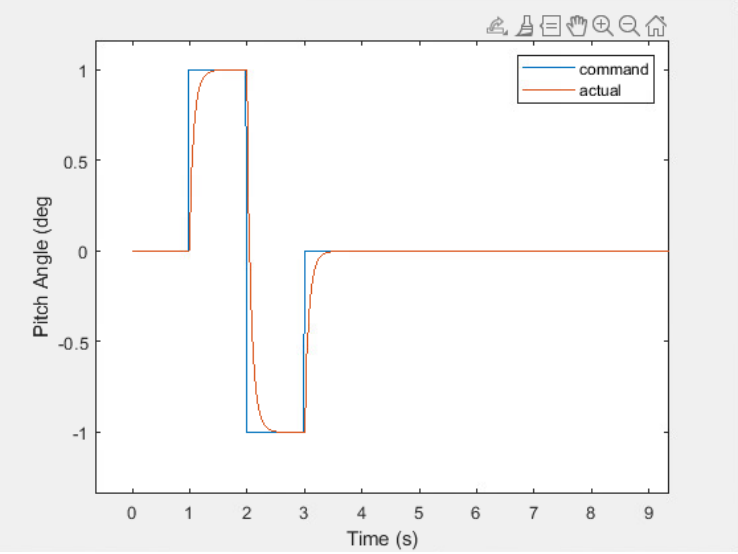

Figure 5.13 Pitch Angle Response to Doublet Command

Figure 5.13 demonstrated that the pitch angle tracking was of high quality, with no overshoot, no steady-state error, and good damping. This was important for the altitude hold controller, as accurate pitch angle response was crucial for maintaining the desired altitude. The well-behaved pitch dynamics ensured that the aircraft's vertical trajectory remained stable and consistent, contributing to overall system performance and control reliability.

The altitude controller, the outler-loop, is directly impacted by the Kh gain. To accurately select the Kh gain, the altitudehold.m file was run with a Kh set to a value of zero. This allowed the user to view and understand the root locus plot and how a selected gain would impact the desired output.

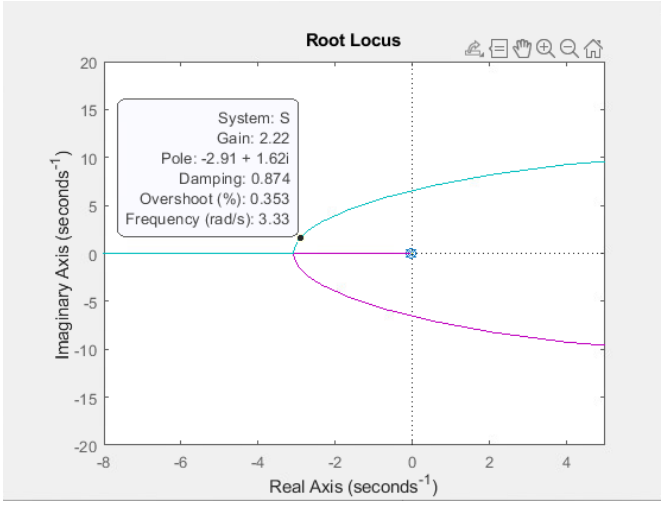

Figure 5.14 Kh Root Locus when Gain is Set to Zero

The following behaviors were observed for Kh root locus (fig. 5.14): 1) the phugoid poles are initially real (overdamped), 2) the phugoid poles become oscillator when gain is greater than approximately 2, 3) the phugoid poles become unstable when gain is greater than approximately 11. Select a gain the is large enough to get an oscillatory phugoid mode but not too big to remain stable. Kh = 2.22 was selected.

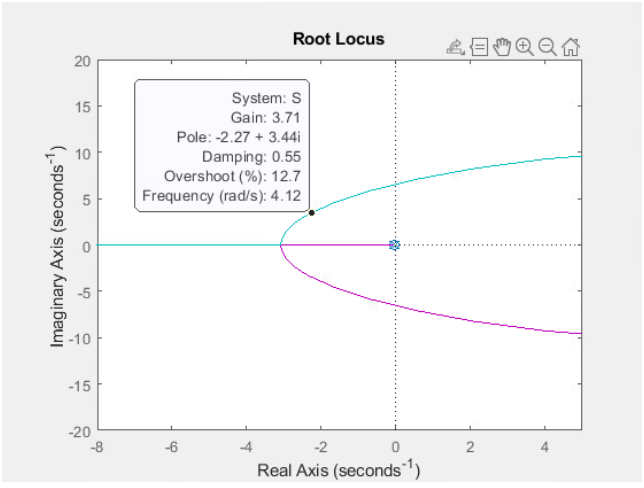

Figure 5.15 Kh Root Locus when Gain is Set to 2.22

When Kh = 3.7 the tracking for the altitude changes reasonably fast, and has a minor overshoot, and minor steady-state error, but quality decayed to the desired step input. The bode plot (fig. 5.16) and block diagram (fig. 5.17) for the Kh root locus provide context for selected gain. The block diagram provides a visual representation while the bode plot displays the magnitude and phase.

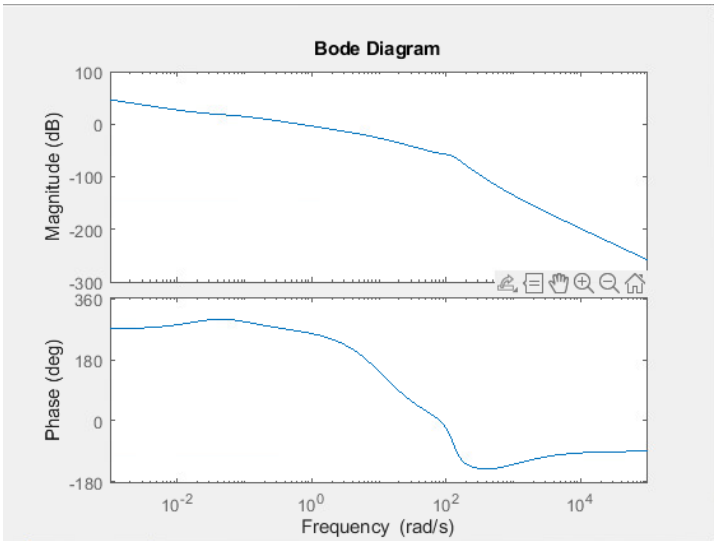

Figure 5.16 Bode Plot for Kh Root Locus

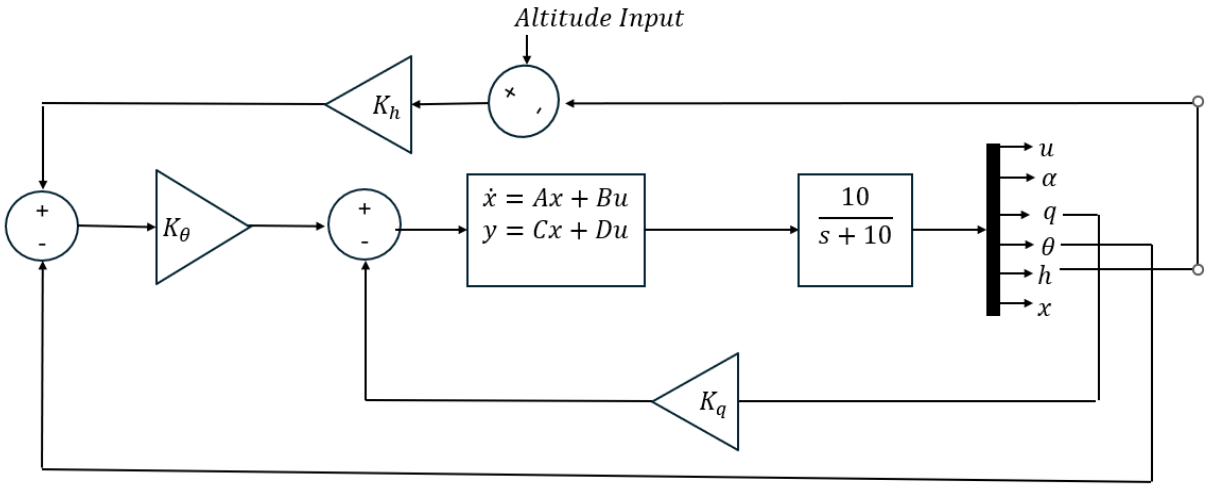

Figure 5.17 Block Diagram for Kh Root Locus

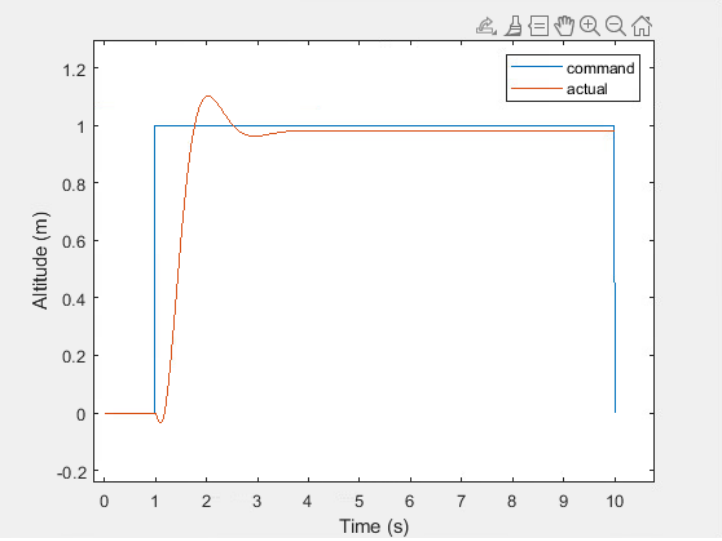

Figure 5.18 Altitude Step Response for Altitude Hold

Figure 5.18, the step response to the altitude command showed a system that tracked the desired altitude quickly, with a smooth rise toward the target value. There was a slight overshoot, indicating a moderate level of damping, but it remained within acceptable limits, demonstrating a well-balanced transient response. The system settled efficiently without excessive oscillations, and the final altitude closely matched the commanded input, reflecting a low steady-state error. This response indicated that the altitude controller was both responsive and stable. Such good tracking performance was important because it ensured the vehicle could accurately and promptly reach the commanded altitude, which is critical for maintaining safe flight, achieving mission objectives, and responding to dynamic environments. Table 5.1 displays the qualities and characteristics of the altitude step response (fig. 5.18).

Table 5.1 Characteristics of Altitude Step Response

Parameter	**Value**
Precent Overshoot	~10%
Rise Time	~2.1 seconds
Steady-State Error	~0.02 meters
Settling Time	~3.5 seconds

5.2.2 Yaw Damper Controller Design

The root locus of both the aileron and rudder were originally set to zero to understand the impact of gain on the root loci plots. Kp is the gain that tries to achieve tracking of pitch rate, Kr is the gain acting as yaw damper.

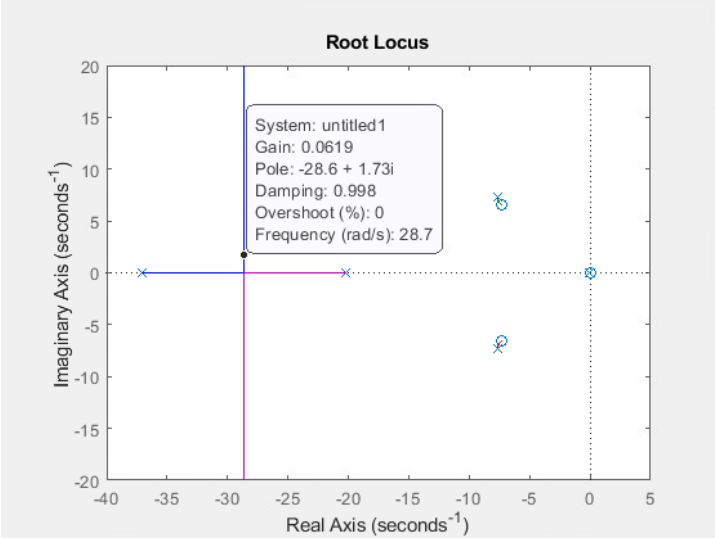

Figure 5.19 Root Locus for Roll Rate to Aileron when Kp =0.0

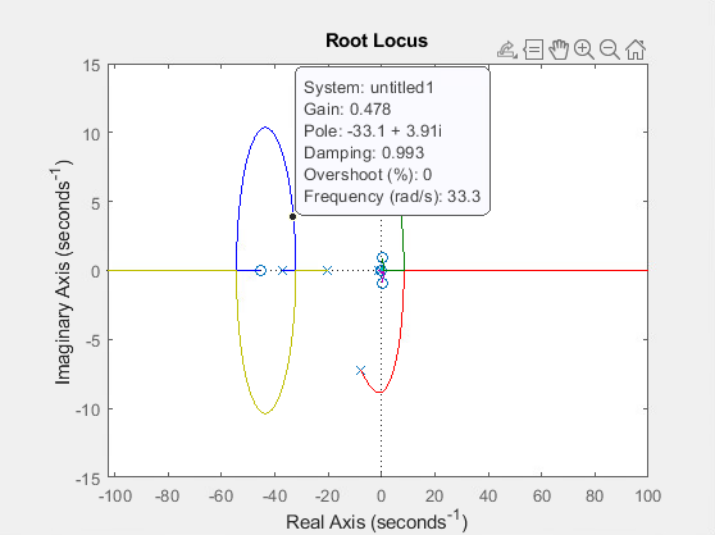

Figure 5.20 Root Locus for Yaw Rate to Rudder when Kr= 0.0

The root locus plots, figures 5.19 and 5.20, displayed the root loci when the gains are set to zero. Select relatively small gains to maximize the damping in dutch-roll mode, and achieve fast tracking of roll-rate commands. Kp = 0.0619 and Kr = 0.478 were selected.

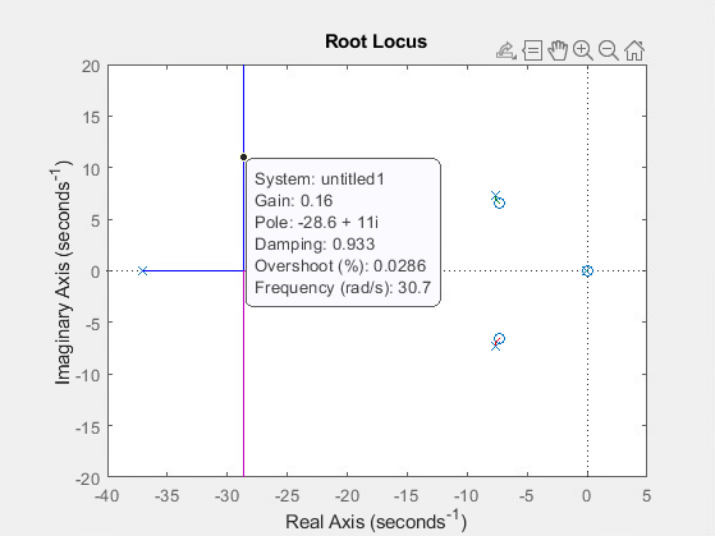

Figure 5.21 Root Locus for Roll Rate to Aileron when Kp = 0.0619

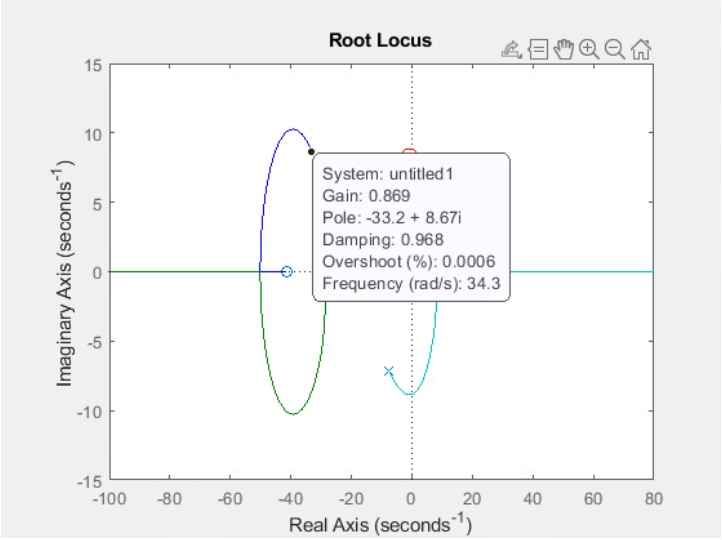

Figure 5.22 Root Locus for Yaw Rate to Rudder when Kr= 0.478

Tracking is relatively good with little to no damping, but some overshoot and steady-state error. Increase the gain to minimize overshoot and steady-state error. Kp =0.16 and Kr = 0.869 were selected. Those gains provided good tracking. The Roll rate tracking had a slight overshoot with an increasing steady-state error, and good damping due to little oscillations. The bode plots for both root loci display magnitude and phase. Additionally the block diagrams display a visual representation of the root locus plots.

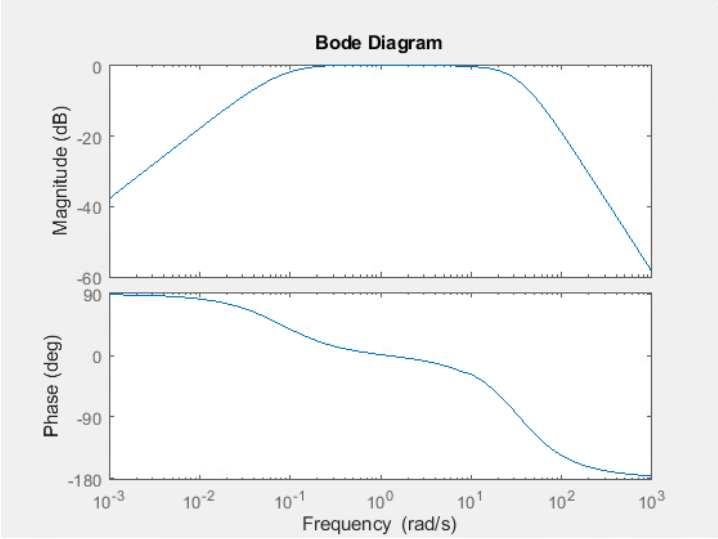

Figure 5.23 Bode Plot for Roll Rate to Aileron

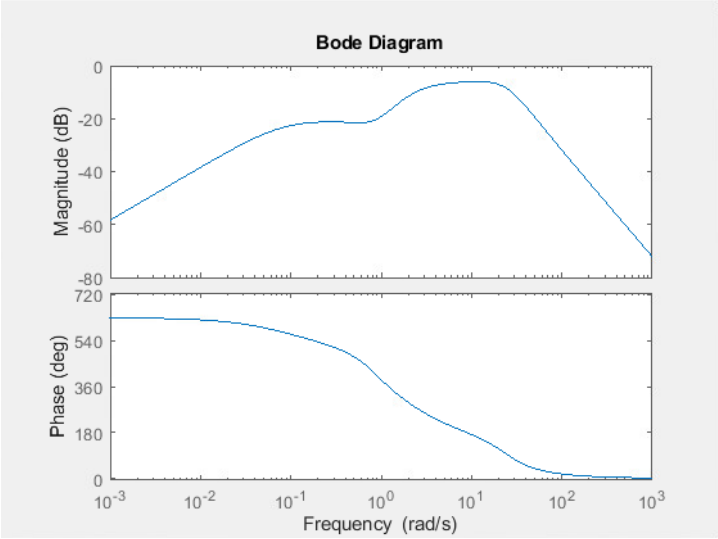

Figure 5.24 Bode Plot for Roll Rate to Aileron

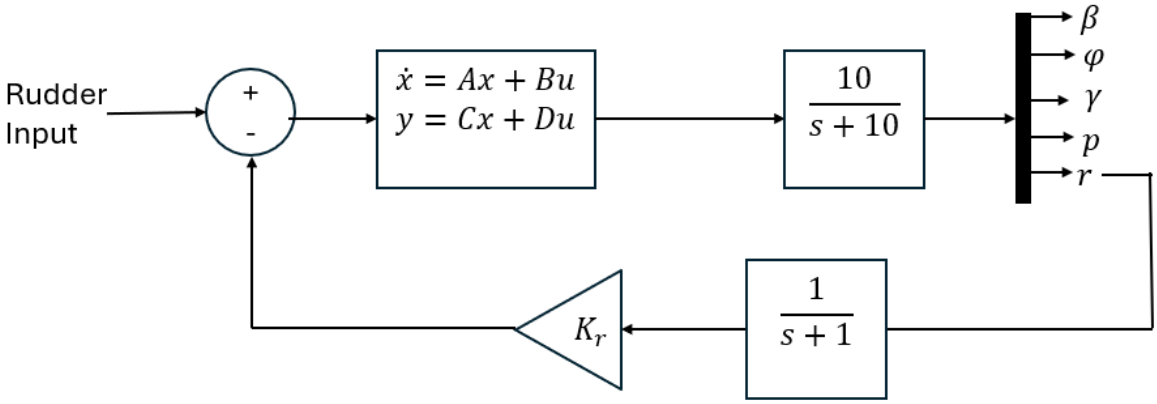

Figure 5.25 Block Diagram for Yaw Rate to Rudder

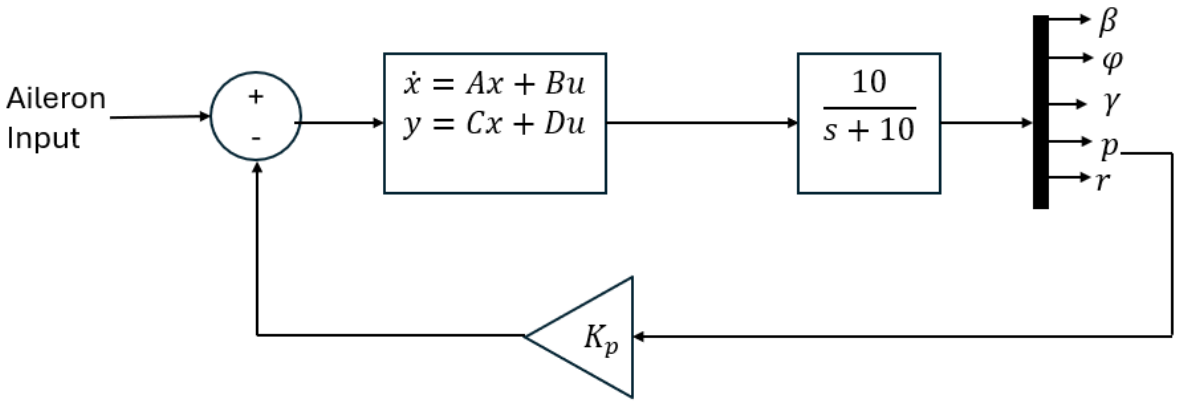

Figure 5.26 Block Diagram for Yaw Rate to Rudder

The step responses from the yaw damper portion of the controller had appropriate tracking after the gain was manipulated. To provide context the open loop plots are presented in the same plots as the closed loop responses (fig. 5.37-5.29), this provides context showing how the selected gains impacted the tracking. Additionally, the characteristics of each step response were calculated and displayed (table 5.2-5.4).

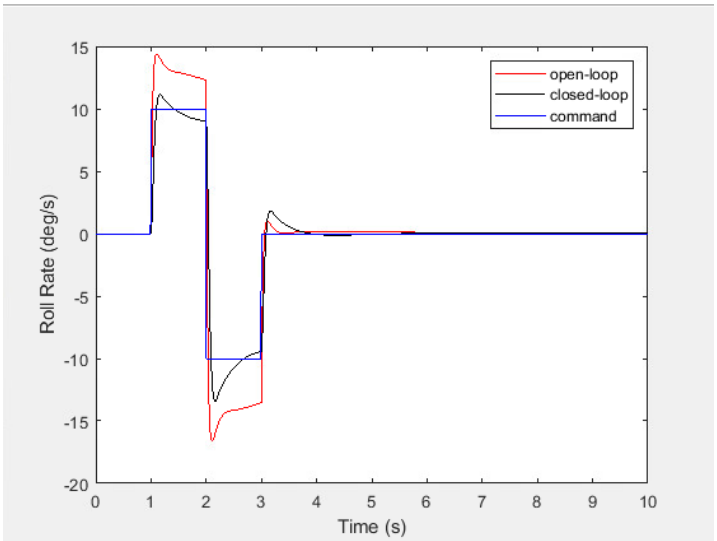

Figure 5.27 Roll Rate Response to a Doublet Command

Table 5.2 Characteristics of Roll Rate Step Response

Parameter	**Value**
Precent Overshoot	~10%
Rise Time	~0.1 seconds
Steady-State Error	~0.01 deg/s
Settling Time	~4.2 seconds

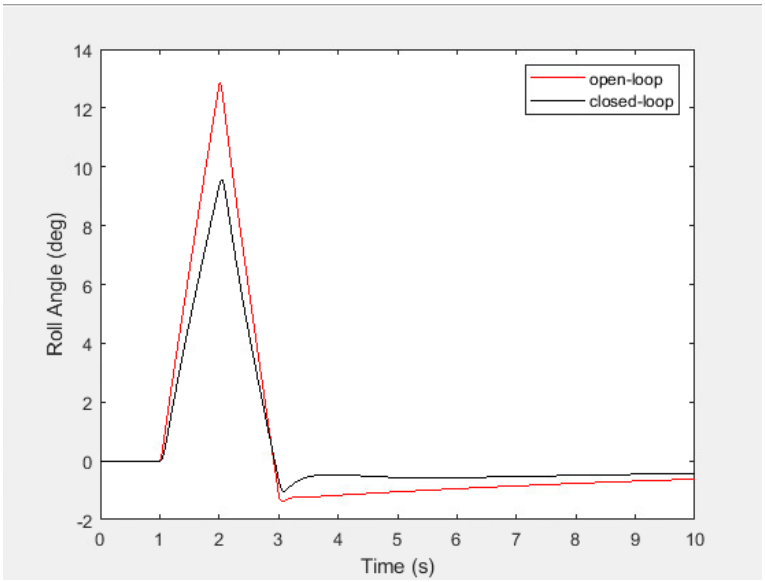

Figure 5.28 Roll Angle Response to a Doublet Command

Table 5.3 Characteristics of Roll Angle Step Response

Parameter	**Value**
Precent Overshoot	~12%
Rise Time	~2 seconds
Steady-State Error	~0.02 deg
Settling Time	~7 seconds

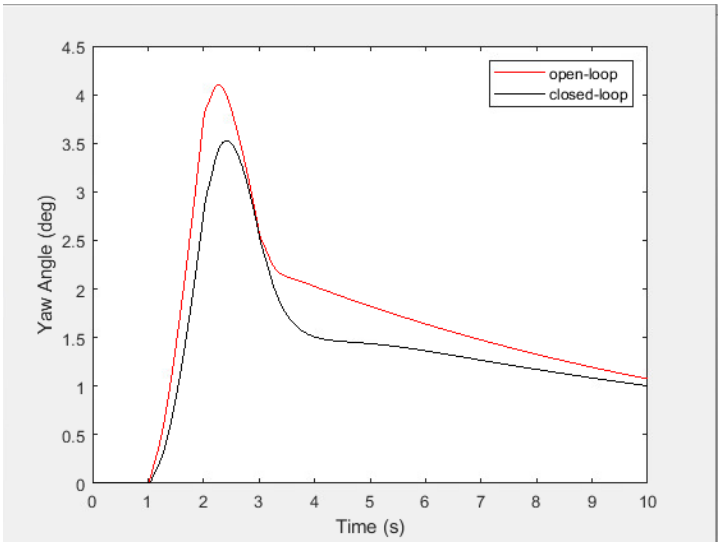

Figure 5.29 Yaw Angle Response to a Doublet Command

Table 5.4 Characteristics of Roll Angle Step Response

Parameter	**Value**
Precent Overshoot	~130%
Rise Time	~2.2 seconds
Steady-State Error	~0.1 deg
Settling Time	~9.4 seconds

The roll rate (fig. 5.27) has a good response with some overshoot, but quickly it decayed maintain a relatively constant steady-state error with good damping. Both The roll angle and yaw angle (fig. 5.28 & 5.29) have great damping, and barely any steady-state error. Both plots experienced an overshoot but quickly decayed to the desired response based on the input.

Good tracking of roll rate, roll angle, and yaw angle was essential for demonstrating the effectiveness of the control system shown in the plots above. Accurate roll rate tracking ensured that the aircraft could quickly and precisely respond to lateral commands, enabling stable and coordinated turns. Roll angle tracking was important for maintaining desired bank angles during maneuvers, directly affecting the aircraft's trajectory and passenger comfort. Similarly, yaw angle tracking played a critical role in directional stability and coordinated flight, especially during crosswind conditions or asymmetric thrust scenarios. The plots illustrated that the control system responded promptly to changes in command inputs with minimal overshoot and low steady-state error, highlighting the system's ability to maintain precise attitude control under dynamic conditions.

5.3 Actuator Response and Handling Qualities

After the controller was designed the actuator responses were explored. The actuators explored were the aileron (roll control), rudder (yaw control), and elevator (pitch control). By examining how the actuators responded to control inputs and how the aircraft behaved as a result, this analysis provides insight into the system's overall responsiveness, stability, and pilot-friendliness. Emphasis is placed on the dynamic performance of key control surfaces and their role in achieving smooth, precise maneuvering and maintaining flight stability.

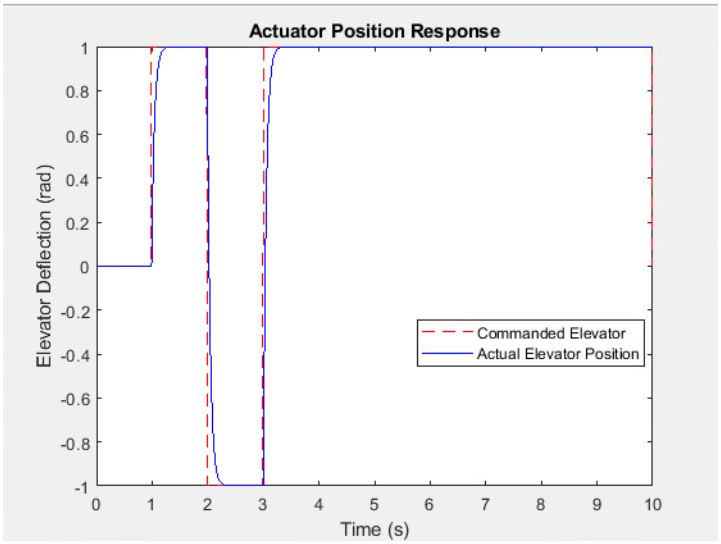

Figure 5.30 Elevator Step Response

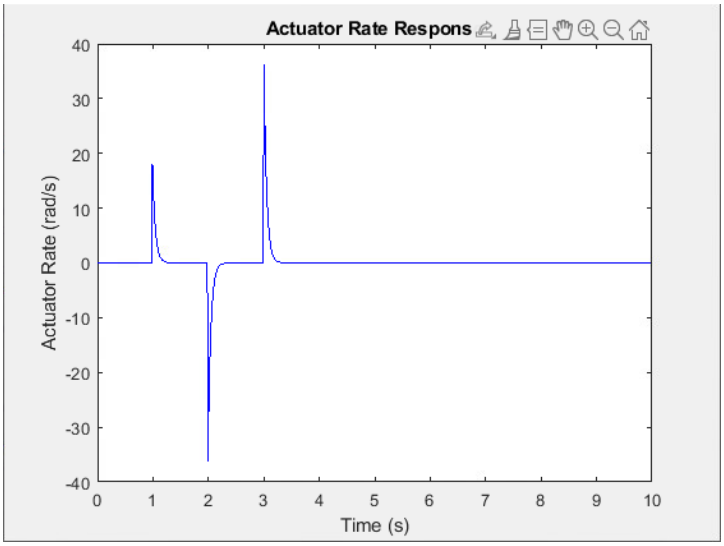

Figure 5.31 Rate of Elevator Step Response

Based on the actuator response of the elevator the altitude controller seems to have been designed in an optimal manner. To further characterize the quality of the controller the handling qualities are computed. The goal is to design a controller with level 1 handling qualities. The altitude controller is used to develop the phugoid and short-period modes. To obtain level 1 handling for the phugoid mode the damping needs to be greater than 0.04. For level 1 handling for short-period mode the damping is required to greater than 0.35 but less than 1.30. Looking at the damping obtained in the altitude root locus (fig. 5.15) or the Kh gain, the damping is equal to 0.55.

Table 5.5 Longitudinal Handling Qualities

Short-Period	**Phugoid**
$\xi = 0.55$ (level 1)	$\xi = 0.55$ (level 1)

In lateral-directional flight dynamics, the aileron and rudder serve distinct but interconnected roles in controlling the aircraft's motion. The aileron, located on the trailing edge of each wing, is the primary control surface responsible for inducing roll motion about the longitudinal axis. When deflected, it creates differential lift between the wings, producing a rolling moment that changes the roll angle (ϕ) and roll rate (p). Conversely, the rudder, located on the vertical stabilizer, governs yaw motion about the vertical axis. Its deflection generates a side force that alters the yaw rate (r) and yaw angle (ψ), and it also influences the sideslip angle (β) due to the aircraft's response to lateral aerodynamic forces.

The aileron step response and response rate were presented in section 5.2.2 as figure 5.26 and 5.27, the roll rate and roll angle. Therefor ethe aileron actuator step response and rate of response are not presented in this section. The Rudder step response and rate of response are displayed in figures 5.32 and 5.33.

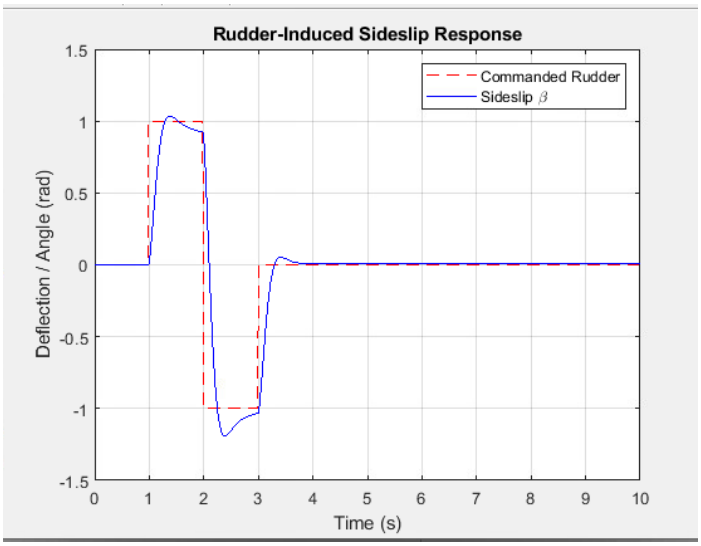

Figure 5.32 Rudder Step Response

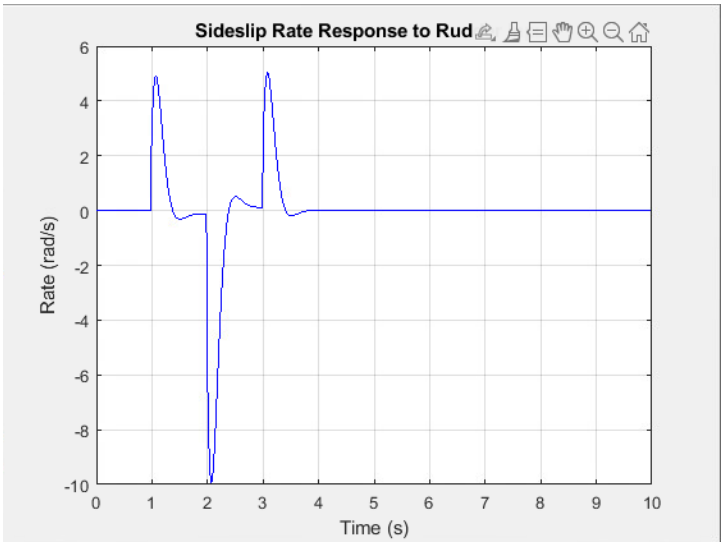

Figure 5.33 Rate of Rudder Step Response

Lateral–directional state matrix is used to generate the both the Spiral and Dutch-roll mode. The Dutch-roll is comprised of both sideslip and yaw rate, and is shown by a oscillatory nature during the rudder's step response. The Spiral mode occurs when a slow divergence or convergence in roll and yaw angle during the aileron's step response. For Spiral mode, level 1 handling qualities are obtained when the time to double is greater than 12 seconds or if the response is stable. For Dutch-roll mode, level 1 handling qualities are obtained when damping is greater than 0.08 and natural frequency is greater than 0.4. The natural frequency and damping ratio for Dutch-roll can be obtained the from the eigenvalues from the lateral–directional state matrix.

Table 5.6 Lateral–Directional Handling Qualities

Spiral	**Dutch-roll**
Stable (level 1)	$\xi = 0.72, \omega_n = \ 10.5 \frac{rad}{s}$ (level 1)

The design met the desired handling qualities for all four modes. Next the autopilot or waypoint navigation was tested to see if the aircraft could effectively reach three desired waypoints.

5.4 Waypoint Navigation

The waypoint navigation tested the autopilot and the overall controller for the aircraft. Three waypoints were selected and the controllers with designed gains explore in section 5.2 were input into the waypoint simulation MATLAB file. When ran, the output showed the simulated flightpath for the aircraft with the designed controller.

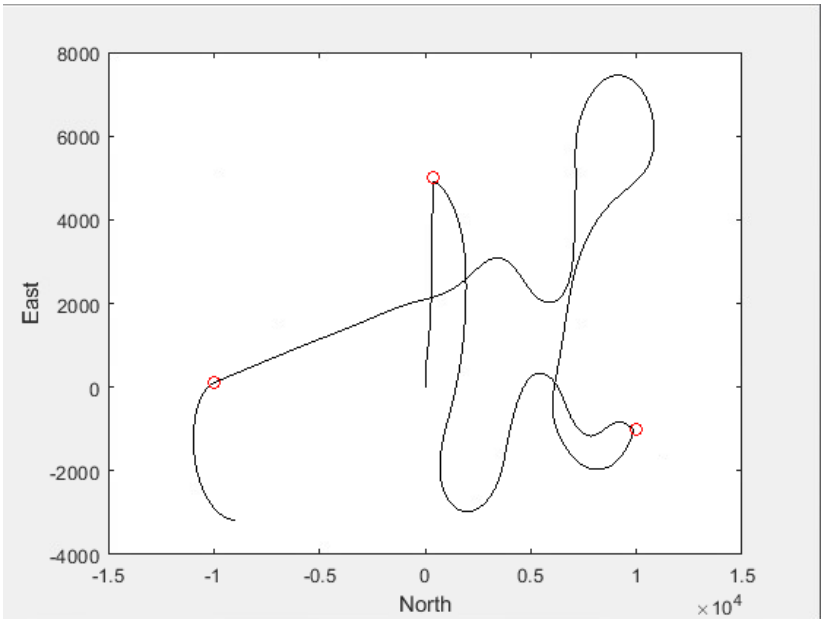

Figure 5.34 North-East View of Waypoint Flight Path

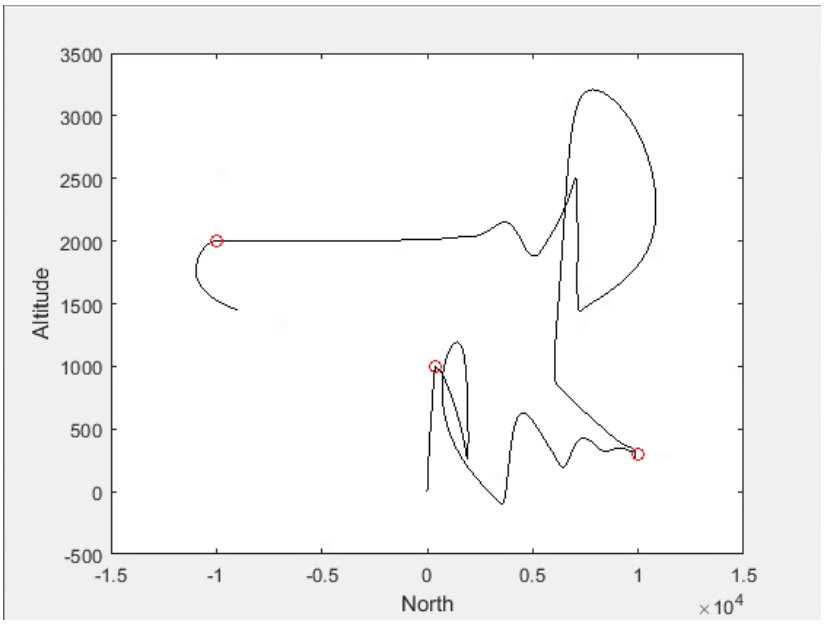

Figure 5.35 Altitude-North View of Waypoint Flight Path

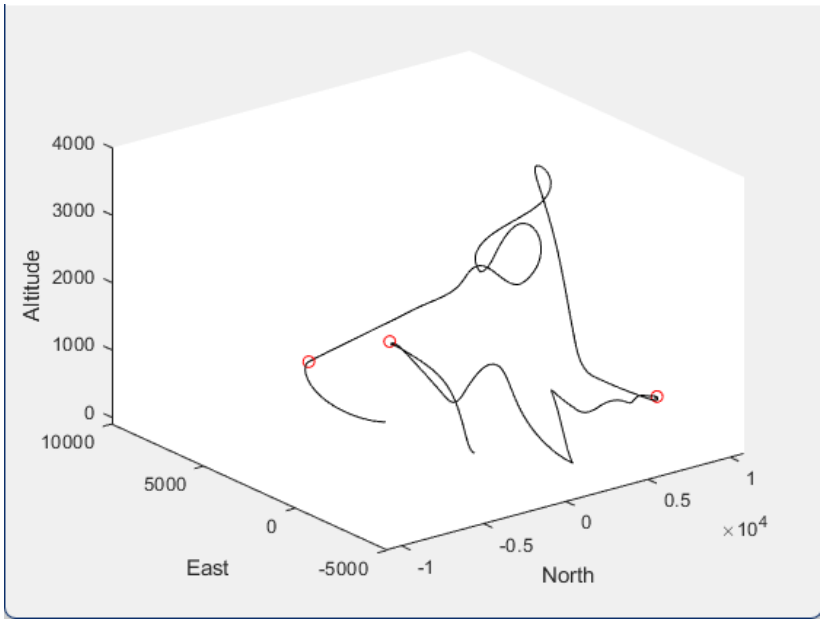

Figure 5.36 3D View of Waypoint Flight Path

Figures 5.34-5.36 show the flight path of the waypoint navigation including the 3D view and other views to provide context and different perspectives of the flight path. The aircraft was able to successfully reach all three waypoint locations. The effectiveness of the controller could be debated as the flight path is not the most efficient, meaning the controller could be optimized to be more fuel efficient. As seen most clearly in figure 5.34 the aircraft doubled back after reaching the first waypoint, and made an inefficient turn from waypoint 2 to 3. This could be credited to the large overshoot seen in the roll angle and deflection angle plots (fig. 3.39 & 3.40) or in the lack of damping in the heading and altitude plots (fig. 3.37 & 3.38). Improving the flight

path would make the aircraft more fuel efficient and more robust overall allowing it to fly for longer durations when utilizing the autopilot feature.

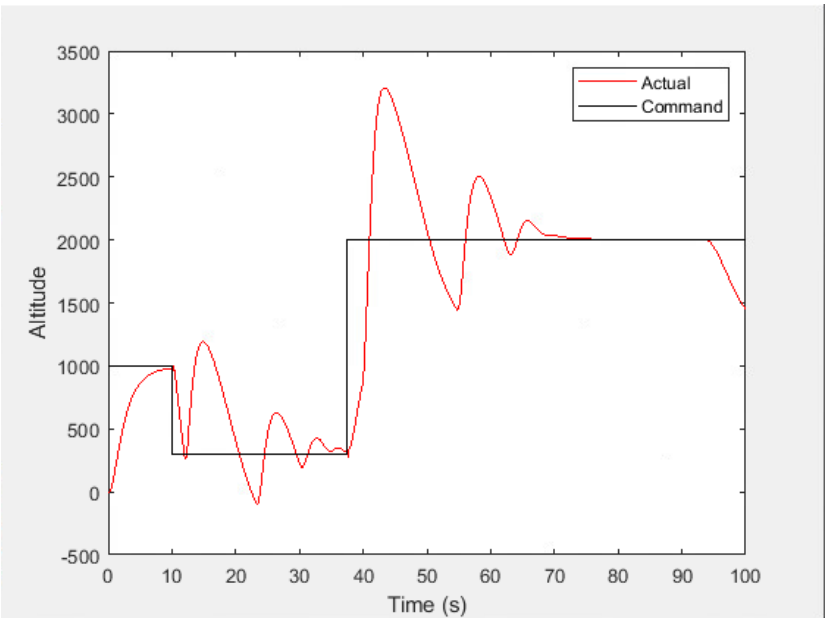

Figure 5.37 Altitude vs Time for the Waypoint Navigation

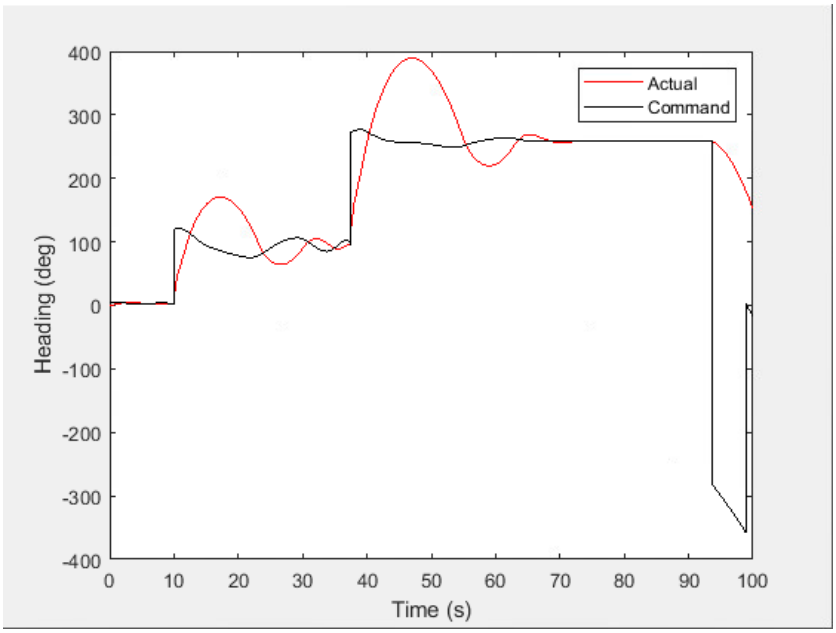

Figure 5.38 Heading vs Time for the Waypoint Navigation

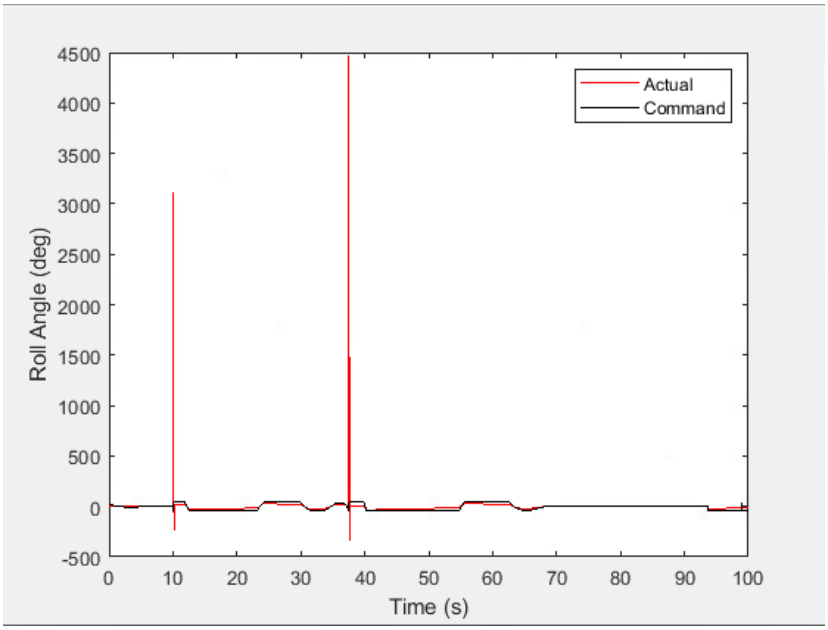

Figure 5.39 Roll Angle vs Time for the Waypoint Navigation

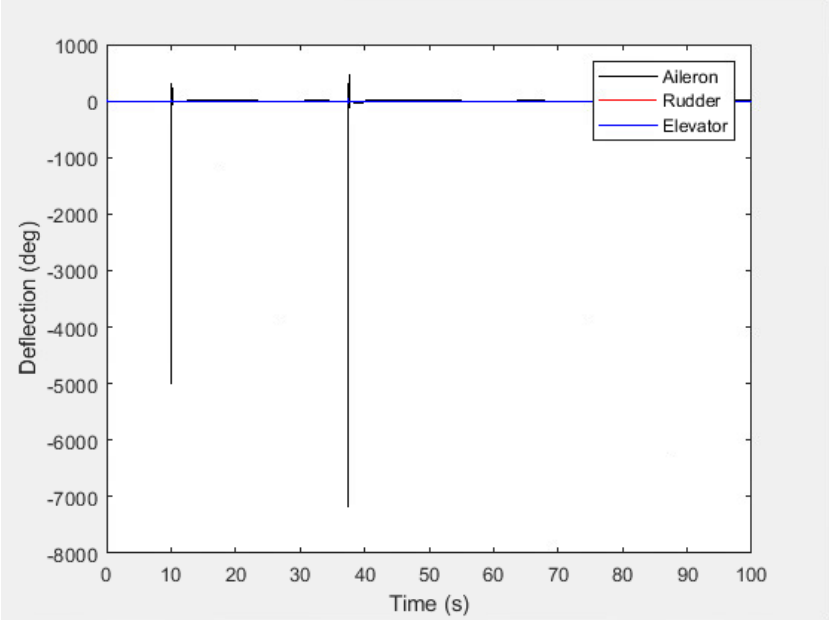

Figure 5.40 Deflection vs Time for the Waypoint Navigation

The deflection and roll angle plots have two large overshoots at about 9 seconds and about 38 seconds. These two outliers cause the plots to zoom out drastically. To get a better understanding of the tracking the plots for those two were zoomed in (fig. 5.41& 5.42). These two large overshoots or spikes can be ignored due to the fact that the rest of the plot has very food tracking.

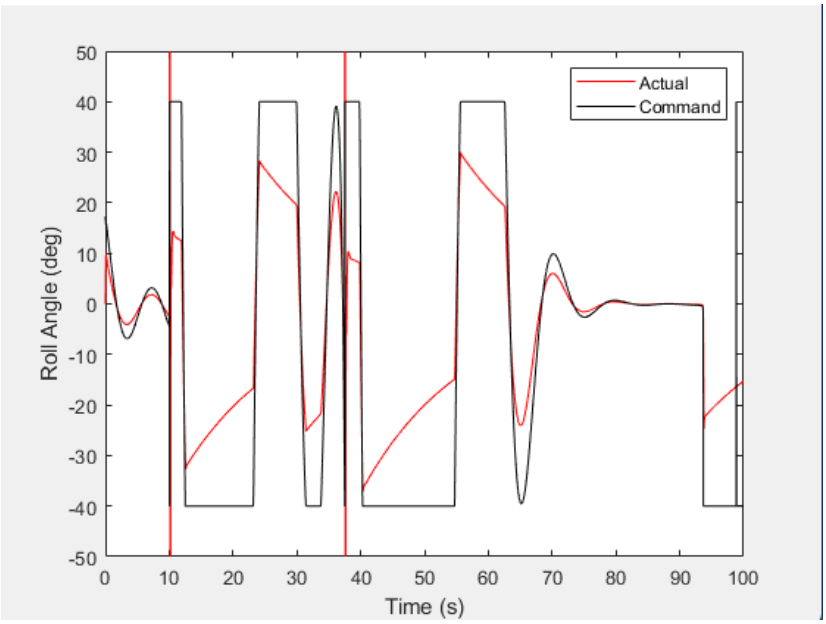

Figure 5.41 Roll Angle vs Time for the Waypoint Navigation

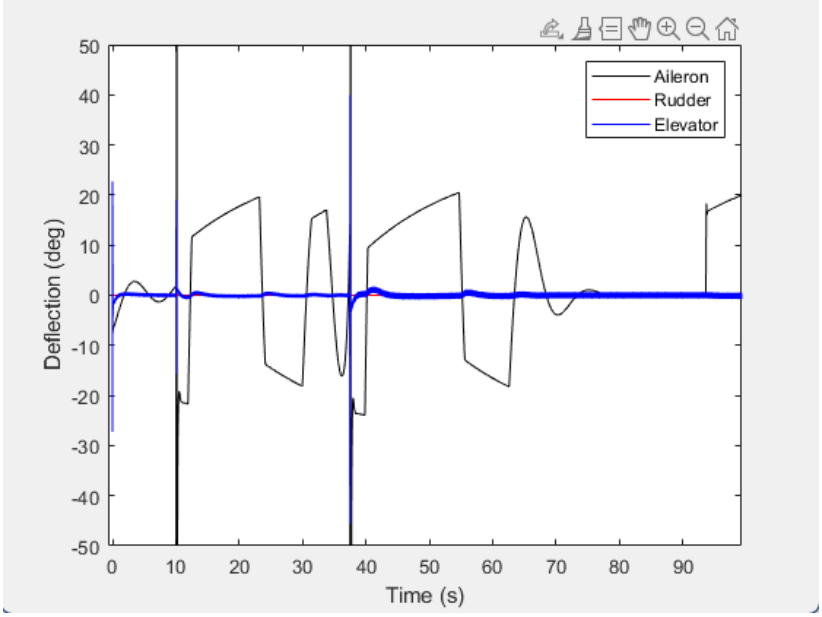

Figure 5.42 Deflection vs Time for the Waypoint Navigation

From the zoomed in version of the graphs, it can be seen that the roll angle some solid tracking with fast responses and no oscillation. Although there's appears to be an inconsistent steady-state error that varies from 0.01 degrees to 20 degrees. The deflection of the three actuators varies. The Aileron fluctuates the most while the elevator and rudder seem to stay constant for the most part. The variation in aileron was most likely caused by the aircraft climbing and descending to reach the various waypoints. This corresponds with the oscillation in altitude of the aircraft (fig. 5.38)

5.5 Optimal Design with LQR

A Linear Quadratic Regulator is an optimal full-state feedback law for a time-invariant linear system. Begin by assigning weight and cost values. The LQR then computes the unique state-feedback gain that minimizes the integral of a quadratic cost composed of those state and control penalties. Internally, this requires solving the algebraic Riccati equation to find the optimal cost-to-go matrix, from which the feedback gain is directly constructed. The result is a provably asymptotically stable closed-loop system whose transient behavior reflects the chosen trade-off between regulation performance and control authority. Basically, a more mathematical approach to designing a controller than a PID.

A LQR was designed for the altitudehold architecture. The step response for the altitude input was created and compared to the PID step response (fig. 5.43).

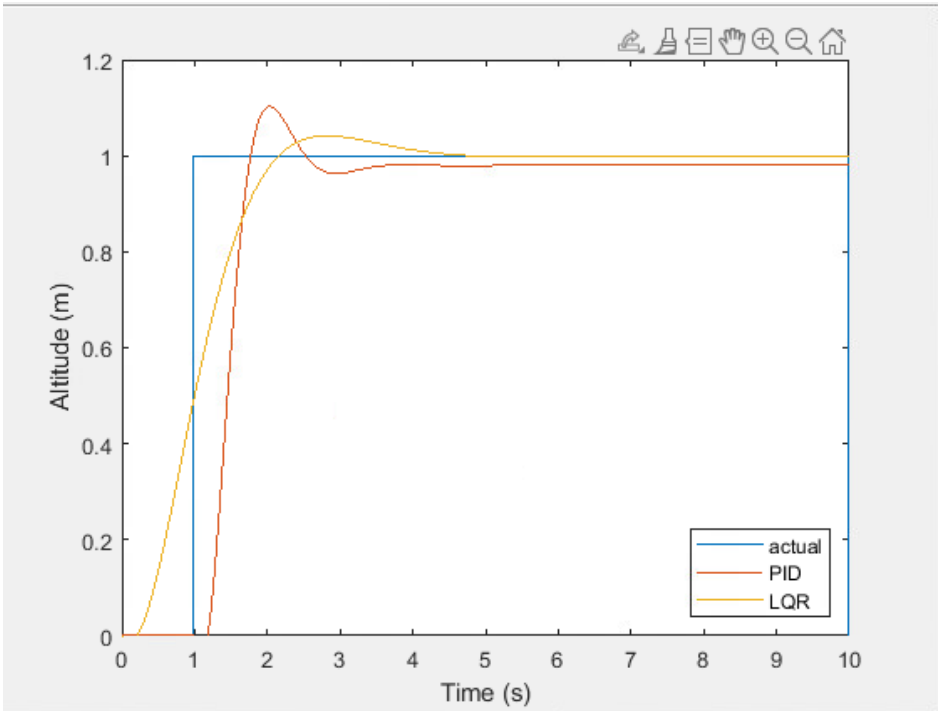

Figure 5.43 LQR vs PID for Altitude Step Response

Designing a PID controller is generally simpler and more intuitive than an LQR controller, making it a popular choice for quick implementation and basic systems. It requires minimal system modeling and relies on tuning three gains (proportional, integral, derivative), often through empirical methods. In contrast, LQR design is more mathematically involved, requiring a full state-space model and thoughtful selection of weighting matrices, but it offers a more systematic and optimal approach to control. In terms of tracking performance, PID can handle step references effectively and is robust to modeling uncertainties, but it can struggle with complex, high-order, or multivariable systems. LQR, while not inherently designed for reference tracking, can achieve superior control quality—especially when augmented with integrators—and excels in managing multi-input, multi-output systems with precise state regulation. Overall, PID is ideal for simpler applications or when time and resources are limited, while LQR offers higher-quality control in well-modeled, advanced systems

5.6 Robustness Analysis

A robustness analysis is essential in aircraft design because it ensures that the aircraft can perform safely and reliably under a wide range of real-world uncertainties, such as changing weather conditions, sensor noise, or component variability. By evaluating how sensitive the aircraft is to these factors, engineers can validate design margins, ensure control systems remain stable, and identify potential worst-case scenarios that might otherwise go unnoticed. This process also supports regulatory certification by providing evidence that the aircraft meets safety requirements across different operating conditions. Ultimately, robustness analysis helps catch potential issues early, reducing the risk of costly redesigns or failures and contributing to safer, more dependable aircraft.

For this aircraft a Montecarlo simulation was run for the waypoint navigation simulation to understand the variation between multiple simulations painting a full understanding of the aircraft's capabilities. The simulation focused on plotting the distribution of open-loop poles and compared the distribution across the various simulations. The variations across the simulations correlate with the uncertainty of the aircraft and help characterize how "good" it is.

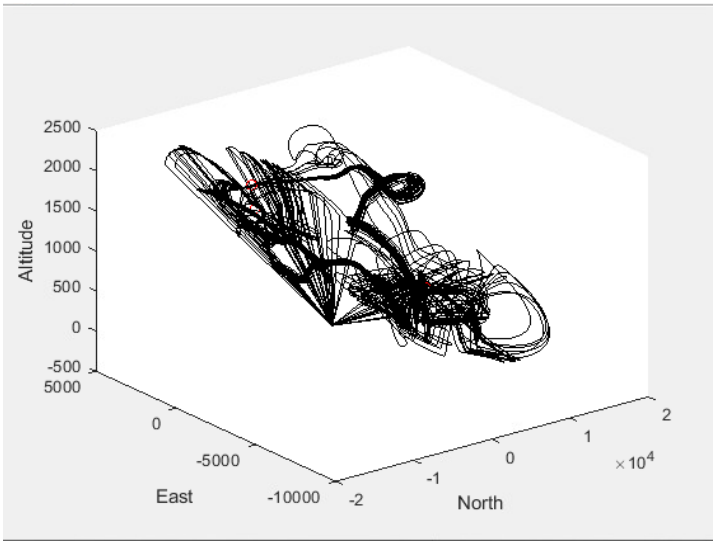

Figure 5.44 Montecarlo Simulation for Waypoint Navigation

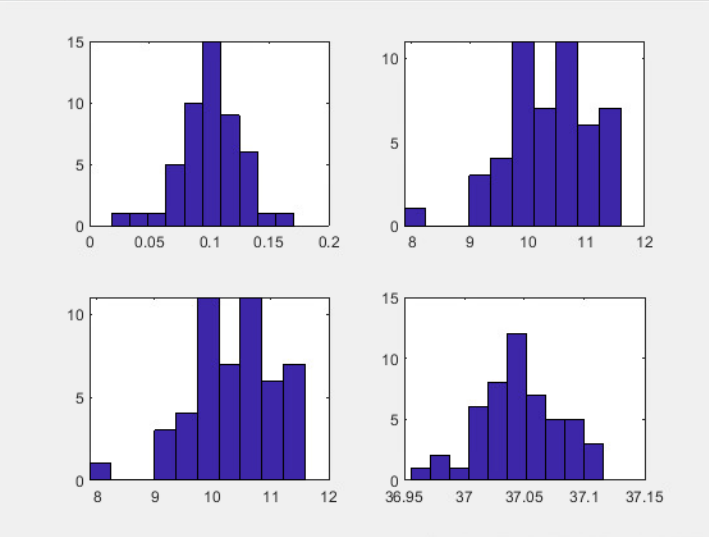

Figure 5.45 Distribution of Open-loop poles from Montecarlo Sim (1)

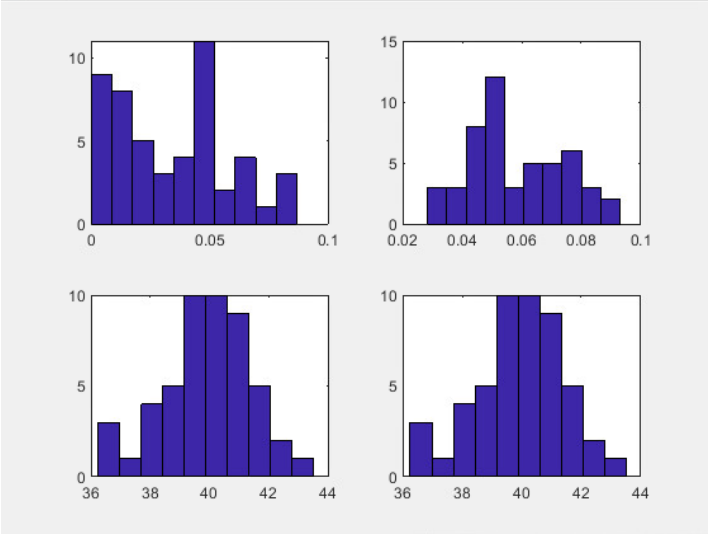

Figure 5.46 Distribution of Open-loop poles from Montecarlo Sim (2)

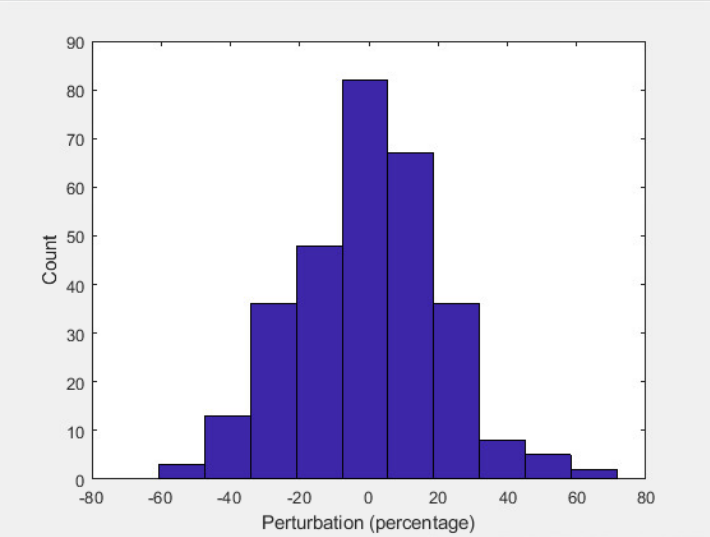

Figure 5.47 Distribution of Perturbations from Montecarlo Sim

The distribution of perturbations (fig. 5.47) shows a somewhat Gaussian distribution. The distribution showed several key variables can be considered uncertain due to the limitations of modeling and real-world variability. Aerodynamic coefficients like lift, drag, and pitching moment are often derived from wind tunnel or CFD data, which can introduce errors, especially under varying flight conditions. Mass properties, particularly the center of gravity and moments of inertia, can shift during flight and significantly impact dynamic stability, including modes like Dutch roll. Control surface effectiveness is another source of uncertainty, as actuators and surfaces may not perform exactly as modeled due to wear, damage, or nonlinearities. Environmental conditions such as wind gusts and air density also vary unpredictably, influencing the aircraft's aerodynamic performance. Structural flexibility and unmodeled aeroelastic effects can introduce unexpected dynamic behavior, while sensor and actuator limitations—like noise, lag, or saturation—add further uncertainty. Your observation about Dutch-roll damping is insightful; if there's no clear pole representing this mode, it may indicate low damping or missing yaw-related dynamics in the model, which should be accounted for in the robustness analysis [6].

6. Design Iterations

6.1. Wing Attachments

The structures and avionics specialists needed to interact with each other regarding the position and mounting of the aileron, servo, and landing gear. Because the landing gear from the stock plane was mounted in the wing, the same landing gear needed to be attached to the custom wings. In the stock plane, this mechanism involves retractable landing gear for aerodynamic purposes. An early iteration of the design accounted for this like the stock plane did, but further iterations omitted this in favor of prioritizing that internal volume to be used for structural elements. However, the avionics and structures specialists still needed to interact and iterate the

location of ribs and other wooden members to attach the landing gear, and also to leave enough space below the plane's fuselage for payload mounting.

Another interaction between these two specialists involved adjusting the wing design for ailerons. The initial design intended for full wing-length ailerons, but discussion between these specialists yielded the decision that it is better to have shorter ailerons closer to the wing tips. They collaborated to appropriately adjust the ribs to omit the trailing edge and permit a stringer there to mount the aileron to. The ribs also needed to be cut and reinforced to permit the servos to be flush within the wing and prevent aerodynamic losses here.

6.2. State Space Model from AVL

The State space model was generated from AVL for each design iteration that the Aerodynamic specialist made. Initially the stock airplane was modeled based on the original aircraft design that was built out of the box by the Avionics specialist. This geometry was inputted in AVL and the respective 12 by 12 matrices with flight stability and control properties was sent to the Controls Specialist. Each dynamic model was used to generate a newer controller for the plane. The original controller was designed for a 747 aircraft. The second was designed for the stock airplane which the design aircraft was based off. The third and final controller was designed for the design aircraft presented in the PDR, note that the dynamics used to create the controller described in section 5 was for a different aircraft then presented in the rest of the sections.

This process was repeated once the Parametrically design plane was created with interaction of Aerodynamics and Structures. The structures specialist modeled the aircraft to get an estimate for the total weight. This was then inputted into AVL to generate an updated aircraft which reflected the correct weight amount. This updated space state model was then again sent to Controls specialist for to design the PID controller for the aircraft. The gain for each root locus was iteratively designed. Each design iteration a gain was selected and the dynamics were run to view the expected step response. The gains were then adjusted based on the response to either eliminate steady-state error, over shooting, or to add damping to eliminate oscillations. The controller was designed for the rudder, aileron, and elevator actuators which resulted in level 1 handling qualities for all four modes.

6.3. Wing Geometry Compatibility with Structures

In early stages of the design process, the aerodynamics specialist reported wing geometries to the structures specialist based on AVL simulations. The structures specialist created a model of the wing in SolidWorks and tested its compatibility with the stock model, noting that the specified root chord was too large to fit the fuselage connection point. This was reported back to the aerodynamics specialist who changed their model to have an allowable root chord size with a taper to the wing tip. The new geometry was given to the structures specialist, and another CAD model was created. After several iterations of deflection testing, it was determined that the small size of the tip chord did not allow enough room for spar and stringers to meet deflection goals. This was reported back to the aerodynamics specialist along with an estimation of the required tip chord length. The aerodynamics specialist then iterated their design until a taper ratio was found that met aerodynamic design objectives while also allowing enough room for structural members to maintain rigidity.

7. Ethical Considerations

7.1. Potential for Misuse

Sweet Silence's pacifier delivery aircraft is intended for good, but the company must also consider the idea that technology designed for good can also be misused. The intent behind the company is to maintain community peace. It is oriented around proper safety for the communities they serve, and hygiene for the babies receiving the delivered pacifiers. One side of the ethical considerations of the potential for this technology to be misused is that the ethics begins and ends at operational intent. Sweet Silence has designed and manufactured this aircraft to be used to serve people and better a community. It is intended for this plane to be solely maintained and operated by the company, so therefore potential ethical liability for misuse ends in the hypothetical where someone has stolen or otherwise separated the aircraft from Sweet Silence's operation and is using it in a manner separate from the company's intent.

However, the other perspective on this issue argues that the ethical liability for any potential misuse of a technology still lies with its creator. This perspective notes that any aerial system could be exploited for surveillance, harassment, or disruption. Specific to this pacifier delivery aircraft is the potential for modifying the payload to deliver unwanted or harmful items. They argue that it would be negligent of the company to ignore the possibility of misuse. Some ways to correct this negligence may involve a reasonable level of safeguards, such as securely storing the aircraft to prevent theft, implementing limits within the flight software to prevent operation outside of the dedicated operation zone, and manufacturing techniques which increase the level of difficulty to maliciously modify the plane or payload capabilities.

7.2. Responsible Disclosure of Aircraft Performance Metrics

The ethics of information disclosure to the customer is critically important. While it may be tempting to omit or downplay modeling or flight data that indicates sensitivity, lack of robustness, or potential instability, doing so would be ethically irresponsible and could jeopardize both mission success and public safety. Regarding Sweet Silence's mission — soothing distressed infants across a dense urban environment —the humanitarian and emotionally charged nature of the mission ensuring reliable, stable performance is not just a technical goal but a moral obligation.

In practice, this means that all relevant data should be presented transparently to the customer, even if some aspects reveal weaknesses in the current design. For example, if the aircraft's roll response shows high sensitivity to turbulence or there is evidence that certain yaw modes may become unstable under specific wind conditions, this must be explained clearly. Ignoring or hiding such findings would not only mislead the customer but could also result in operational failures, delays, or loss of trust — all of which are particularly unacceptable in a mission aimed at supporting vulnerable populations.

Ethical engineering demands full disclosure, paired with well-thought-out mitigation strategies. This might include highlighting areas of concern, offering design revisions, or clarifying the operating conditions under which performance issues may arise. Ultimately, presenting the complete truth — even when imperfect — fosters a collaborative, responsible approach to solving problems and ensures that the mission of delivering pacifiers is carried out safely, effectively, and with integrity.

7.3. Topic 3

Each teammate is responsible for keeping up with their own work in order for the team to function well. Compensation for members can lead to negative cascade effects which may result in inaccurate aircraft performance. When working as part of a team, ethical considerations are essential, especially when it comes to balancing support for teammates within the long-term success of the group. In the short term, doing extra work to cover for a teammate who is falling behind may seem like a helpful solution. It could prevent immediate disruptions and help meet deadlines. However, this could ultimately enable the individual who is falling behind to avoid responsibility for their actions, potentially create an unintended a sense of dependence. Over time, this could harm both the individual and the team, as the teammate may not develop the necessary drive to improve their own performance, as someone will just help them out.

Addressing the issue to the teammate who is underperforming can be an ethically difficult decision. While it may feel like a betrayal, it could ultimately benefit both the team and the individual in the long run. By addressing the issue directly, the teammate has an opportunity for discussion to possibly help resolve the issue for the future. This ensures that the work is fairly distributed and that everyone is held accountable for their contributions. Ultimately, addressing and preventing someone from getting behind should be done with consideration of the potential outcomes but with a focus on helping the team improve, rather than merely shifting blame.

7.4. Environmental and Societal Implications

This aircraft runs on a 5200 mAh battery which requires frequent recharging. There is an environmental cost associated with producing the electricity needed to run a high volume of aircraft frequently. Currently, the majority of electricity is produced with fossil fuels which create carbon emissions. The design detailed in this report was customized to closely fit Sweet Silence's mission requirements and provide the most efficient flight possible. Additionally, a conscious decision was made by the design team in creating a fully electric vehicle because it is our belief that in time, more renewable energy will be utilized in creating the electricity required to power our aircraft. Sweet Silence also packages all its products in fully bio-degradable materials so that no pollution is created after customers receive their order. However, the product itself is not biodegradable and the possibility of customers not retrieving the product or not properly disposing of it after they are finished is an area for potential environmental concern.

Sweet Silence is also conscious of noise pollution, in fact, it is the idea that the company was founded on. One side of the ethical considerations behind noise pollution is that the aircraft produce noise in populated areas which may disrupt non-customers. However, Sweet Silence aircraft are also delivering a solution to other forms of noise pollution which affect a more concentrated area. The noise pollution that sweet silence aircraft produce, while short lived, could be disruptive to a large audience of non-customers as the plane flies over highly populated areas enroute to the drop site.

8. Codes and Standards

The aircraft is designed to satisfy several codes and standards that are associated with flight. In particular, the Federal Aviation Administration (FAA) has established several criteria that must be met before a design can be certified and legally fly. A subset of these criteria that are used in this design are presented in Federal Airworthiness Regulation (FAR) Part 23: Airworthiness Standards for Normal, Utility, Acrobatic and Commuter Category Airplanes.

FAR : Part 23 : Section 23.177

(a.1) The static directional stability, as shown by the tendency to recover from a wings level sideslip with the rudder free, must be positive for any landing gear and flap position appropriate to the takeoff, climb, cruise, approach, and landing configurations.

The design was considered to have directional stability if $C_{n\beta}$ was greater than zero. This was demonstrated for this aircraft by the data in Figure 2.23.

(b.1) The static lateral stability, as shown by the tendency to raise the low wing in a sideslip with the aileron controls free, may not be negative for any landing gear and flap position appropriate to the takeoff, climb, cruise, approach, and landing configurations.

The design was considered to have directional stability if $C_{l\beta}$ was less than zero. This was demonstrated for this aircraft by the data in Figure 2.23.

FAR : Part 23 : Section 23.231

(a) A landplane may have no uncontrollable tendency to nose over in any reasonably expected operating condition, including rebound during landing or takeoff. The pitch is dynamically stable as seen in section 5.2.1 where the altitude hold controller was designed. The gains were selected to that both the pitch rate and pitch angle of the elevator have good tracking with strong damping and little to no steady-state error.

FAR : Part 23 : Section 23.305

a) The structure must be able to support limit loads without detrimental, permanent deformation. At any load up to limit loads, the deformation may not interfere with safe operation.

The structure is able to withstand the trim load without detrimental or permanent deformation based on SolidWorks finite element analysis covered in Section 3.3.2. The deflection of the wing tip under three times loading condition is 26.3 mm (Fig. 3.20).

References

[1] Airfoil Tools. “NACA 0012 AIRFOILS (N0012-Il).” *Airfoiltools.com*, 2019, airfoiltools.com/airfoil/details?airfoil=n0012-il.

[2] K. Alambra and N. Swanson, “Beam deflection calculator,” Omni Calculator, https://www.omnicalculator.com/construction/beam-deflection (accessed Feb. 28, 2025).

[3] Elliptical lift distribution, https://web.mit.edu/16.unified/www/SPRING/fluids/Spring2008/LectureNotes/f07.pdf (accessed Feb. 28, 2025).

[4] NACA 0012 airfoil section, https://ntrs.nasa.gov/api/citations/19880019495/downloads/19880019495.pdf (accessed Feb. 28, 2025).

[5] R. Lind, “Lecture Notes slide0225-slide0306”, (accessed April 10, 2025)

[6] Stevens, B.L., Lewis, F.L., & Johnson, E.N. “*Aircraft Control and Simulation*,” 3rd Edition, Wiley, 2015. Chapter 7 (Modeling Uncertainties) and Chapter 10 (Stability and Control Derivatives)